

On Improving Graph Neural Networks for QSAR by Pre-training on Extended-Connectivity Fingerprints

Sam Money-Kyrle¹, Markus Dablander², Thierry Hanser³,
Stephane Werner³, Charlotte M. Deane¹, Garrett M. Morris^{1*}

¹Department of Statistics, University of Oxford, 24-29 St Giles',
Oxford, OX1 3LB, United Kingdom.

²Mathematical Institute, University of Oxford, Andrew Wiles Building,
Woodstock Road, Oxford, OX2 6GG, United Kingdom.

³Molecular Informatics and AI, Lhasa Limited, Granary Wharf House,
2 Canal Wharf, Leeds, LS11 5PS, United Kingdom.

*Corresponding author(s). E-mail(s): morris@stats.ox.ac.uk;

Abstract

Molecular Graph Neural Networks (GNNs) are increasingly common in drug discovery, particularly for Quantitative Structure-Activity Relationship (QSAR) studies; yet, their superiority compared to classical molecular featurisation approaches is disputed. We report a general strategy for improving GNNs for QSAR by pre-training to predict Extended-Connectivity Fingerprints (ECFP). We validate our approach with statistical tests and challenging out-of-distribution (OOD) splits. Across five out of six Biogen benchmarks, we observed a statistically significant improvement in standard performance metrics over all evaluated baselines when using ECFP pre-trained GNNs. However, for more heterogeneous datasets and more complex endpoints, such as binding affinity prediction, pre-trained GNNs underperformed in OOD settings. Importantly, we investigated the impact of substructure-level data leakage during pre-training on downstream performance. While we identified scenarios where pre-training on ECFPs was less effective, our findings show that ECFP-based pre-training can enhance downstream OOD performance on a diverse set of practically relevant QSAR tasks.

Keywords: Extended-connectivity fingerprints, Molecular property prediction, Graph neural networks, Pre-training, QSAR, Out-of-distribution generalisation, molecular substructures

1 Introduction

Machine learning (ML) has become a prominent method for accelerating therapeutic drug discovery research [1]. An example of this is Quantitative Structure-Activity Relationship (QSAR) studies, where computational models are used to predict molecular properties. QSAR studies are useful for profiling and filtering candidate drugs before clinical trials. In drug discovery, after binding affinity, molecular properties primarily relate to absorption, distribution, metabolism, excretion, and toxicity (ADMET). Numerous methods have pushed state-of-the-art performance forward on ADMET benchmarks, e.g., [2–9]. However, attrition rates in small molecule drug discovery have increased in recent years [10], suggesting benchmark performance does not reflect impact. This is partly due to a key limitation in drug discovery; experimental datasets for training and benchmarking are typically small, noisy, and heterogeneous, leading to biased models and inaccurate performance estimates [11–13].

To overcome the limitations in QSAR, we need robust molecular representations that reduce bias and capture relevant task-specific information. Classical representations include topological fingerprints, e.g., Extended-Connectivity Fingerprints (ECFP) [14], where substructure or pharmacophore presence is encoded by bits in a binary vector [15]. Differentiable representations based on deep learning are a more recent approach which utilise forward- and back-propagation to extract meaningful features from the input data in a latent embedding space. The ability to automatically derive abstract, non-linear patterns from non-tabular data should make differentiable approaches particularly useful in complex domains like chemistry.

One such differentiable approach is graph-based representation learning, which is an intuitive choice for molecular featurisation; molecules can be easily represented as graphs, with atoms as nodes and bonds as edges. Graph neural networks (GNNs), which operate on molecular graphs and learn task-specific molecular embeddings, have been applied to QSAR, showing promising performance as a featurisation method [3, 4, 7, 9], but other results suggest GNN-based methods struggle to outperform classical approaches [16–18]. Self-supervised pre-training has been proposed as a solution for improving GNN performance and overcoming dataset constraints [2, 19–21]. Implemented strategies include pre-training on context prediction and attribute masking [6], self-supervised pre-training via contrastive learning [8], a disentangled transformer approach pre-trained on topological substructure environments [2], and pre-training on physicochemical descriptor vectors (PDV) [21].

Although pre-training GNNs for QSAR, both supervised and self-supervised, has been investigated and shown promise, there are limitations with how some methods have been assessed. Firstly, there is a lack of statistical testing against baselines, such as models trained from scratch on benchmark data represented via commonly used static fingerprints [22, 23]. Secondly, benchmark comparisons between learned representations pre-trained on different datasets do not provide a picture of architectural superiority. Thirdly, the interpretability of pre-trained models is rarely explored beyond nearest-neighbour analyses of learned embeddings. Finally, data leakage between pre-training and benchmark datasets is often overlooked, particularly at the substructural level. Méndez-Lucio et al. excluded molecules with identical Tanimoto similarities to benchmark molecules from pre-training data [2]. More recently,

van Tilborg et al. used a 0.7 Tanimoto similarity threshold of between Bemis–Murcko scaffolds to filter pre-training data [24]. We propose a more stringent similarity threshold of 0.5 to filter pre-training data, and investigate the impact of substructure-level data leakage on downstream performance.

Data leakage is especially concerning in supervised pre-training, where benchmark and pre-training datasets can overlap at both task and molecule levels due to limited open-source experimental data. Generalisation in the form of robust out-of-distribution (OOD) performance is essential for identifying novel areas of chemical space with therapeutic potential and validating in-distribution performance [25, 26]. Therefore, consideration of potential data leakage between pre-training and benchmark datasets is essential in QSAR model development. We investigate the impact of data leakage on downstream performance by applying similarity filtering to pre-training data.

In addition to data leakage, the choice of benchmark splits is essential for evaluating OOD performance, as in-distribution splitting can exacerbate benchmark bias [26, 27]. Since exploring novel chemical space is important for developing new drugs, ML models should be evaluated for robust OOD performance using benchmark splits with minimal molecular overlap. Commonly used OOD splitting by molecular scaffolds is vulnerable to information leakage and performance overestimation [26, 27]. Hierarchical clustering on UMAP projections of molecular fingerprints produces challenging OOD splits; however, train-test split sizes tend to vary [28], which could increase the variance in performance estimates. On the other hand, Butina clustering on topological fingerprints is a fast, distance-based method that forms evenly sized clusters [29]. Here we opt for the latter approach to generate many evenly-sized OOD splits.

Despite using a consistent splitting strategy, test set performance is variable between splits; this volatility can obscure whether differences between ML approaches are meaningful. To validate whether these differences are statistically significant, repeated cross-validation (CV) combined with statistical testing and effect size estimation is recommended [22]. However, robust effect size estimation can be challenging in cases where differences are expected to be subtle, or for tasks where performance is highly variable (e.g., highly imbalanced classification tasks). Moreover, as folds within each k-fold split are mutually exclusive, fold-level metrics within a CV repeat are not independent and should be averaged before statistical testing. We therefore use a high number of repetitions (200×5 CV) to generate many OOD train-test splits for robust statistical comparison.

Here, we explore self-supervised pre-training on topological fingerprints as a general method for improving GNN predictive performance in QSAR. We also include an exploratory analysis of substructure importance in Supplementary Information Section 1.3, facilitated by our multi-radius substructure tokenisation approach. Finally, we investigate the impact of substructure data leakage between pre-training and benchmark datasets, finding that the impact with our pre-training strategy is limited.

2 Results

Graph Isomorphism Networks (GINs) [30] pre-trained to predict topological fingerprints (PT-GIN), showed statistically significant improvements over baseline methods

on challenging OOD splits in five out of six Biogen regression tasks. We also observed relative underperformance on MoleculeNet tasks, particularly virtual screening, and ChEMBL binding affinity prediction tasks, suggesting that our pre-training strategy may not fully overcome the challenges posed by data heterogeneity and complex end-points. Additionally, we found that data leakage between pre-training and benchmark datasets has a minimal impact on downstream performance when using our proposed pre-training strategy.

Benchmarking was carried out on 40 tasks (11 regression and 29 classification) from Biogen [31], MoleculeNet [32], and ChEMBL [16, 33]. For our baseline featurisation methods, we compared the predictive performance of PT-GIN against three classical molecular fingerprinting techniques; hashed Extended-Connectivity Fingerprints (ECFP_{hashed}), hashed Functional-Connectivity Fingerprints (FCFP_{hashed}) [14], and ECFPs vectorised via S&S (ECFP_{S&S}) [34]. On Biogen, we additionally benchmarked Scratch GINs to demonstrate pre-training impact. All featurisation methods were evaluated with Light Gradient-Boosted Machines (LightGBM) [35], except Scratch GIN (end-to-end MLP head). Performance metrics are reported as 5-fold test-set means for each CV repeat; statistical significance tests and effect sizes were computed across repeats. See methods for further details.

2.1 GINs pre-trained on ECFPs outperform baselines on homogeneous QSAR datasets

Biogen is a homogeneous dataset of drug-like molecules with six diverse QSAR regression tasks. A model with greater correlation and lower error on OOD splits for these tasks is more likely to generalise well to novel chemical space. On five of six Biogen tasks, PT-GIN achieves the highest mean coefficient of determination (R^2), with statistically significant improvements over baseline approaches (Fig. 1). On these five tasks, PT-GIN has the highest mean Pearson Correlation (ρ) (Fig. 1). Moreover, the r_{rb} effect sizes for R^2 between PT-GIN and the baseline methods are consistently 1.00, indicating that PT-GIN outperforms all baselines on every CV repeat (Fig. 2). The only exception is on the Human Plasma Protein Binding (PPB) task, where ECFP_{S&S} performs best by R^2 and ρ . However, on Human PPB there is no significant difference in R^2 between PT-GIN and ECFP_{hashed}, and PT-GIN still has significantly greater R^2 than FCFP_{hashed} and Scratch GIN, with a r_{rb} of 1.00 between PT-GIN and Scratch GIN (Fig. 2).

Overall, r_{rb} values for R^2 are smaller between PT-GIN and baseline methods on Human PPB than for other Biogen tasks, suggesting that pre-training has a diminished effect on performance for this task in particular. Although PT-GIN does not exhibit the greatest correlation compared to baselines on Human PPB, it has the lowest mean absolute percentage error (MAPE), with significant differences between PT-GIN and baselines. These observations suggest that self-supervised pre-training on topological fingerprints provides a robust predictive advantage over the baseline methods.

Scratch GIN models achieve the lowest mean MAPE on both intrinsic hepatic clearance (CL_{int}) tasks and the Efflux Ratio task, with a significant difference from all other approaches (Fig. 1), despite significantly lower R^2 than PT-GIN on these three tasks. In addition, PT-GIN has the highest ρ on the same three tasks, with a significant

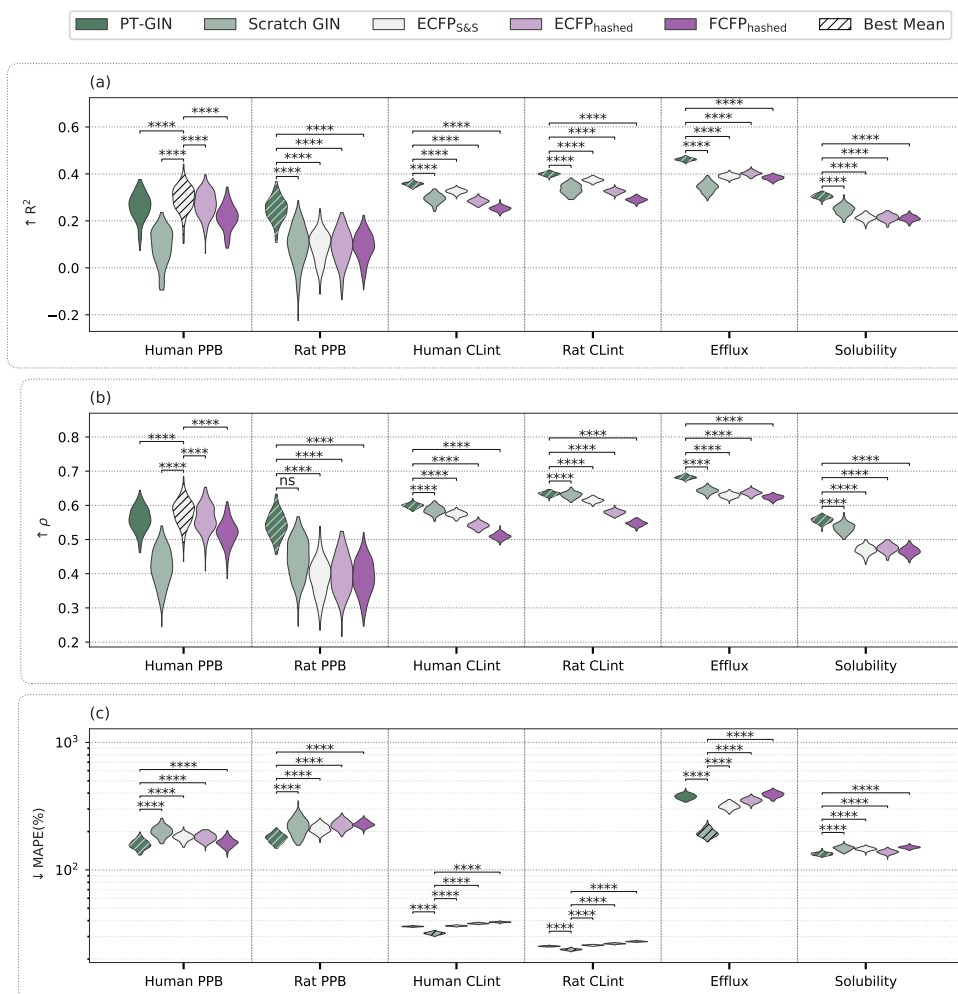


Fig. 1 Performance metrics on Biogen ADMET regression tasks. Tasks shown are Human Plasma Protein Binding (PPB), Rat PPB, Human Intrinsic Clearance (CLint), Rat CLint, Efflux, and Solubility. The metrics shown are (a) coefficient of determination ($\uparrow R^2$), (b) Pearson correlation ($\uparrow \rho$) and (c) mean absolute percentage error ($\downarrow \text{MAPE}(\%)$). Featurisation methods shown are GINs trained from scratch (Scratch GIN), ECFP-pre-trained GINs (PT-GIN), hashed Extended-Connectivity Fingerprints (ECFP_{hashed}), hashed Functional-Connectivity Fingerprints (FCFP_{hashed}), and ECFPs folded via Sort & Slice (ECFP_{S&S}). For each task and metric, the approach with the best mean is hatched. Statistical significances, determined by the Wilcoxon signed-rank test ($n = 199$, $\alpha = 0.05$), between the best method by mean and all other approaches are shown with asterisks; ns (not significant) is $p \geq 0.05$; * is $0.01 \leq p < 0.05$; ** is $0.001 \leq p < 0.01$; *** is $0.0001 \leq p < 0.001$; and **** is $p < 0.0001$. Violins are normalised such that each violin has the same maximum width.

difference from Scratch GIN on Human CLint and Efflux. This combination of lower error, lower explained variance and lower correlation for Scratch GIN compared to PT-GIN, may indicate a reduced capability of Scratch models to predict outliers on certain tasks. For in-distribution prediction, overfitting to the mean of the ground truth could be useful for interpolation in well-characterised areas of chemical space; however, for extrapolative OOD performance, prediction of outliers would be of greater interest. In summary, our results on the Biogen data set indicate that GINs pre-trained on topological fingerprint targets enable stronger OOD prediction performance on a variety of ADMET tasks.

On the three MoleculeNet regression tasks, the performance gains from pre-training on hashed ECFPs are not as clear. PT-GIN only attains the highest mean R^2 on ESOL, underperforming compared to $\text{ECFP}_{\text{S\&S}}$ on FreeSolv and Lipophilicity (Extended Data Fig. 1). Additionally, PT-GIN has a significantly lower R^2 on FreeSolv compared to $\text{FCFP}_{\text{hashed}}$ (Extended Data Fig. 2). PT-GIN attains a significantly greater R^2 than $\text{ECFP}_{\text{hashed}}$ on all three tasks, suggesting pre-training on hashed ECFPs beneficial over the classical equivalent; however, the effect size of 0.301 on FreeSolv suggests that performance gains are not ubiquitous (Extended Data Fig. 2). The R^2 and ρ scores of all methods declines on ESOL when only considering test set molecules with a drug-like solubility, $1\mu\text{M} < S < 1000\mu\text{M}$; however, PT-GIN retains a superior correlation (Supplementary Information Fig. 1).

Fingerprints folded via hashing are prone to bit collisions [34], although FCFPs less so than ECFPs due to coarse-grained grouping of atomic environments in FCFPs. $\text{ECFP}_{\text{S\&S}}$ reduces the occurrence of bit collisions by mapping frequent substructures to specific bits. Bit collisions in $\text{ECFP}_{\text{hashed}}$ may have impacted performance on FreeSolv, with methods that use classical hashed ECFPs (PT-GIN and $\text{ECFP}_{\text{hashed}}$) exhibiting lower R^2 . PT-GIN is superior to $\text{ECFP}_{\text{hashed}}$ and $\text{FCFP}_{\text{hashed}}$ for Lipophilicity, but $\text{ECFP}_{\text{S\&S}}$ outperforms all other approaches. The superiority of $\text{ECFP}_{\text{S\&S}}$ may be due to the absence of bit collisions; however, this requires further investigation.

Although alternative pre-training targets (such as $\text{ECFP}_{\text{S\&S}}$) may be more appropriate for certain tasks, the related nature of lipophilicity, free energy of aqueous solvation, and aqueous solubility (all three are related to interactions with water) suggests that task-level differences may be driven by another underlying cause. For example, substructure importance analysis on FreeSolv (Supplementary Information Section 1.3) suggests $\text{ECFP}_{\text{S\&S}}$ may be prone to reliance on, and potentially overfitting to, a specific substructure. Furthermore, experimental data in Lipophilicity and FreeSolv are aggregated from multiple sources, whereas the experimental data in ESOL originates from a single source. Discrepancies between tasks could therefore be due to greater data heterogeneity introduced by aggregating experimental data; learned representations may struggle to overcome noise from experimental inconsistency more than simpler representations.

For target-specific binding affinity, PT-GIN underperformed compared to baselines (Extended Data Fig. 3). PT-GIN has a significantly lower R^2 score than all classical approaches for DRD2 and Factor X_A , suggesting pre-training on 2D circular fingerprints harms the molecular representation for OOD binding affinity prediction. Due to the complexity of the task, it is possible that a greater volume of pre-training data

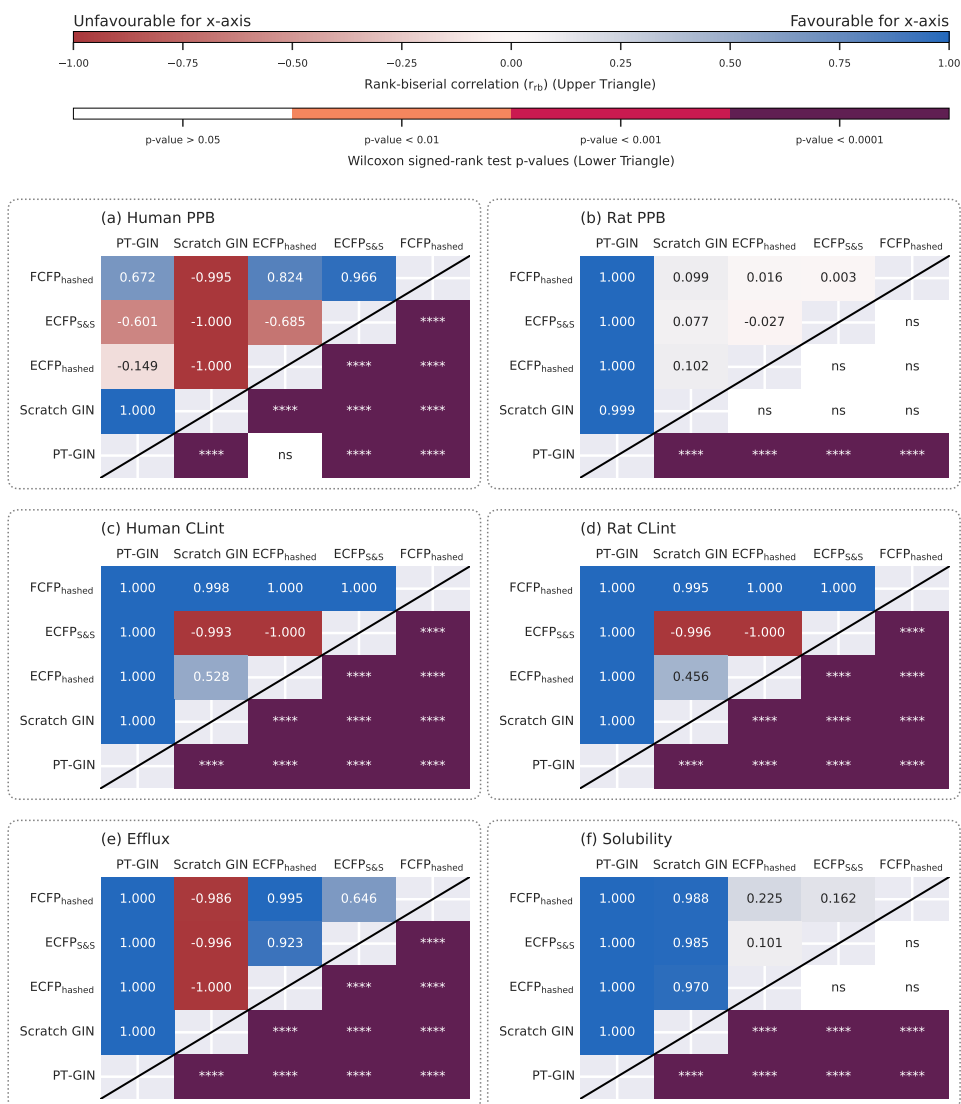


Fig. 2 Rank-biserial coefficient (r_b) effect sizes (upper triangle) and Wilcoxon signed-rank test p -values (lower triangle) comparison of R^2 between methods on Biogen datasets. Tasks are (a) Human Plasma Protein Binding (PPB), (b) Rat PPB, (c) Human Intrinsic Clearance (CLint), (d) Rat CLint, (e) Efflux, (f) Solubility. Featurisation methods shown are GINs trained from scratch (Scratch GIN), ECFP-pre-trained GINs (PT-GIN), hashed Extended-Connectivity Fingerprints (ECFP_{hashed}), hashed Functional-Connectivity Fingerprints (FCFP_{hashed}), and ECFPs folded via Sort & Slice (ECFP_{S&S}). For r_b effect sizes (upper triangle): blue indicates the method on the x -axis has a higher R^2 than the method on the y -axis; red indicates the opposite. For Wilcoxon signed-rank test p -values (lower triangle): white indicates no significant difference and darker indicates a smaller p -value ($n = 199$, $\alpha = 0.05$).

is required. Three-dimensional topological representations, such as E3FPs [36], may be more appropriate pre-training targets for affinity prediction due to the relevance of three-dimensional interactions.

The MUV dataset presents a challenging task; target-specific virtual screening (VS). On MUV tasks, models using PT-GIN and baseline methods for featurisation often predict only negatives, leading to a high proportion of Matthews correlation coefficient (MCC) scores being $MCC = 0$ (Extended Data Fig. 4, Supplementary Information Section 1.4.2). This highlights the challenge of VS in an OOD setting, where 2D ligand topology is likely insufficient for accurately predicting 3D protein-ligand interactions, and class imbalance is expected. For VS, models can be useful for ranking ligands even with low recall at a 0.5 threshold. Enrichment Factors (EF) are a method for determining the quality of ligand ranking by a VS model. $EF_{x\%}$ measures the ratio of active compounds in the top $x\%$ ranked compared to the entire dataset. At all thresholds, there is no clear advantage for any particular method across the different targets; for example, PT-GIN achieves the highest mean $EF_{10\%}$ on only 24% of targets (Fig. 5). This inconsistency is corroborated by Area Under the Precision-recall Curve (AUCPR) scores, with no method achieving the greatest AUCPR on the majority of targets (Extended Data Fig. 4).

Improvements resulting from our pre-training strategy are clearer for toxicity classification. In this case, PT-GIN exhibited the highest AUCPR with a significant difference from all baseline approaches on 7 out of 12 tasks (Extended Data Fig. 6). Across all Tox21 tasks, the effect sizes (r_{rb}) for AUCPR between PT-GIN and baseline methods exceed 0.5 in favour of PT-GIN for 72% of paired comparisons, indicating a strong and frequently observed improvement from pre-training over baseline methods (Supplementary Information Fig. 19). Low MCC scores occur for all approaches, with $\text{mean}(MCC) = 0$ on several tasks and $\text{mean}(MCC) < 0.2$ for 60% of scores (Extended Data Fig. 6), suggest poor performance at a 0.5 classification threshold, although this is not as prevalent as on the MUV dataset.

Overall, these findings suggest that while pre-training on ECFPs can enhance model performance in an out-of-distribution setting, improvements are often data and task-dependent. On regression endpoints, particularly with homogeneous data, pre-training on ECFPs can lead to more robust GNN models, highlighted by consistently favourable effect sizes for PT-GIN on five out of six Biogen tasks. In contrast, the improvements over classical approaches do not occur in settings where the data sources are heterogeneous (e.g., Lipophilicity and affinity datasets), when the endpoint is more complex and may require 3D information (e.g., binding affinity), or when architectural factors may hinder prediction, such as information loss during graph pooling in cases where specific substructures may greatly influence the endpoint (e.g., FreeSolv).

2.2 On data leakage effects in self-supervised pre-training for QSAR

As data leakage is a known issue in ML for drug discovery [37], we investigated the potential effects of pre-training on molecules similar to those in the benchmark data. We generated six QMugs pre-training datasets with molecules 462189 each, using varying Tanimoto similarity thresholds to exclude molecules similar to the benchmark

data, the most stringent being a 0.5 threshold and the most relaxed being a 1.0 threshold (see methods). PT-GIN models were pre-trained on the filtered datasets and benchmarked on Biogen.

On five out of six tasks, there is no clear improvement in performance as data leakage increases. At the greatest dissimilarity, 0.5, PT-GIN exhibits the highest mean R^2 on three tasks, Rat PPB, Efflux, and Solubility (Fig. 3). The model achieving both the highest correlation (ρ) and lowest error (MAPE) is the same only for two tasks, Human PPB and Human CLint (Fig. 3). For Human CLint, the general trend indicates a decrease in R^2 with increased similarity between pre-training and benchmark data (Fig. 4). In contrast, for Human PPB, increasing data leakage is associated with higher performance, with models trained at higher similarity thresholds (0.8–1.0) consistently outperforming those trained at lower thresholds (0.5–0.7) across all three metrics (Fig. 3). The smallest benchmarks exhibit a far greater maximum percentage difference in R^2 , 41% for Human PPB and 34% for Rat PPB, compared to tasks with more data; the next highest is Human CLint at 11%.

The inconsistent, at times negative, effects of data leakage on Biogen ADMET performance scores are counterintuitive, as data leakage is typically associated with overly optimistic model performance [37]. Examining the substructures in the pre-training dataset, QMugs, the number of unique substructures increases asymptotically with more molecules (Extended Data Fig. 7a). In Biogen benchmark data, the proportion of substructures that appear in QMugs pre-training subsets does not substantially change as the Tanimoto similarity filter becomes more relaxed (Extended Data Fig. 7b), i.e., the relative change in substructure content between QMugs subsets is very small. At 462189 molecules, each QMugs subset is likely to contain over 80% of the total substructures that appear in QMugs (Extended Data Fig. 7a). Our filtered QMugs subsets are therefore not OOD relative to the benchmark data with respect to individual substructures, but rather with respect to their combinations.

Pre-training objectives focused on substructure topology can potentially generalise to novel combinations of familiar substructures, as the majority of the underlying substructure content is already observed on the most stringently filtered QMugs subset. Additionally, the robustness of topological pre-training would likely increase as pre-training dataset size, and thus substructure coverage, increases. However, this assumption is unlikely to hold for more extreme similarity thresholds, or more robust similarity measures, where the pre-training data may be more OOD with respect to the benchmark data at the individual substructure level. The expected effect of increased performance with greater data leakage was only observed on Human PPB, the only Biogen task where PT-GIN failed to outperform classical approaches, suggesting that substructure data leakage can still lead to overly optimistic performance. Decreasing R^2 with greater data leakage in some instances could be due to increased variance in molecular topology within the pre-training data, without a corresponding increase in the number of samples.

Our findings suggest that in addition to performance improvements on Biogen ADMET tasks, pre-training on diverse molecular substructures enhances GNN robustness to benchmark data that contains molecules with OOD combinations of

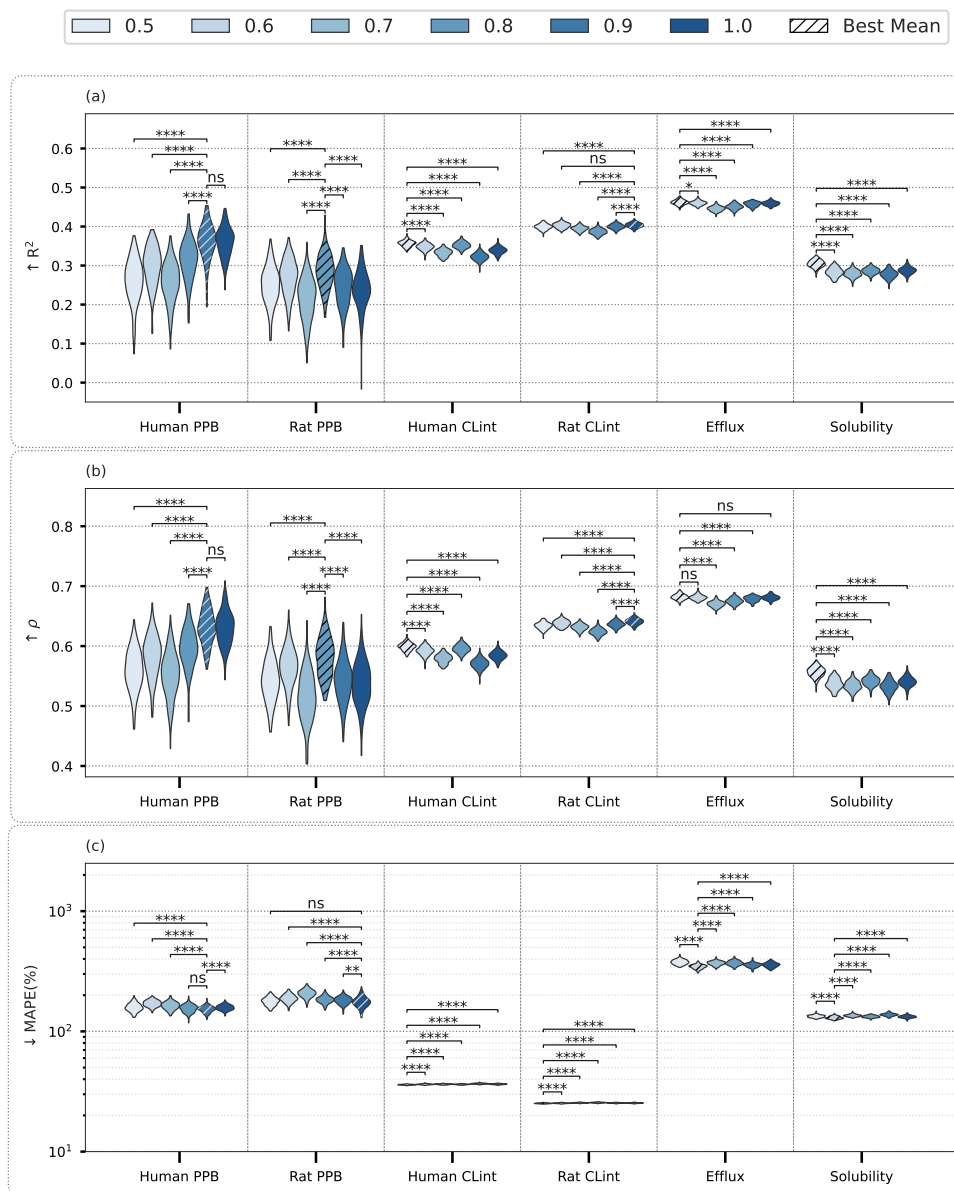


Fig. 3 Biogen ADMET regression task metrics for models pre-trained on data with varying Tanimoto similarity filter thresholds (see 4.2.2). Dissimilarity is greatest between the pre-training and benchmark molecules at the 0.5 threshold; at 1.0, the pre-training data includes molecules that appear in the benchmark data. The metrics shown are coefficient of determination (R^2), Pearson correlation (ρ) and mean absolute percentage error (MAPE) (%). For each task and metric, the approach with the best mean is hatched. Statistical significances, determined by the Wilcoxon signed-rank test ($n = 199$, $\alpha = 0.05$), between the best method by mean and all other approaches are shown with asterisks; ns (not significant) is $p \geq 0.05$; * is $0.01 \leq p < 0.05$; ** is $0.001 \leq p < 0.01$; *** is $0.0001 \leq p < 0.001$; and **** is $p < 0.0001$. Violins are normalised such that each violin has the same maximum width.

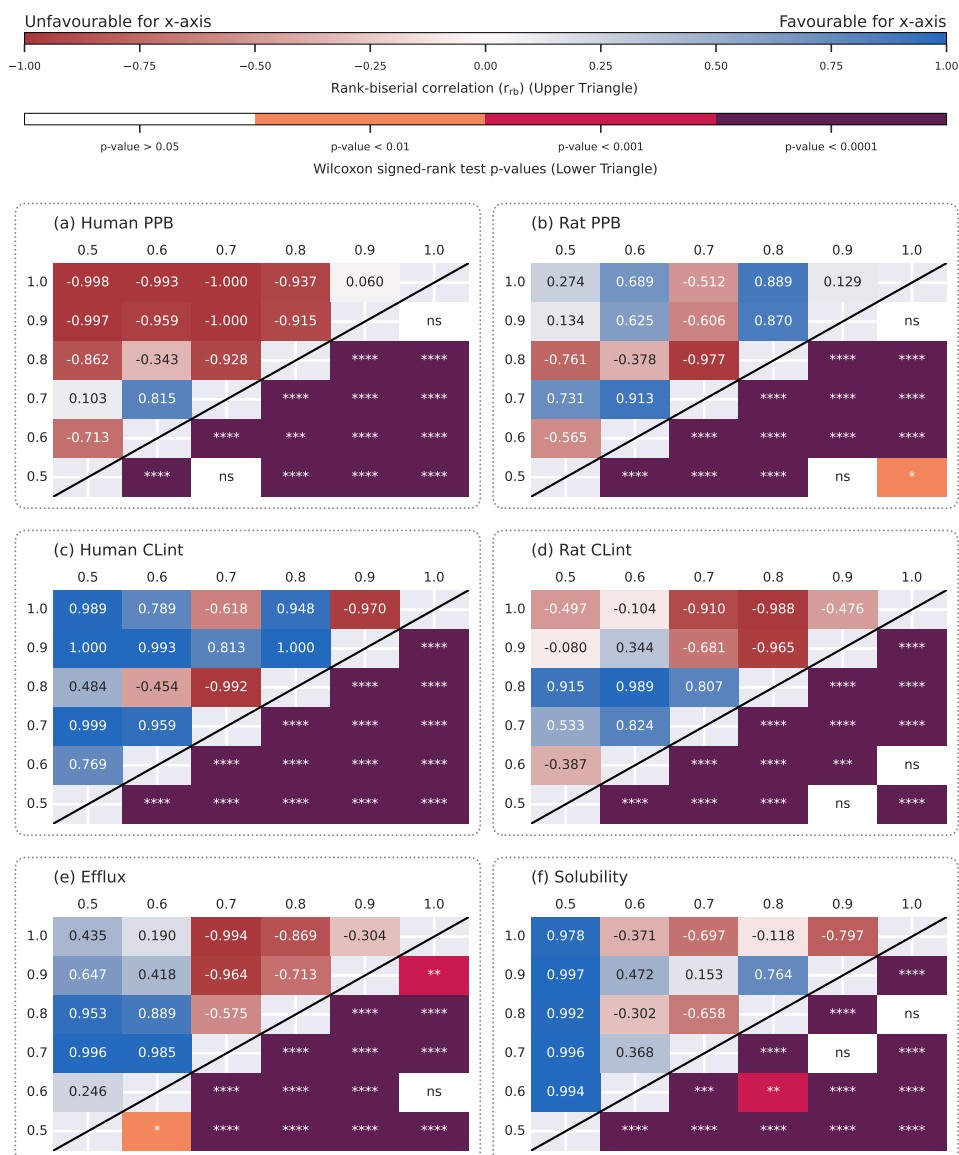


Fig. 4 Rank-biserial coefficient (r_b) effect sizes (upper triangle) and Wilcoxon signed-rank test p -values (lower triangle) comparison of R^2 between PT-GIN models pre-trained on Tanimoto similarity-filtered QMugs data with varying thresholds. Tasks are (a) Human Plasma Protein Binding (PPB), (b) Rat PPB, (c) Human Intrinsic Clearance (CLint), (d) Rat CLint, (e) Efflux, (f) Solubility. Methods shown are PT-GIN models pre-trained on filtered QMugs data at varying similarity filter thresholds; 0.5 indicates that no molecule with Tanimoto similarity > 0.5 to any molecule in the benchmark data was included in the pre-training data. For r_b effect sizes (upper triangle): blue indicates the method on the x -axis has a higher R^2 than the method on the y -axis; red indicates the inverse. For Wilcoxon signed-rank test p -values (lower triangle): white indicates no significant difference and darker indicates a smaller p -value ($n = 199$, $\alpha = 0.05$). See methods for details.

substructures. Data leakage may have a limited impact on models pre-trained to predict molecular topology, as the substructure corpus is already well-represented by a dissimilar set of molecules. While the filtered subsets may not be OOD with respect to individual substructures, they remain OOD in terms of molecular composition. This suggests that our pre-training strategy effectively learns to generalise from substructure components to entire molecules, more so than GNNs trained from scratch, achieving robustness that would likely increase with even larger pre-training datasets.

3 Discussion

Graph neural networks have historically struggled to outperform classical molecular featurisation methods for QSAR [16–18]. Our work demonstrates that self-supervised pre-training on Extended-Connectivity Fingerprints is a simple, robust, and effective strategy for improving the OOD performance of GNNs on key QSAR tasks. By leveraging the structural information encoded in ECFPs, ECFP-pre-trained GINs significantly outperformed GINs trained from scratch and classical fingerprinting methods on a diverse set of ADMET tasks in the Biogen dataset, validated through rigorous statistical testing. As such, enhancement of GNNs for drug discovery can be achieved without increasing model complexity or utilizing large, noisy, labelled pre-training datasets.

However, the success of our pre-training approach is not ubiquitous. On tasks directly relating to 3D protein-ligand interactions, such as binding affinity prediction and virtual screening, PT-GINs fail to outperform baseline approaches. Additionally, PT-GINs struggle to compete on more heterogeneous datasets, such as the Lipophilicity benchmark. Prior work has shown that binding affinity datasets aggregated from multiple sources can be noisy and inconsistent, suggesting that data heterogeneity leads to inaccurate performance estimates [38]. These limitations highlight that a more nuanced approach to pre-training may be necessary. For example, it would be preferable to select self-supervised targets based on the specific characteristics of the downstream task, such as E3FPs for 3D molecular representations. Given enough data, a multi-task learning approach could also be beneficial; however, this may not entirely mitigate an erroneous relationship between one or more pre-training tasks and downstream performance.

In addition, we analysed the impact of pre-training data leakage, in the form of topological similarity (ECFP₄₂₀₄₈ Tanimoto similarity), on model performance. Our findings suggest that increased data leakage between benchmark and pre-training datasets has an inconsistent impact on model performance; for example, on a subset of Biogen tasks, greater data leakage showed an association with reduced performance or no association at all. This is counterintuitive, as data leakage typically leads to overly optimistic performance. This suggests that as long as the pre-training corpus is large enough to contain a diverse vocabulary of chemical substructures, a GNN could learn to generalise to novel substructure combinations. The focus for self-supervised pre-training may not need to be on finding perfectly matched pre-training domains, but rather on maximizing the diversity of chemical motifs. However, this may not hold for more extreme similarity thresholds, or more robust similarity measures, where

the pre-training data may be more OOD with respect to the benchmark data at the substructure level.

Looking forward, our topological pre-training approach can be adopted as a simple method to boost GNN performance on relevant ADMET tasks in an OOD setting, even with limited pre-training data. Our findings suggest that pre-training on topological fingerprints can enhance GNN robustness in regimes with lower data overlap between pre-training and benchmark datasets. Additionally, our substructure-based tokenisation also allows for interpretable model insights, via permutation importance (Supplementary Information Section 1.3). Secondly, multi-modal self-supervised pre-training strategies should be developed, such as pre-training on topological fingerprints and PDVs simultaneously, although this would require more data than used in this study. Thirdly, pre-training strategies should be devised and implemented with consideration for the specific characteristics of the downstream task or tasks. Finally, the community would benefit greatly from standardised pre-training protocols, including curated and consistent pre-training datasets that consider downstream tasks. Such standards would clarify the strengths and detriments of different pre-training approaches for molecular property prediction, and are vital for fairly assessing performance differences between pre-training methods.

4 Methods

For package versions used here, see Supplementary Information Table 2.

4.1 Datasets

4.1.1 QMugs for self-supervised pre-training

Self-supervised pre-training of GINs was performed on QMugs [39], a chemical dataset consisting of 665k molecules. QMugs contains drug-like molecules and prior work has shown QMugs has potential for pre-training [40], and the dataset is large enough, even with similarity filtering, for pre-training, whilst being small enough for extensive ablation studies.

4.1.2 Benchmarking datasets: Biogen, MoleculeNet, ChEMBL

The primary benchmarking dataset used in this study was Biogen [31], a dataset of 3521 molecules with six ADMET tasks. Its prediction tasks are plasma protein binding (PPB) in human and rat blood plasma, intrinsic hepatic clearance (CL_{int}) in human and rat liver, a measure of active transport, as an efflux ratio, by multidrug resistance protein 1, and aqueous solubility. Biogen was selected for its high degree of experimental consistency, with all assays conducted under uniform conditions, ensuring data homogeneity [31].

We also used a subset of MoleculeNet [32] for benchmarking, including three regression datasets, ESOL [41], FreeSolv [42], and Lipophilicity [33], and two binary classification datasets, MUV [43], and Tox21 [44]. ESOL is a solubility task, although solubility values extend outside the typical range for drug-like molecules [45]. FreeSolv is a benchmark for free energies of solvation. MUV contains 17 target-specific,

imbalanced virtual screening (VS) tasks. Tox21 contains 12 toxicity tasks from high-throughput *in vitro* assays. Whilst MoleculeNet benchmarks have been subject to critique [12, 13, 23, 46], they are still widely used for ADMET benchmarking and can highlight potential model weaknesses, hence their inclusion.

We also benchmarked the featurisation methods on the challenging task of target-specific binding affinity prediction. We employed two datasets derived from ChEMBL [33] that were previously used in another systematic QSAR study [16]. The target associated with the first dataset is Dopamine Receptor D2 (DRD2), a regulatory signalling protein implicated in neurological disorders [47], and the second dataset is Factor X_A, a pharmaceutical protein target for anticoagulation therapies [48].

4.2 Data preparation and splitting

All Tanimoto similarities were determined using hashed ECFPs, with chirality set to True, radius = 2, and fpsize = 2048.

4.2.1 Molecular standardisation

All pre-training and benchmark molecules were standardised using RDKit [49]:

1. Molecules were checked for incorrect chemistry by `Chem.SanitizeMol`.
2. Hydrogens and disconnected metal atoms were removed using `Cleanup` from `rdMolStandardize`.
3. Disconnected fragments were removed using `FragmentParent` from `rdMolStandardize`.
4. Molecules were neutralised using `Uncharger` from `rdMolStandardize`.
5. The canonical tautomer was determined using `TautomerEnumerator` from `rdMolStandardize`. Tautomerisation was performed without Sp3 stereochemistry removal to retain chirality.

Any molecule that failed to pass standardisation was excluded.

4.2.2 Pre-training data filtering based on Tanimoto similarities with benchmarking data

QMugs was filtered into different subsets for pre-training to investigate the effects of data leakage, in the form of topological similarity, on model performance. Tanimoto similarities were determined between the molecules in QMugs, and the molecules in every benchmark dataset used (Biogen, MUV, Tox21, etc.). Any molecule in the QMugs dataset with > 0.5 similarity to any benchmark molecule was excluded, leaving an initial pre-training dataset of 462189 molecules. For data leakage analysis, the same process was repeated with similarity thresholds of 0.6, 0.7, 0.8, 0.9, and 1.0. To ensure that the same number of molecules were used for pre-training at each similarity threshold, random uniform sampling without replacement was performed on the filtered QMugs subsets to yield 462189 molecules for each threshold.

4.2.3 QMugs duplicate screening

There are approximately 10k duplicate SMILES strings in QMugs [39]; on inspection many of the duplicates are enantiomers with missing chirality flags. To avoid loss of chirality and erroneous duplicates, we used the ChEMBL IDs saved to QMugs to retrieve SMILES strings directly from ChEMBL v.27 [33].

4.2.4 Repeated cross-validated splitting for out-of-distribution testing

Pairwise Tanimoto similarities between molecules were calculated for each benchmark dataset. Distances between molecules were calculated as $\text{dist} = 1 - \text{Tanimoto similarity}$. Benchmark datasets were individually clustered using Butina clustering on Tanimoto distances [29] with a cutoff of 0.65; the default cutoff in Useful RDKit Utils [50]. We chose Butina for its speed, ease of implementation in RDKit, and the evenly sized clusters it produces. Here we assume that molecules within the same cluster are more similar to each other than to molecules in other clusters, enabling us to split the data by clusters for out-of-distribution (OOD) train-test sets. Datasets were repeatedly resampled into k-folds, similarly to Ash et al. (2024) [22], for grouped cross-validation; we used `GroupKFold` for regression tasks and `StratifiedGroupKFold` for classification tasks [51]. We used 200 repetitions, each time splitting into five folds of held-out clusters with a new random seed, producing an abundant number of 1000 train-test splits for each dataset.

One repetition was used for hyperparameter tuning, the remaining 199 were used for model evaluation. Even with stratifying by target label, the MUV dataset occasionally produced folds with no positive labels due to extreme class imbalance; test metrics over these folds were ignored (see Supplementary Information Table 4).

4.2.5 Units

For binding affinity tasks, DRD2 and Factor X_A , affinity was converted from nM to M before calculating pKi. For ESOL, $\log(S)$ was converted from $\log(M)$ to $\log(\mu M)$, such that drug-like solubility values were comparable to the Biogen Solubility dataset.

4.3 Model architecture and training strategy

4.3.1 Graph Neural Networks

Graph neural networks were implemented using PyTorch and PyTorch Geometric [52, 53]. In this work, we used Graph Isomorphism Networks (GINs) [30] as our GNN architecture of choice. Our study was motivated by the fact that previous work has suggested that GINs without pre-training struggle to outperform classical featurisation methods for QSAR [16].

4.3.2 Substructure tokenisation

Molecular graph featurisation is commonly performed with curated atom-level descriptors, [16, 20, 54]. An alternative approach is to embed the molecule based on atom

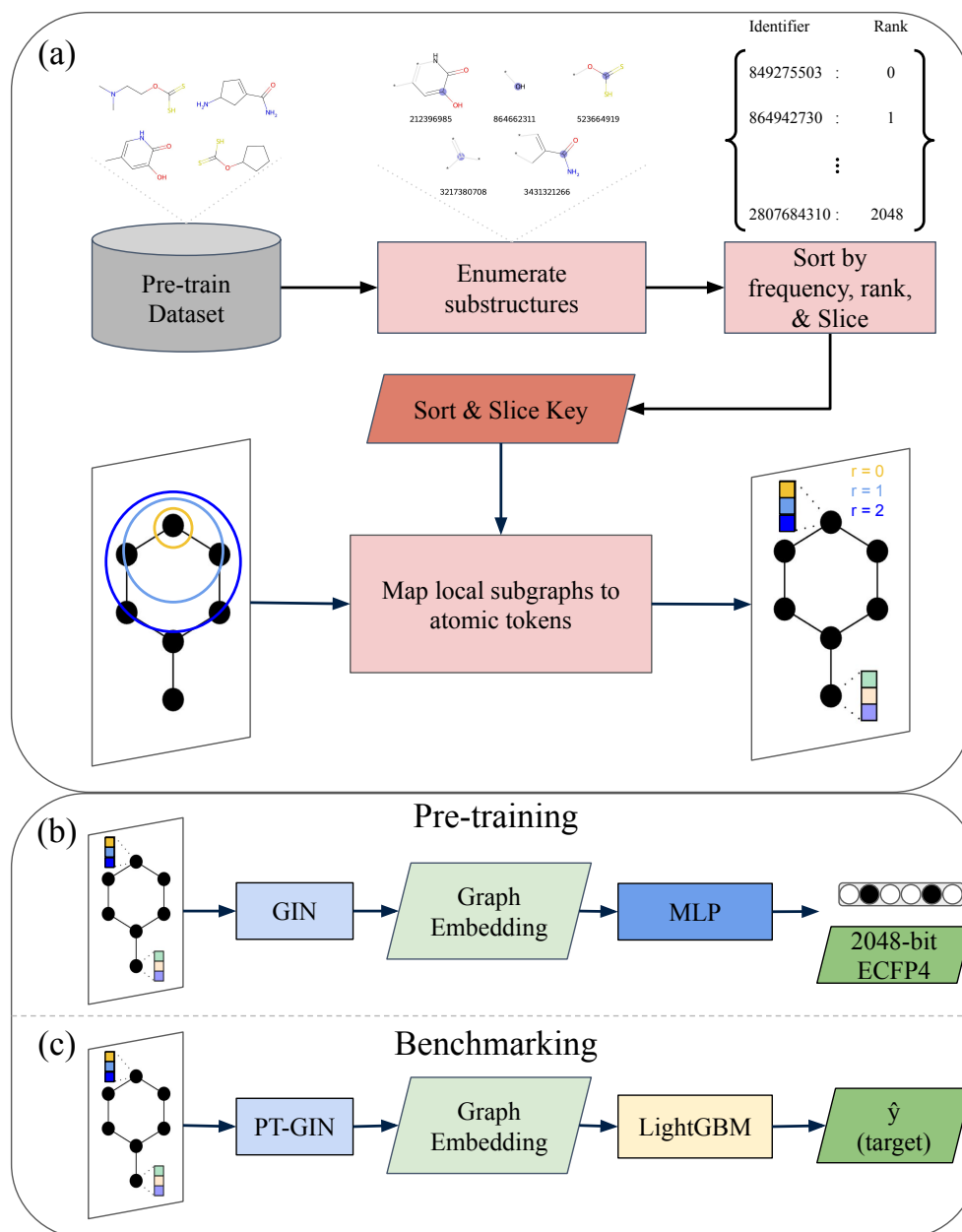


Fig. 5 Model architecture. (a) Substructure tokenisation of molecular graphs through Sort & Slice (S&S) [34]. (b) Self-supervised, topological pre-training pipeline. GINs were pre-trained to predict hashed ECFPs [14] from substructure tokenised molecular graphs. (c) Benchmarking pipeline with frozen ECFP-pre-trained GINs and LightGBM [35].

types. For MolE, Méndez-Lucio et al. [2] introduced encoding via Daylight atomic invariants, i.e., via Morgan identifiers with radius $r = 0$ [14]. We explored taking this further by expanding this strategy to include local substructures beyond a radius of $r = 0$ and assigning multiple tokens to each atom, one token for each radius (Fig. 5a). We refer to this process as substructure tokenisation. The vocabulary is generated by ranking Morgan identifiers based on their frequency in the pre-training corpus, a process analogous to the creation of corpus-dependent vocabularies in NLP.

Circular substructure vocabularies for pre-training datasets were determined by applying Sort and Slice (S&S) [34] (Supplementary Information Algorithm 1). S&S is an easy-to-implement and bit-collision-free alternative to hash-based folding for the vectorisation of the set of ECFP-substructures detected in an input molecule. S&S first sorts ECFP substructures according to their relative prevalence in a given set of training compounds and then incorporates only the most frequent substructures into the final binary fingerprint. This vectorisation technique has been shown to robustly outperform hash-based folding at a diverse set of molecular property prediction tasks. Here, we apply S&S in a new context; rather than mapping substructures to positions in a binary fingerprint, we map substructures to tokens for vectorial embedding. We use S&S, with `chirality` as `True`, to

1. sort circular substructures by the number of molecules they appear in,
2. map each circular substructure to a rank, and
3. slice the vocabulary to a specific size.

Substructure enumeration was performed using the Morgan Fingerprint generator in RDKit [49]. By applying the S&S algorithm to the substructure vocabulary, we were able to rank the substructures by frequency and control the vocabulary size. The maximum radius of circular substructures and vocabulary size were treated as hyperparameters.

Each substructure in the vocabulary was mapped to a learnable embedding using `torch.nn.Embedding`, producing a node embedding shape of (i, j, k) , where:

- i is the number of atoms in the molecular graph,
- j is the number of radii, e.g. $j = 2$ for a maximum radius of $r = 1$ with a zero radius and a one radius token, and
- k is the embedding size.

Multi-token node embeddings were concatenated to produce one unified vectorial representation per atom with shape (i, jk) . Thus, the atomic embedding shape varied depending on the maximum radius of the tokenisation strategy (Supplementary Information Table 7).

For PT-GIN, vocabulary sizes used were 1024, 2048, 4096, 8192, and 16384. Vocabularies beyond 16384 were not considered due to increasingly high parameter counts relative to the amount of pre-training data (e.g. 16384 tokens of 128 dimensions would be 2M parameters). Maximum radii of $r = 0$, $r = 1$, and $r = 2$ were explored.

For Scratch GIN, the hyperparameter search space was constrained to smaller vocabulary sizes and maximum radii, as preliminary work suggested that larger vocabularies and maximum radii did not lead to performance improvements, and increased

the computational cost of training. This was likely due to insufficient benchmark data for Scratch GIN to generalise in an OOD setting with larger vocabularies, and small benchmark datasets leading to more rare substructures being included at training and unused during inference. The vocabularies sizes explored in hyperparameter tuning were constrained to 16, 32, 64 for radius $r = 0$, and 16, 32, 64 for radius $r = 1$. We initially explored using atomic features, such as atomic mass, and tokens based only on atom type, however, performance was notably improved by tokenising based on local atomic environments.

The resulting substructure vocabularies were used to featurise molecular graphs by assigning substructure tokens to each atom for all radii up to the pre-defined maximum (Supplementary Information Algorithm 2). Unknown substructures were assigned an UNK token.

4.3.3 Self-supervised pre-training

GINs were pre-trained (PT-GIN) on hashed two radius 2048-bit ECFPs fingerprints (ECFP₄₂₀₄₈), with chirality as True. This approach is malleable as the label can be substituted for different topological targets, such as Functional-Connectivity Fingerprints (FCFP). The ECFP₄₂₀₄₈ bit-vectors were used as a multi-task binary classification target for self-supervised pre-training (Fig. 5b). While hash-based vectorisation is prone to noise resulting from bit collisions [34], it allows compression of the constituent circular substructures in a molecule into a smaller vectorial representation. Prediction of the entire substructure corpus without hashed-based folding would require substantially more trainable parameters within our neural architecture. We did not use S&S to fold ECFPs for pre-training, as S&S would have removed rare substructures entirely. Loss was calculated using binary cross-entropy with balanced class weighting [51].

Pre-training GIN hyperparameters were explored using Optuna [55] with 50 trials and 5-fold CV on the 0.5 similarity-filtered QMugs subset, aiming to maximise mean test fold AUROC on ECFP₄₂₀₄₈ predictions. Splitting was performed via KFold [51]. For pre-training hyperparameters, see Supplementary Information Tables 5,6. The initial learning rate was calculated as $lr = d_{model}^{-0.5}$, where d is the number of model parameters; the learning rate scheduler was a hyperparameter. After tuning, the best hyperparameters were used to pre-train models on the entirety of each pre-training subset.

During pre-training, the output from the last GIN layer was the input for the prediction head. Multiple models with varying vocabulary sizes and maximum radii were pre-trained; for benchmarking, each pre-trained model was used for featurisation in individual LightGBM hyperparameter tuning runs on the benchmark data (see Section 4.4.5). The ECFP-pre-trained GIN with the best performance during the benchmark hyperparameter tuning was selected for testing on the remaining 199 train-test splits, using the model with the highest mean R^2 for regression tasks and AUCPR for classification tasks. For each task, models pre-trained for investigating threshold similarity used the same radius and vocabulary size as the PT-GIN pre-trained on the 0.5 filtered dataset with the highest R^2 .

4.4 Benchmarking Setup

4.4.1 Pre-trained embedding representations

In downstream benchmarking, frozen embeddings from pre-trained models were used as molecular representations (Fig. 5c); PT-GIN outputs after each layer were pooled and concatenated to form a global molecular embedding. The graph pooling method (mean, max, etc.) was a hyperparameter (Supplementary Information Table 5). Fine tuning was explored in preliminary experiments, however, end-to-end fine tuning was computationally expensive relative to using frozen embeddings with Light Gradient-Boosted Machines (LightGBM) [35], and the benefits were often negligible. In some cases fine tuning was even detrimental. This was most likely due to the small size of the downstream benchmark datasets relative to the parameter count in the pre-trained model, even when only fine tuning a subset of model layers. As such, we used frozen pre-trained embeddings as inputs for LightGBM models in downstream benchmarking. The use of pre-trained embeddings with LightGBM additionally allowed for a more direct comparison with baseline molecular fingerprint representations, such as hashed ECFPs with LightGBM, as differences in performance could not be attributed to differences between architectures.

As an initial baseline, we conducted experiments pre-training an autoencoder, equivalent in parameter count to PT-GIN, to reconstruct ECFP bit vectors. However, this approach underperformed compared to models using graph-based representations.

4.4.2 Baseline classical featurisation methods

For our baseline comparisons, we used static circular topological fingerprints, namely fingerprinting methods vectorised via classical hash-based folding, including Extended-Connectivity Fingerprints (ECFP_{hashed}) [14] and Functional-Connectivity Fingerprints (FCFP_{hashed}). Furthermore, we employed ECFPs vectorised via Sort & Slice (ECFP_{S&S}) [34]. The S&S vectorisation technique for ECFPs has been shown to lead to robustly superior predictive performance over classical hash-based folding on various molecular property prediction tasks [34].

For classical fingerprinting methods, the radius and bit-vector lengths were treated as hyperparameters. We used radii of $r = 1$ and $r = 2$, and bit-vector lengths of 1024 and 2048. For each train-test split, features with zero variance in the training split were excluded.

4.4.3 Light gradient-boosted machines

Light Gradient-Boosted Machines (LightGBM) models were used in benchmarking for their training speed and efficiency [35]. Frozen ECFP-pre-trained GIN embeddings were used as inputs with LightGBM models to evaluate PT-GIN as a featurisation method (Fig. 5c). All classical baseline molecular representations were fed into a LightGBM model as well for downstream prediction (Fig. 6a).

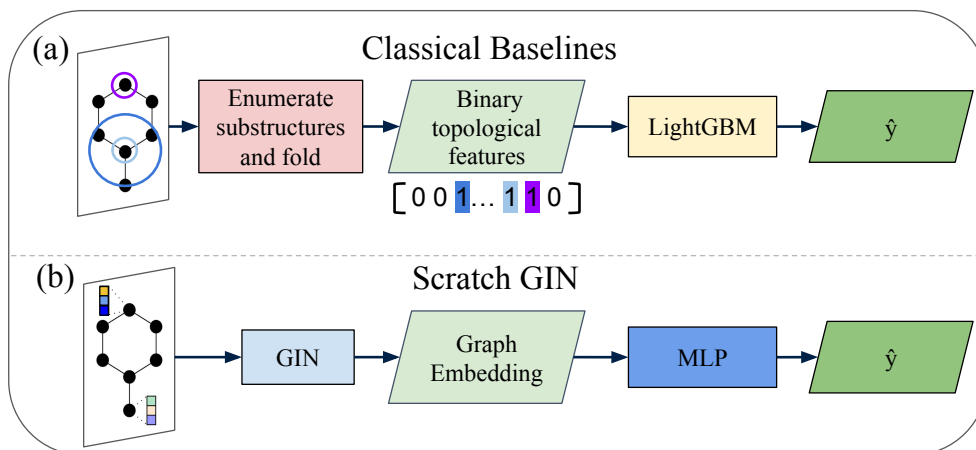


Fig. 6 Baseline pipelines for (a) classical fingerprinting methods ($\text{ECFP}_{\text{hashed}}$, $\text{FCFP}_{\text{hashed}}$, $\text{ECFP}_{\text{S\&S}}$), and (b) Scratch GIN.

4.4.4 Scratch GIN

Scratch GINs were trained with a standard multi-layer perceptron prediction head (Fig. 6b). Regression tasks were trained using mean squared error (MSE) loss. On binary classification tasks, models were trained using binary cross-entropy loss with balanced class weighting. We explored retraining LightGBM models on Scratch GIN embeddings for a consistent pipeline across all molecular representations, however, there was no noticeable difference in performance between end-to-end Scratch GIN models and LightGBMs trained on the same embeddings.

As Scratch GIN models were computationally expensive to repeatedly train compared to the LightGBM used with the other approaches, comparisons to Scratch GINs were limited to Biogen.

4.4.5 Benchmark hyperparameter tuning

Hyperparameter tuning for benchmarking was performed on a held-out 5-fold CV using Optuna [55] with 50 trials. Ideally, nested cross-validation would have been used for tuning and evaluation. However, this would have required approximately 250,000 additional model fits (50 trials by 5 folds per trial by 1000 train-test splits) per baseline per dataset, which was computationally prohibitive. Regression tasks were optimised for minimizing mean absolute error (MAE) and binary classification tasks were optimised for minimizing binary cross-entropy loss. As nested cross-validated tuning would require many iterations over the full 1000 train-test splits, tuning was instead performed on one 5-fold set produced from repeated cross-validated splitting; these folds were excluded from the final evaluation.

The search space for Scratch GIN was constrained such that the number of parameters would be approximately the same order of magnitude as the dataset size. This was done to mitigate overfitting and improve generalisation in an OOD setting, as well

as to reduce the computational cost of training. Additionally, initial testing suggested that over-parameterisation did not lead to performance improvements of Scratch GIN, likely due to the small size of the benchmark datasets. For the search spaces used for LightGBM and Scratch GIN see Supplementary Information Tables 7-12.

4.5 Model evaluation and statistical testing

Ash et al. (2024) suggested performing multiple comparisons over repeated k-fold cross-validation (CV) splits [22]. We adopted this approach for our benchmarking, using 5-fold CV repeated 200 times for 1000 train-test splits with each dataset. As each of the folds within a single repeat are mutually exclusive—samples in one fold cannot appear in another—test sets within the same CV repeat are not independent. To account for this, we averaged the performance metrics across all folds for each repeat and assume each CV repeat is independent. Additionally, performances from individual test splits can be noisy, especially for small datasets; averaging performances over folds reduces the impact of this noise on statistical tests. The 5-fold split used for hyperparameter tuning and excluded from model evaluations, resulting in 199 samples for each statistical test.

Tukey’s Honest Significant Difference Test (Tukey’s HSD), a statistical test for evaluating whether performance differences between ML models are significant, and Cohen’s d , an effect size measure, are commonly appropriate for comparing models [22]. Both of these approaches are parametric, assuming sample sets are normally distributed and that the variance within each group is comparable. However, we found that metric distributions can be non-normally distributed, particularly for performance scores with values close to upper and lower bounds of the metric, such as AUCPR (Supplementary Information Section 1.4). Additionally, Tukey’s HSD assumes independent observations [56]; however, our results are paired, since the performance of a model on a CV repeat can be directly matched to the performance of a different model on the same CV repeat. Therefore, we used the Wilcoxon signed-rank test [57], a non-parametric test for evaluating differences in mean ranks between paired samples. To account for multiple comparisons, we applied the Bonferroni correction method to adjust p -values and reduce the occurrence of type I error [58]. Wilcoxon with Bonferroni correction was computed using scikit-posthocs [59]. Even when normality held, we still used non-parametric tests and effect sizes for consistency across tasks and metrics. To evaluate the effect size between models, we used rank-biserial correlation (r_{rb}) [60, 61], a paired non-parametric measure of effect size. Given two models, A and B , r_{rb} in our case can be interpreted as

$$r_{rb} = P(A > B) - P(A < B)$$

where $P(A > B)$ is the probability of model A outperforming model B on the same CV repeat, and $P(B > A)$ is the reverse. Assuming that $P(A = B) \approx 0$ (i.e., ties of model performance are rare),

$$P(A > B) = \frac{r_{rb} + 1}{2}.$$

For example, an $r_{rb} = 0.5$ would mean that model A outperforms model B on 75% of the CV repeats.

For MAPE calculations, we excluded test samples with $y = 0$, as MAPE is undefined for these samples due to the division by zero ($\text{MAPE} = 100 \cdot \frac{1}{n} \sum_{i=1}^n \left| \frac{y_i - \hat{y}_i}{y_i} \right|$). This resulted in two samples being excluded from the Biogen Solubility, one from ESOL, two from FreeSolv, and three from Lipophilicity.

4.6 Substructure Importance

As S&S maps substructures to bits and PT-GIN maps substructures to tokens, it is possible to measure the relative importance of substructures for both methods.

For $\text{ECFP}_{\text{S\&S}}$, substructure importance was determined by measuring change in performance upon permutation as described previously [62], using R^2 for regression AUCPR for classification.

For PT-GIN models, substructure importance was determined by iteratively permuting the embedding for each substructure token (Supplementary Information Algorithm 3-4). To prevent token prevalence within each graph from influencing the measurement, a fixed number of permutations, equal to the node embedding dimension, were distributed across every instance of a token in a graph; an alternative approach would be to permute a maximum of one node in each graph. By permuting substructure embeddings, we had a heuristic for substructure importance that we could compare directly to S&S.

Feature importance was performed with LightGBM models over one of the 5-fold cross-validated splits used in benchmark evaluation, and repeated five times on each train-test split, totalling 25 iterations. See Supplementary Information Section 1.3 for Substructure Importance results and analysis.

Declarations

Supplementary information Additional discussion, figures, tables, and algorithms are provided in the Supplementary Information.

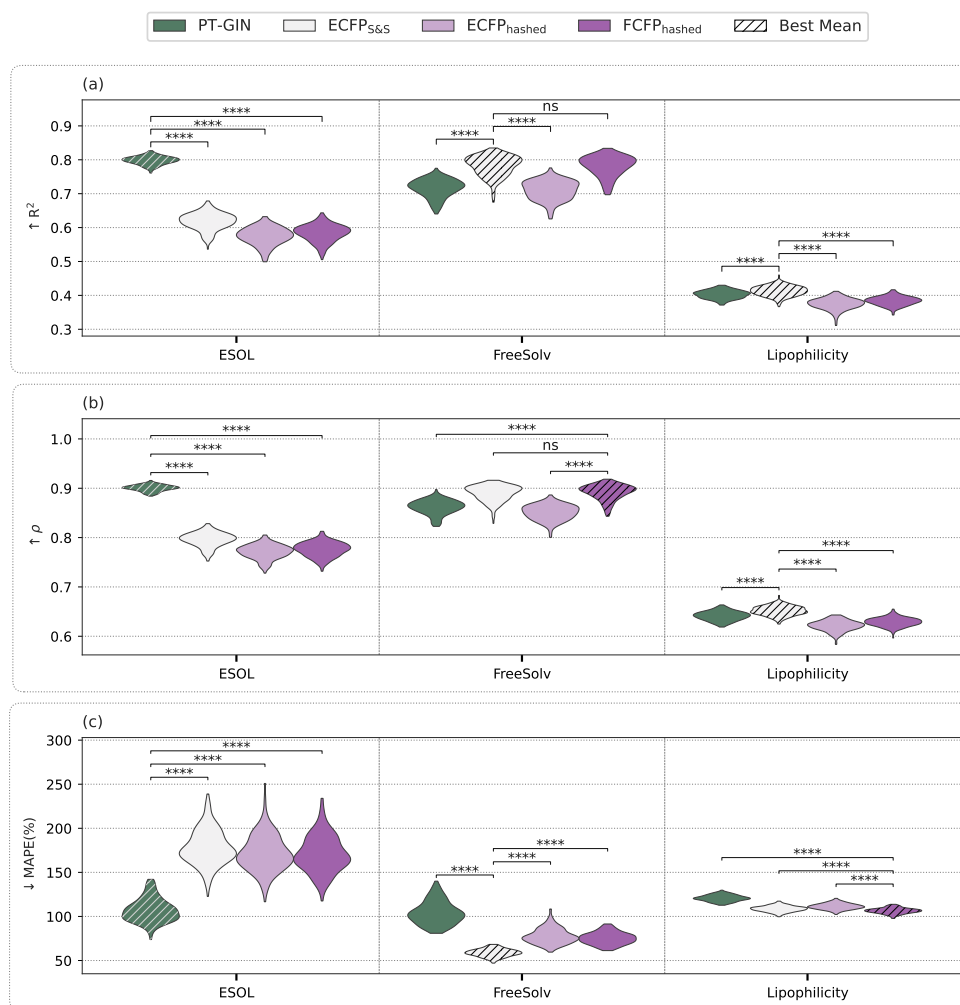
Acknowledgements This work was supported by the Engineering and Physical Sciences Research Council [Grant number EP/W524311/1] and Lhasa Ltd.

Ethics declarations The authors declare no competing interests.

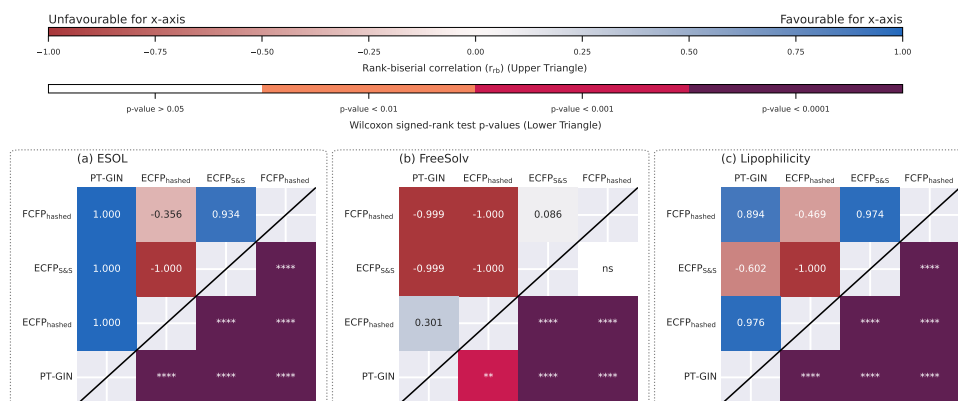
Code and Data availability The code and data for this work are available at: <https://github.com/oxpig/topological-pretraining>.

Author contributions S.M-K. and M.D. conceptualised the study. S.M-K. developed the methodology, performed the experiments, and analysed the results. G.M.M., C.M.D., T.H., and S.W. supervised the project. All authors discussed the results and contributed to the interpretation. S.M-K. wrote the manuscript with editorial input from all authors.

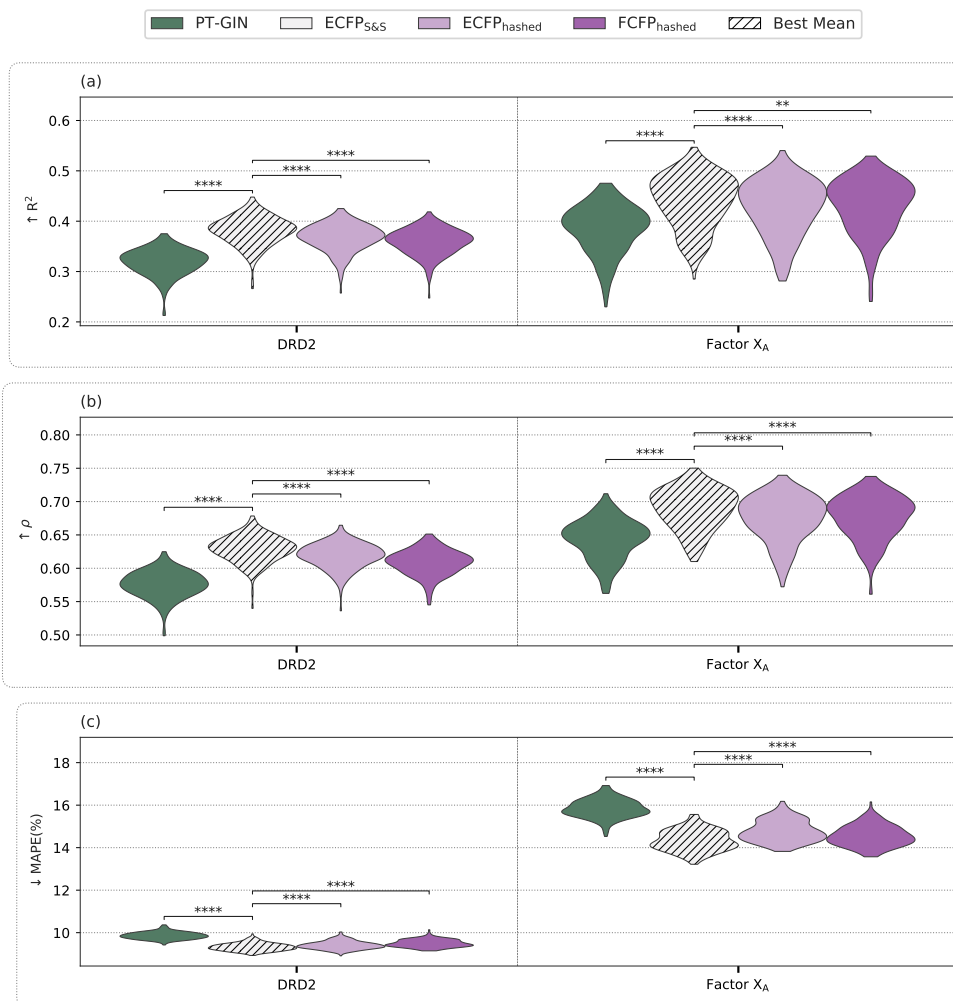
Extended Data



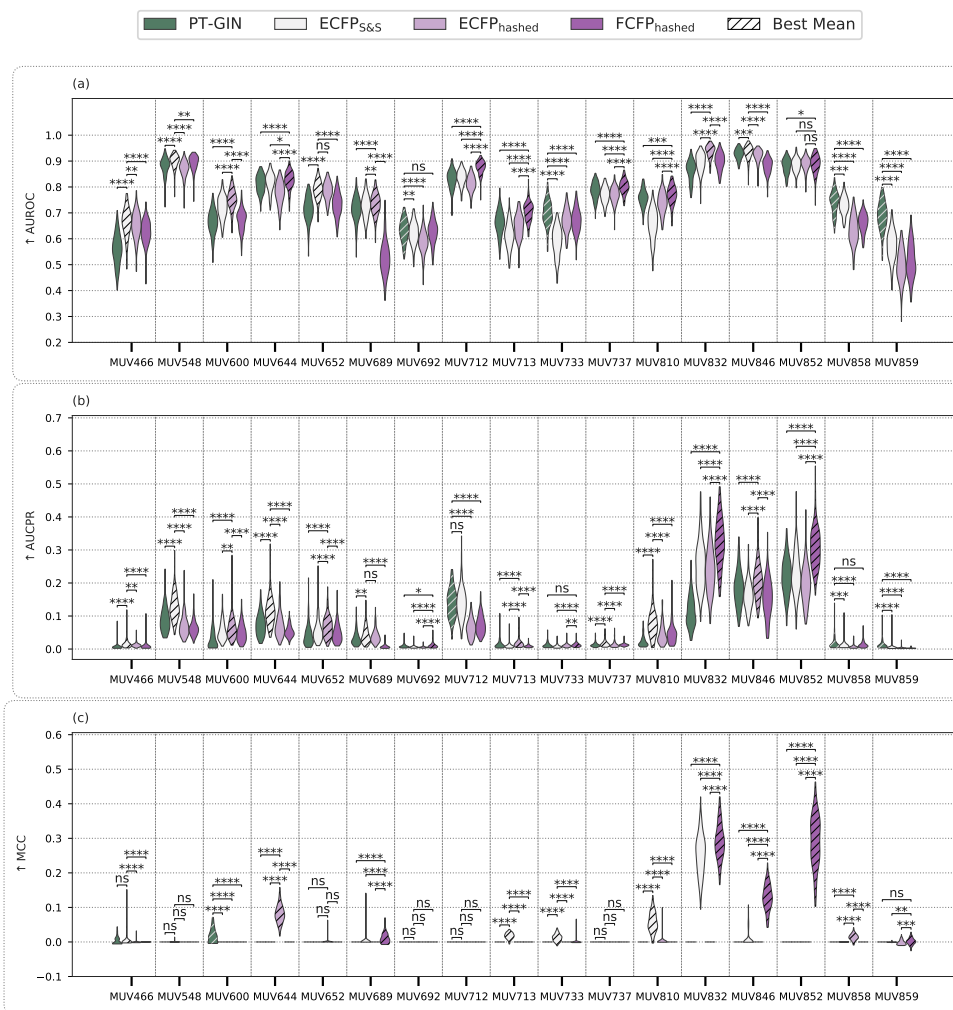
Extended Data Figure 1 Performance metrics on MoleculeNet ADMET regression tasks. Datasets shown are ESOL, FreeSolv, and Lipophilicity. The metrics shown are (a) Coefficient of Determination ($\uparrow R^2$), (b) Pearson Correlation ($\uparrow \rho$) and (c) mean absolute percentage error (\downarrow MAPE (%)). Featurisation methods shown are ECFP-pre-trained GINs (PT-GIN), hashed Extended-Connectivity Fingerprints (ECFP_{hashed}), hashed Functional-Connectivity Fingerprints (FCFP_{hashed}), and ECFPs folded via Sort & Slice (ECFP_{S&S}). Statistical significances, determined by the Wilcoxon signed-rank test ($n = 199$, $\alpha = 0.05$), between the best method by mean and all other approaches are shown with asterisks; ns (not significant) is $p \geq 0.05$; * is $0.01 \leq p < 0.05$; ** is $0.001 \leq p < 0.01$; *** is $0.0001 \leq p < 0.001$; and **** is $p < 0.0001$. Violins are normalised such that each violin has the same maximum width.



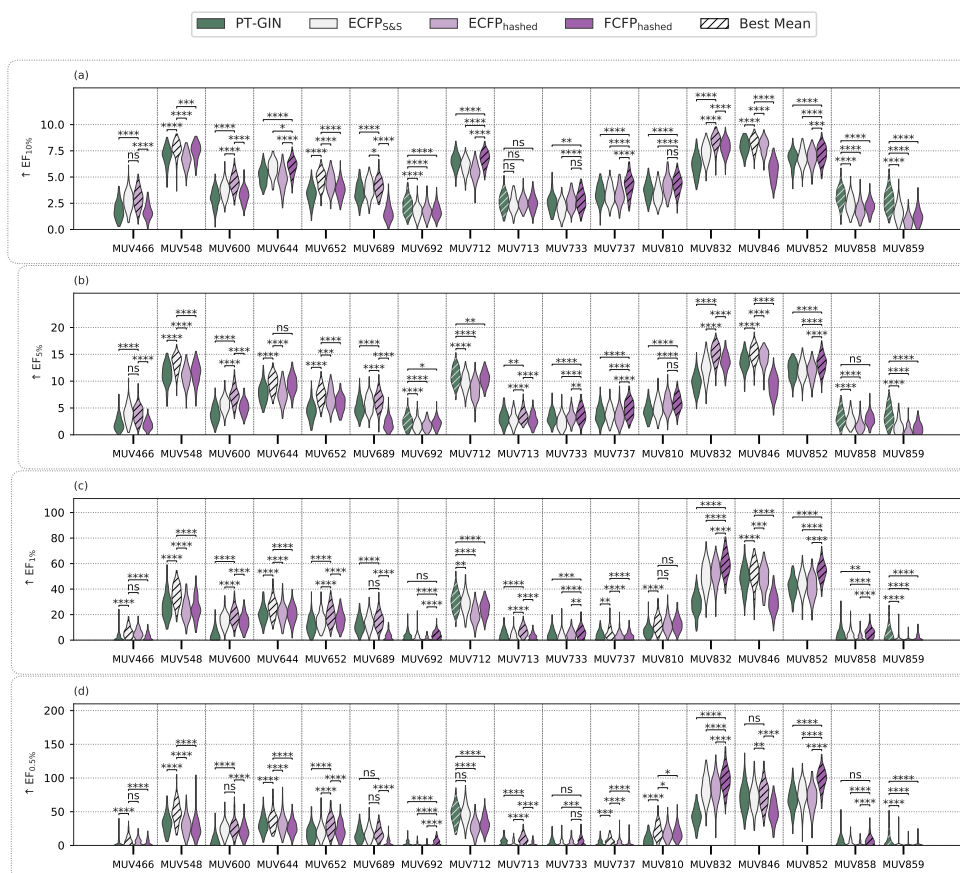
Extended Data Figure 2 Rank-biserial coefficient ($r_{r,b}$) effect sizes (upper triangle) and Wilcoxon signed-rank test p -values (lower triangle) comparison of R^2 between methods on MoleculeNet regression datasets. Datasets are (a) ESOL, (b) FreeSolv, and (c) Lipophilicity. Featurisation methods shown are ECFP-pre-trained GINs (PT-GIN), hashed Extended-Connectivity Fingerprints (ECFP_{hashed}), hashed Functional-Connectivity Fingerprints (FCFP_{hashed}), and ECFPs folded via Sort & Slice (ECFP_{S&S}). For $r_{r,b}$ effect sizes (upper triangle): blue indicates the method on the x -axis has a higher R^2 than the method on the y -axis; red indicates the inverse. For Wilcoxon signed-rank test p -values (lower triangle): white indicates no significant difference and darker indicates a smaller p -value ($n = 199$, $\alpha = 0.05$).



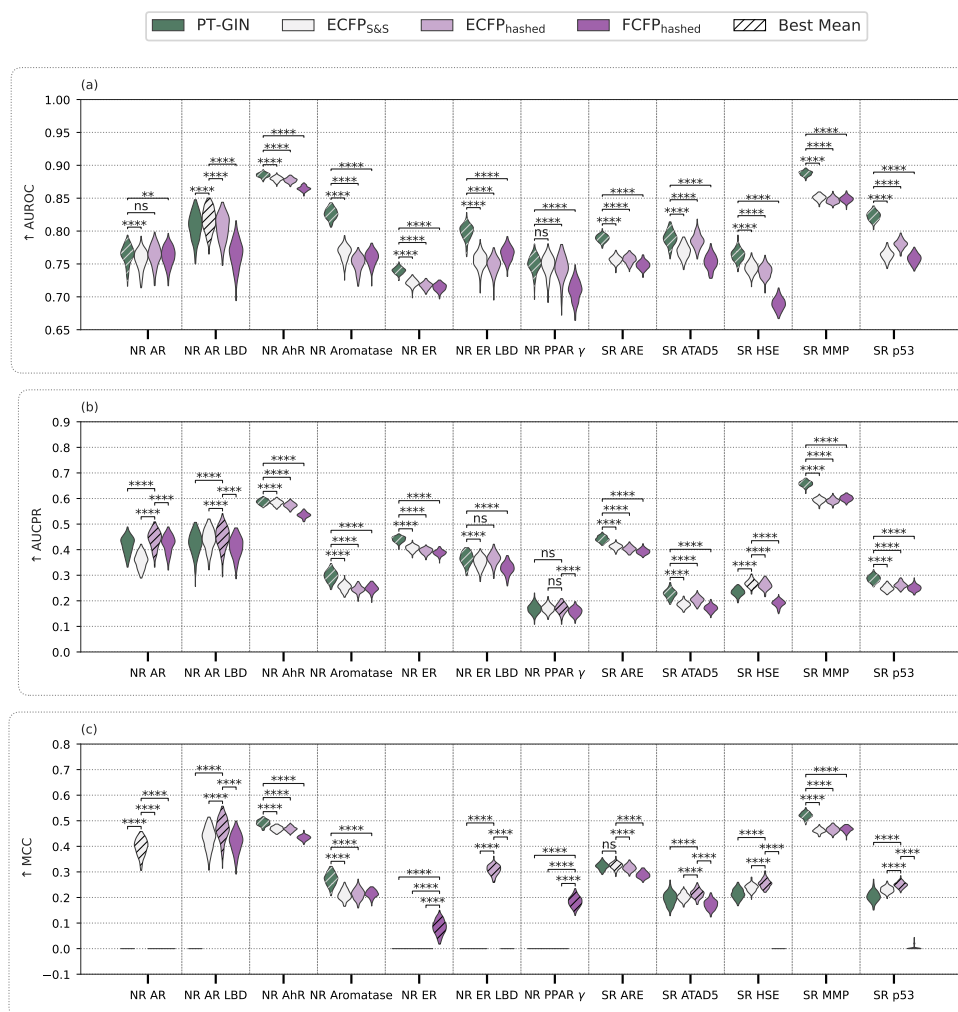
Extended Data Figure 3 Performance metrics on ChEMBL binding affinity tasks. Datasets shown are DRD2 and Factor X_A . The metrics shown are (a) $\uparrow R^2$, (b) Pearson Correlation ($\uparrow \rho$) and (c) mean absolute percentage error (\downarrow MAPE (%)). Featurisation methods shown are ECFP-pre-trained GINs (PT-GIN), hashed Extended-Connectivity Fingerprints (ECFP_{hashed}), hashed Functional-Connectivity Fingerprints (FCFP_{hashed}), and ECFPs folded via Sort & Slice (ECFP_{S&S}). For each task and metric, the approach with the best mean is hatched. Statistical significances, determined by the Wilcoxon signed-rank test ($n = 199$, $\alpha = 0.05$), between the best method by mean and all other approaches are shown with asterisks; ns (not significant) is $p \geq 0.05$; * is $0.01 \leq p < 0.05$; ** is $0.001 \leq p < 0.01$; *** is $0.0001 \leq p < 0.001$; and **** is $p < 0.0001$. Violins are normalised such that each violin has the same maximum width.



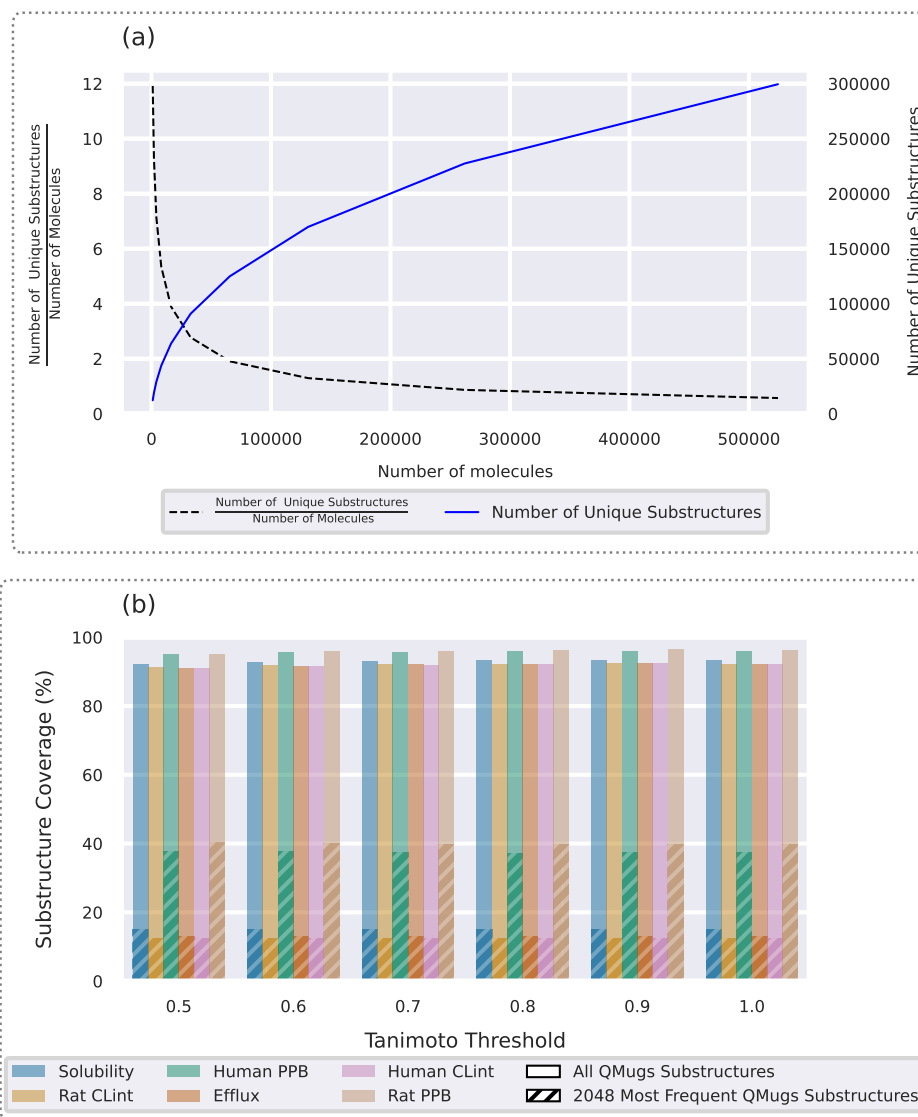
Extended Data Figure 4 Performance metrics on MUV virtual screening tasks. The metrics shown are Area Under the Receiver Operating Characteristic (\uparrow AUROC), Area Under the Precision-Recall Curve (\uparrow AUCPR), and Matthews correlation coefficient (\uparrow MCC). Featurisation methods shown are ECFP-pre-trained GINs (PT-GIN), hashed Extended-Connectivity Fingerprints (ECFP_{hashed}), hashed Functional-Connectivity Fingerprints (FCFP_{hashed}), and ECFPs folded via Sort & Slice (ECFP_{S&S}). Statistical significances, determined by the Wilcoxon signed-rank test ($n = 199$, $\alpha = 0.05$), between the best method by mean and all other approaches are shown with asterisks; ns (not significant) is $p \geq 0.05$; * is $0.01 \leq p < 0.05$; ** is $0.001 \leq p < 0.01$; *** is $0.0001 \leq p < 0.001$; and **** is $p < 0.0001$. Violins are normalised such that each violin has the same maximum width.



Extended Data Figure 5 Enrichment factors at 10%, 5%, 1%, and 0.05% on MUV virtual screening tasks. Featurisation methods shown are ECFP-pre-trained GINs (PT-GIN), hashed Extended-Connectivity Fingerprints ($\text{ECFP}_{\text{hashed}}$), hashed Functional-Connectivity Fingerprints ($\text{FCFP}_{\text{hashed}}$), and ECFPs folded via Sort & Slice ($\text{ECFP}_{\text{S\&S}}$). For each task and metric, the approach with the best mean is hatched. Statistical significances, determined by the Wilcoxon signed-rank test ($n = 199$, $\alpha = 0.05$), between the best method by mean and all other approaches are shown with asterisks; ns (not significant) is $p \geq 0.05$; * is $0.01 \leq p < 0.05$; ** is $0.001 \leq p < 0.01$; *** is $0.0001 \leq p < 0.001$; and **** is $p < 0.0001$. Sample sizes (i.e., the number of train-test splits) are in the Supplementary Information Section 4. Violins are normalised such that each violin has the same maximum width.



Extended Data Figure 6 Performance metrics on Tox21 binary toxicity tasks. The metrics shown are Area Under the Receiver Operating Characteristic (\uparrow AUROC), Area Under the Precision-Recall Curve (\uparrow AUCPR), and Matthews correlation coefficient (\uparrow MCC). Featurisation methods shown are ECFP-pre-trained GINs (PT-GIN), hashed Extended-Connectivity Fingerprints (ECFP_{hashed}), hashed Functional-Connectivity Fingerprints (FCFP_{hashed}), and ECFPs folded via Sort & Slice (ECFP_{S&S}). For each task and metric, the approach with the best mean is hatched. Statistical significances, determined by the Wilcoxon signed-rank test ($n = 199$, $\alpha = 0.05$), between the best method by mean and all other approaches are shown with asterisks; ns (not significant) is $p \geq 0.05$; * is $0.01 \leq p < 0.05$; ** is $0.001 \leq p < 0.01$; *** is $0.0001 \leq p < 0.001$; and **** is $p < 0.0001$. Violins are normalised such that each violin has the same maximum width.



Extended Data Figure 7 QMugs substructure content. (a) The number of molecules in randomly selected subsets of QMugs (x -axis) versus the ratio of the number of unique substructures to the number of molecules (black, dashed, left y -axis) and the total number of unique substructures (blue, right y -axis). As the number of molecules increases, the ratio of the number of unique substructures to the number of molecules decreases. (b) The proportion of substructures in the Biogen subsets that appear in the Tanimoto filtered QMugs pre-training subsets. Substructure coverage is expressed as a percentage. Coverage using the entirety of QMugs (no hatching) and only the 2048 most frequent substructures in the QMugs subset (hatched) are shown. The coverage of Biogen substructures does not substantially change with increased data leakage. Substructures were determined using RDKit with a radius $r = 2$, chirality as True, and Daylight atomic invariants.

References

- [1] Koohy, H. The rise and fall of machine learning methods in biomedical research. *F1000Research* **6**, 2012 (2018). URL <https://f1000research.com/articles/6-2012/v2>.
- [2] Méndez-Lucio, O., Nicolaou, C. A. & Earnshaw, B. MolE: A foundation model for molecular graphs using disentangled attention. *Nature Communications* **15**, 9431 (2024). URL <https://doi.org/10.1038/s41467-024-53751-y>.
- [3] Kearnes, S., McCloskey, K., Berndl, M., Pande, V. & Riley, P. Molecular graph convolutions: Moving beyond fingerprints. *Journal of Computer-Aided Molecular Design* **30**, 595–608 (2016). URL <https://doi.org/10.1007/s10822-016-9938-8>.
- [4] Yang, K. *et al.* Analyzing Learned Molecular Representations for Property Prediction. *Journal of Chemical Information and Modeling* **59**, 3370–3388 (2019). URL <https://doi.org/10.1021/acs.jcim.9b00237>.
- [5] Jaeger, S., Fulle, S. & Turk, S. Mol2vec: Unsupervised Machine Learning Approach with Chemical Intuition. *Journal of Chemical Information and Modeling* **58**, 27–35 (2018). URL <https://doi.org/10.1021/acs.jcim.7b00616>.
- [6] Hu, W. *et al.* Strategies for Pre-training Graph Neural Networks (2020). [arXiv:1905.12265](https://arxiv.org/abs/1905.12265).
- [7] Hou, Z. *et al.* GraphMAE: Self-Supervised Masked Graph Autoencoders. In *Proceedings of the 28th ACM SIGKDD Conference on Knowledge Discovery and Data Mining*, 594–604 (ACM, 2022). URL <https://doi.org/10.1145/3534678.3539321>.
- [8] Wang, Y., Wang, J., Cao, Z. & Barati Farimani, A. Molecular contrastive learning of representations via graph neural networks. *Nature Machine Intelligence* **4**, 279–287 (2022). URL <https://doi.org/10.1038/s42256-022-00447-x>.
- [9] Ying, C. *et al.* Do transformers really perform badly for graph representation? In *Proceedings of the 35th International Conference on Neural Information Processing Systems*, Vol. 34, 28877–28888 (Curran Associates Inc., 2021). URL <https://dl.acm.org/doi/10.5555/3540261.3542473>.
- [10] Aitken, M., Roland, A. & Kleinrock, M. Global Trends in R&D 2025: Progress in recapturing momentum in biopharma innovation. Tech. Rep., IQVIA Institute for Human Data Science (2025). URL <https://www.iqvia.com/insights/the-iqvia-institute/reports-and-publications/reports/global-trends-in-r-and-d-2025>.
- [11] Crusius, D., Cipcigan, F. & C. Biggin, P. Are we fitting data or noise? Analysing the predictive power of commonly used datasets in Drug-, Materials-,

- and molecular-discovery. *Faraday Discussions* **256**, 304–321 (2025). URL <https://doi.org/10.1039/D4FD00091A>.
- [12] Kretschmer, F., Seipp, J., Ludwig, M., Klau, G. W. & Böcker, S. Coverage bias in small molecule machine learning. *Nature Communications* **16**, 554 (2025). URL <https://doi.org/10.1038/s41467-024-55462-w>.
- [13] Wallach, I. & Heifets, A. Most Ligand-Based Classification Benchmarks Reward Memorization Rather than Generalization. *Journal of Chemical Information and Modeling* **58**, 916–932 (2018). URL <https://doi.org/10.1021/acs.jcim.7b00403>.
- [14] Rogers, D. & Hahn, M. Extended-connectivity fingerprints. *Journal of Chemical Information and Modeling* **50**, 742–754 (2010). URL <https://doi.org/10.1021/ci100050t>.
- [15] McGibbon, M. *et al.* From intuition to AI: Evolution of small molecule representations in drug discovery. *Briefings in Bioinformatics* **25**, bbad422 (2024). URL <https://doi.org/10.1093/bib/bbad422>.
- [16] Dablander, M., Hanser, T., Lambiotte, R. & Morris, G. M. Exploring QSAR models for activity-cliff prediction. *Journal of Cheminformatics* **15**, 47 (2023). URL <https://doi.org/10.1186/s13321-023-00708-w>.
- [17] Jiang, D. *et al.* Could graph neural networks learn better molecular representation for drug discovery? A comparison study of descriptor-based and graph-based models. *Journal of Cheminformatics* **13**, 12 (2021). URL <https://doi.org/10.1186/s13321-020-00479-8>.
- [18] Xia, J. *et al.* *Understanding the Limitations of Deep Models for Molecular property prediction: Insights and Solutions*. In *Proceedings of the 37th International Conference on Neural Information Processing Systems* (Curran Associates Inc., 2023). URL <https://dl.acm.org/doi/10.5555/3666122.3668949>.
- [19] Sypetkowski, M. *et al.* On the Scalability of GNNs for Molecular Graphs (2024). [arXiv:2404.11568](https://arxiv.org/abs/2404.11568).
- [20] Zaidi, S. *et al.* Pre-training via Denoising for Molecular Property Prediction (2022). [arXiv:2206.00133](https://arxiv.org/abs/2206.00133).
- [21] Burns, J., Zalte, A. & Green, W. Descriptor-based Foundation Models for Molecular Property Prediction (2025). [arXiv:2506.15792](https://arxiv.org/abs/2506.15792).
- [22] Ash, J. R. *et al.* Practically significant method comparison protocols for machine learning in small molecule drug discovery. *Journal of Chemical Information and Modeling* **65**, 9398–9411 (2025). URL <https://doi.org/10.1021/acs.jcim.5c01609>.

- [23] Wognum, C. *et al.* A call for an industry-led initiative to critically assess machine learning for real-world drug discovery. *Nature Machine Intelligence* **6**, 1120–1121 (2024). URL <https://doi.org/10.1038/s42256-024-00911-w>.
- [24] van Tilborg, D., Rossen, L. & Grisoni, F. Molecular deep learning at the edge of chemical space. *Nature Machine Intelligence* 1–13 (2026).
- [25] Barker, A., Kettle, J. G., Nowak, T. & Pease, J. E. Expanding medicinal chemistry space. *Drug Discovery Today* **18**, 298–304 (2013). URL <https://www.sciencedirect.com/science/article/pii/S1359644612003650>.
- [26] Klarner, L. *et al.* *Drug Discovery under Covariate Shift with Domain-Informed Prior Distributions over Functions*. In *Proceedings of the 40th International Conference on Machine Learning*, 17176–17197 (PMLR, 2023). URL <https://proceedings.mlr.press/v202/klarner23a.html>.
- [27] Guo, Q., Hernandez-Hernandez, S. & Ballester, P. J. *Scaffold Splits Overestimate Virtual Screening Performance*. In *Artificial Neural Networks and Machine Learning – ICANN 2024*, 58–72 (Springer Nature Switzerland, Cham, 2024). URL https://doi.org/10.1007/978-3-031-72359-9_5.
- [28] Guo, Q., Hernandez-Hernandez, S. & Ballester, P. J. UMAP-based clustering split for rigorous evaluation of AI models for virtual screening on cancer cell lines. *Journal of Cheminformatics* **17**, 94 (2025). URL <https://doi.org/10.1186/s13321-025-01039-8>.
- [29] Butina, D. Unsupervised Data Base Clustering Based on Daylight’s Fingerprint and Tanimoto Similarity: A Fast and Automated Way To Cluster Small and Large Data Sets. *Journal of Chemical Information and Computer Sciences* **39**, 747–750 (1999). URL <https://doi.org/10.1021/ci9803381>.
- [30] Xu, K., Hu, W., Leskovec, J. & Jegelka, S. How Powerful are Graph Neural Networks? (2019). [arXiv:1810.00826](https://arxiv.org/abs/1810.00826).
- [31] Fang, C. *et al.* Prospective Validation of Machine Learning Algorithms for Absorption, Distribution, Metabolism, and Excretion Prediction: An Industrial Perspective. *Journal of Chemical Information and Modeling* **63**, 3263–3274 (2023). URL <https://doi.org/10.1021/acs.jcim.3c00160>.
- [32] Wu, Z. *et al.* MoleculeNet: A benchmark for molecular machine learning. *Chemical Science* **9**, 513–530 (2018). URL <https://doi.org/10.1039/C7SC02664A>.
- [33] Zdrazil, B. *et al.* The ChEMBL Database in 2023: A drug discovery platform spanning multiple bioactivity data types and time periods. *Nucleic Acids Research* **52**, D1180–D1192 (2024). URL <https://doi.org/10.1093/nar/gkad1004>.

- [34] Dablander, M., Hanser, T., Lambiotte, R. & Morris, G. M. Sort & Slice: A simple and superior alternative to hash-based folding for extended-connectivity fingerprints. *Journal of Cheminformatics* **16**, 135 (2024). URL <https://doi.org/10.1186/s13321-024-00932-y>.
- [35] Ke, G. *et al.* *LightGBM: A Highly Efficient Gradient Boosting Decision Tree*. In *Proceedings of the 31st International Conference on Neural Information Processing Systems*, 3149–3157 (Curran Associates, Inc., 2017). URL <https://dl.acm.org/doi/10.5555/3294996.3295074>.
- [36] Axen, S. D. *et al.* A Simple Representation of Three-Dimensional Molecular Structure. *Journal of Medicinal Chemistry* **60**, 7393–7409 (2017). URL <https://doi.org/10.1021/acs.jmedchem.7b00696>.
- [37] Bennett, J. *et al.* Guiding questions to avoid data leakage in biological machine learning applications. *Nature Methods* **21**, 1444–1453 (2024). URL <https://doi.org/10.1038/s41592-024-02362-y>.
- [38] Landrum, G. A. & Riniker, S. Combining IC50 or Ki Values from Different Sources Is a Source of Significant Noise. *Journal of Chemical Information and Modeling* **64**, 1560–1567 (2024).
- [39] Isert, C., Atz, K., Jiménez-Luna, J. & Schneider, G. QMugs, quantum mechanical properties of drug-like molecules. *Scientific Data* **9**, 273 (2022). URL <https://doi.org/10.1038/s41597-022-01390-7>.
- [40] Raja, A. *et al.* *On the Effectiveness of Quantum Chemistry Pre-training for Pharmacological Property Prediction*. In *ICML 2024 AI for Science Workshop* (2024). URL <https://openreview.net/forum?id=ffSLXl666Q>.
- [41] Delaney, J. S. ESOL: Estimating Aqueous Solubility Directly from Molecular Structure. *Journal of Chemical Information and Computer Sciences* **44**, 1000–1005 (2004). URL <https://doi.org/10.1021/ci034243x>.
- [42] Mobley, D. L. & Guthrie, J. P. FreeSolv: A database of experimental and calculated hydration free energies, with input files. *Journal of Computer-Aided Molecular Design* **28**, 711–720 (2014). URL <https://doi.org/10.1007/s10822-014-9747-x>.
- [43] Rohrer, S. G. & Baumann, K. Maximum unbiased validation (MUV) data sets for virtual screening based on PubChem bioactivity data. *Journal of Chemical Information and Modeling* **49**, 169–184 (2009). URL <https://doi.org/10.1021/ci8002649>.
- [44] Richard, A. M. *et al.* The Tox21 10K Compound Library: Collaborative Chemistry Advancing Toxicology. *Chemical Research in Toxicology* **34**, 189–216 (2021). URL <https://doi.org/10.1021/acs.chemrestox.0c00264>.

- [45] Rytting, E., Lentz, K. A., Chen, X.-Q., Qian, F. & Venkatesh, S. Aqueous and cosolvent solubility data for drug-like organic compounds. *The AAPS Journal* **7**, 10 (2005). URL <https://doi.org/10.1208/aapsj070110>.
- [46] Walters, W. P. We Need Better Benchmarks for Machine Learning in Drug Discovery. Practical Cheminformatics Blog (2023). URL <https://practicalcheminformatics.blogspot.com/2023/08/we-need-better-benchmarks-for-machine.html>.
- [47] Pan, X. *et al.* Dopamine and Dopamine Receptors in Alzheimer’s Disease: A Systematic Review and Network Meta-Analysis. *Frontiers in Aging Neuroscience* **11** (2019). URL <https://doi.org/10.3389/fnagi.2019.00175>.
- [48] Alexander, J. H. & Singh, K. P. Inhibition of Factor Xa. *American Journal of Cardiovascular Drugs* **5**, 279–290 (2005). URL <https://doi.org/10.2165/00129784-200505050-00001>.
- [49] Landrum, G. RDKit: Open-source cheminformatics (2024). URL <https://www.rdkit.org/>. Version 2024.09.1.
- [50] Walters, W. P. Useful RDKit Utils (2024). URL https://github.com/PatWalters/useful_rdkit_utils.
- [51] Pedregosa, F. *et al.* Scikit-learn: Machine Learning in Python. *Journal of Machine Learning Research* **12**, 2825–2830 (2011). URL <http://jmlr.org/papers/v12/pedregosa11a.html>.
- [52] Paszke, A. *et al.* *PyTorch: An Imperative Style, High-Performance Deep Learning Library*. In *Proceedings of the 33rd International Conference on Neural Information Processing Systems*, Vol. 32 (Curran Associates, Inc., 2019). URL <https://dl.acm.org/doi/10.5555/3454287.3455008>.
- [53] Fey, M. & Lenssen, J. E. Fast Graph Representation Learning with PyTorch Geometric (2019). [arXiv:1903.02428](https://arxiv.org/abs/1903.02428).
- [54] Gilmer, J., Schoenholz, S. S., Riley, P. F., Vinyals, O. & Dahl, G. E. *Neural message passing for quantum chemistry*. In *Proceedings of the 34th International Conference on Machine Learning*, Vol. 70, 1263–1272 (PMLR, 2017). URL <http://proceedings.mlr.press/v70/gilmer17a.html>.
- [55] Akiba, T., Sano, S., Yanase, T., Ohta, T. & Koyama, M. *Optuna: A next-generation hyperparameter optimization framework*. In *Proceedings of the 25th ACM SIGKDD International Conference on Knowledge Discovery & Data Mining*, KDD ’19, 2623–2631 (ACM, 2019). URL <https://doi.org/10.1145/3292500.3330701>.

- [56] SciPy. Scipy.stats.tukey_hsd — tukey’s honestly significant difference test — SciPy v1.17.0 Documentation (2023). URL https://docs.scipy.org/doc/scipy/reference/generated/scipy.stats.tukey_hsd.html.
- [57] Wilcoxon, F. Individual Comparisons by Ranking Methods. *Biometrics Bulletin* **1**, 80–83 (1945). URL <https://doi.org/10.2307/3001968>.
- [58] Armstrong, R. A. When to use the Bonferroni correction. *Ophthalmic and Physiological Optics* **34**, 502–508 (2014). URL <https://doi.org/10.1111/opo.12131>.
- [59] Maksim Terpilovskii. Scikit-posthocs: Statistical post-hoc analysis and outlier detection algorithms v.0.11.4 (2025).
- [60] Kerby, D. S. The Simple Difference Formula: An Approach to Teaching Non-parametric Correlation. *Comprehensive Psychology* **3**, 11.IT.3.1 (2014). URL <https://journals.sagepub.com/doi/10.2466/11.IT.3.1>.
- [61] Cureton, E. E. Rank-biserial correlation. *Psychometrika* **21**, 287–290 (1956). URL <https://doi.org/10.1007/BF02289138>.
- [62] Breiman, L. Random Forests. *Machine Learning* **45**, 5–32 (2001). URL <https://doi.org/10.1023/A:1010933404324>.

**Supplementary Information for: On Improving Graph Neural Networks for
QSAR by Pre-training on Extended-Connectivity Fingerprints**

Supplementary Information 1 Supplementary Results

Supplementary Information 1.1 Metric Violin Plots

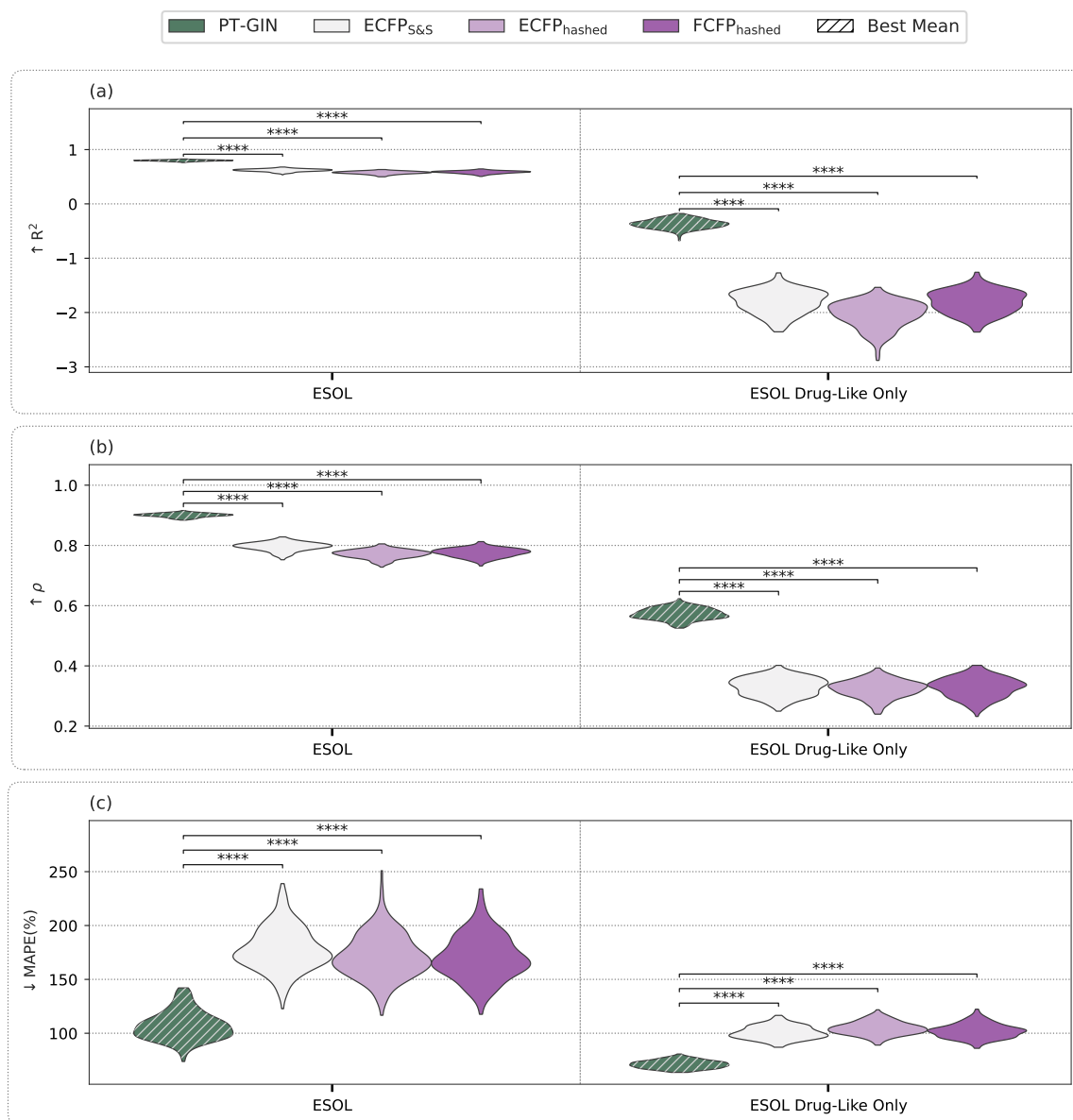


Figure 1: Performance metrics on ESOL aqueous solubility with all molecules (ESOL) and only molecules with a drug-like solubility (ESOL Drug-like Only) ($0 < \log_{10}(S(\mu\text{M})) < 3$). The metrics shown are (a) coefficient of determination ($\uparrow R^2$), (b) Pearson correlation ($\uparrow \rho$) and (c) mean absolute percentage error ($\downarrow \text{MAPE}(\%)$). Featurisation methods shown are ECFP-pretrained GINs (PT-GIN), hashed Extended-Connectivity Fingerprints (ECFP_{hashed}), hashed Functional-Connectivity Fingerprints (FCFP_{hashed}), and ECFPs folded via Sort & Slice (ECFP_{S&S}). For each task and metric, the approach with the best mean is hatched. Statistical significances, determined by the Wilcoxon signed-rank test ($n = 199$, $\alpha = 0.05$), between the best method by mean and all other approaches are shown with asterisks; ns (not significant) is $p \geq 0.05$; * is $0.01 \leq p < 0.05$; ** is $0.001 \leq p < 0.01$; *** is $0.0001 \leq p < 0.001$; and **** is $p < 0.0001$. Violins are normalized such that each violin has the same maximum width.

Supplementary Information 1.2 Multiple Comparisons Plots

Supplementary Information 1.2.1 Biogen

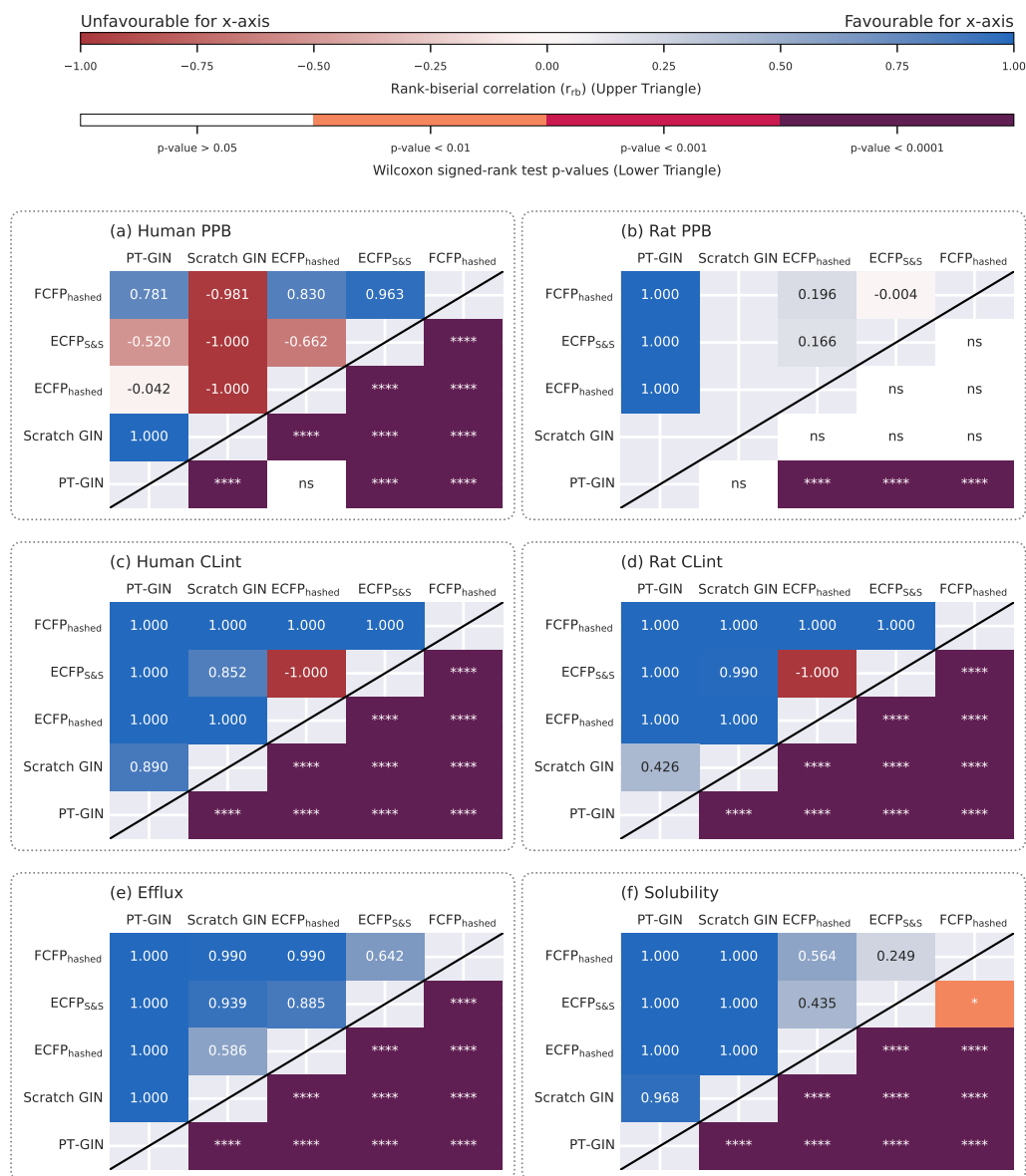


Figure 2: Rank-biserial coefficient (r_b) effect sizes (upper triangle) and Wilcoxon signed-rank test p -values (lower triangle) of the Pearson correlation ($\uparrow \rho$) between methods on Biogen datasets. Tasks are (a) Human Plasma Protein Binding (PPB), (b) Rat PPB, (c) Human Intrinsic Clearance (CLint), (d) Rat CLint, (e) Efflux, (f) Solubility. Featurisation methods shown are GINs trained from scratch (Scratch GIN), ECFP-pretrained GINs (PT-GIN), hashed Extended-Connectivity Fingerprints (ECFP_{hashed}), hashed Functional-Connectivity Fingerprints (FCFP_{hashed}), and ECFPs folded via Sort & Slice (ECFP_{S&S}). For r_b effect sizes (upper triangle): blue indicates the method on the x -axis has a higher ρ than the method on the y -axis; red indicates the opposite. For Wilcoxon signed-rank test p -values (lower triangle): white indicates no significant difference and darker indicates a smaller p -value ($n = 199$, $\alpha = 0.05$).

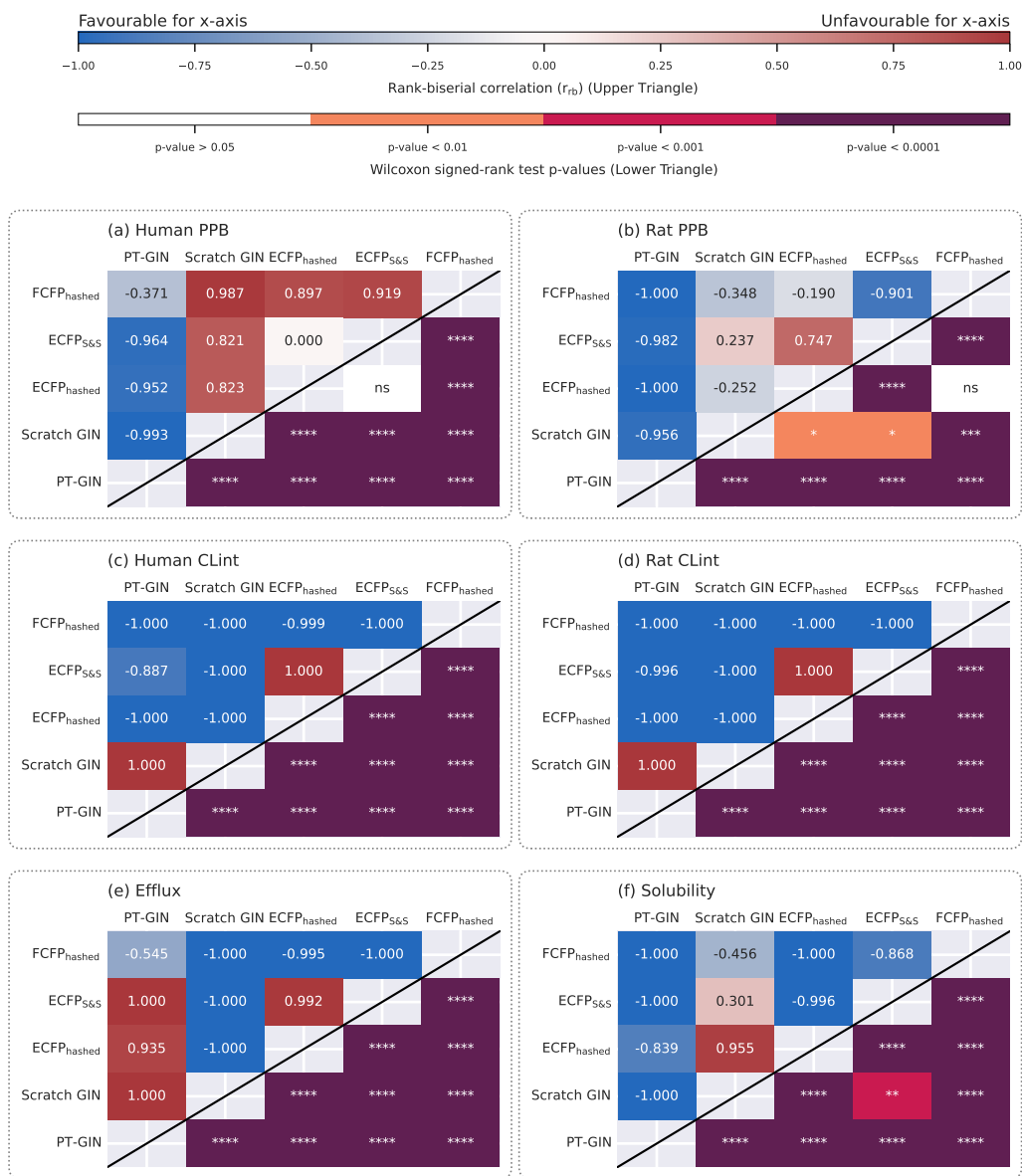


Figure 3: Rank-biserial coefficient (r_b) effect sizes (upper triangle) and Wilcoxon signed-rank test p -values (lower triangle) of the mean absolute percentage error (\downarrow MAPE(%)) between methods on Biogen datasets. Tasks are (a) Human Plasma Protein Binding (PPB), (b) Rat PPB, (c) Human Intrinsic Clearance (CLint), (d) Rat CLint, (e) Efflux, (f) Solubility. Featurisation methods shown are GINs trained from scratch (Scratch GIN), ECFP-pretrained GINs (PT-GIN), hashed Extended-Connectivity Fingerprints (ECFP_{hashed}), hashed Functional-Connectivity Fingerprints (FCFP_{hashed}), and ECFPs folded via Sort & Slice (ECFP_{S&S}). For r_b effect sizes (upper triangle): blue indicates the method on the x -axis has a higher MAPE than the method on the y -axis; red indicates the opposite. For Wilcoxon signed-rank test p -values (lower triangle): white indicates no significant difference and darker indicates a smaller p -value ($n = 199$, $\alpha = 0.05$).

Supplementary Information 1.2.2 Biogen Tanimoto Similarity Filter

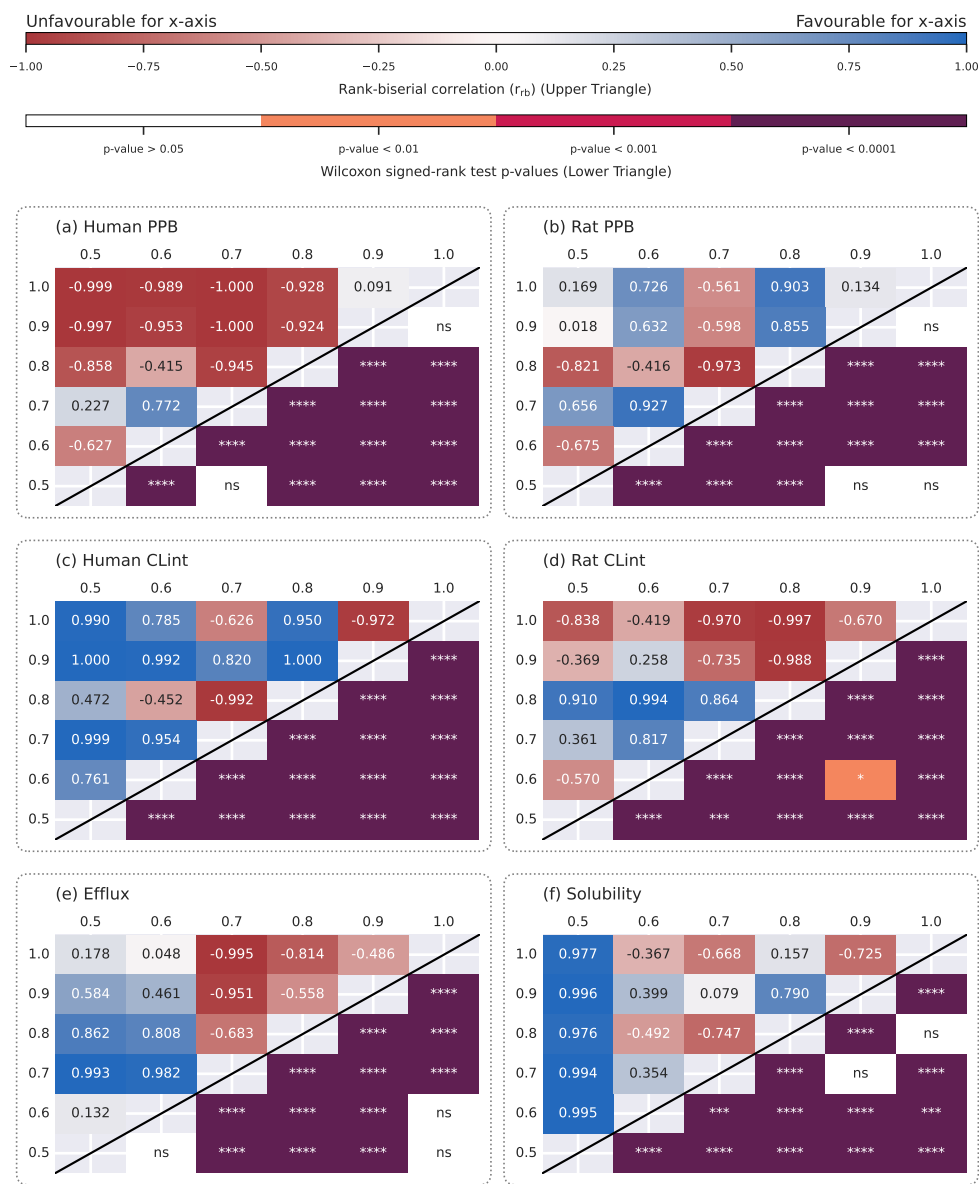


Figure 4: Rank-biserial coefficient (r_{rb}) effect sizes (upper triangle) and Wilcoxon signed-rank test p -values (lower triangle) of the Pearson correlation ($\uparrow \rho$) of PT-GIN models pre-trained on Tanimoto filtered QMugs subsets. Tasks are (a) Human Plasma Protein Binding (PPB), (b) Rat PPB, (c) Human Intrinsic Clearance (CLint), (d) Rat CLint, (e) Efflux, (f) Solubility. Featurisation methods shown are GINs pre-trained (PT-GIN) to predict ECFP₄₂₀₄₈ on QMugs with a Tanimoto filter of 0.5, 0.6, 0.7, 0.8, 0.9, and 1.0. All filter subsets were equal in size. For r_{rb} effect sizes (upper triangle): blue indicates the method on the x -axis has a higher ρ than the method on the y -axis; red indicates the opposite. For Wilcoxon signed-rank test p -values (lower triangle): white indicates no significant difference and darker indicates a smaller p -value ($n = 199$, $\alpha = 0.05$).

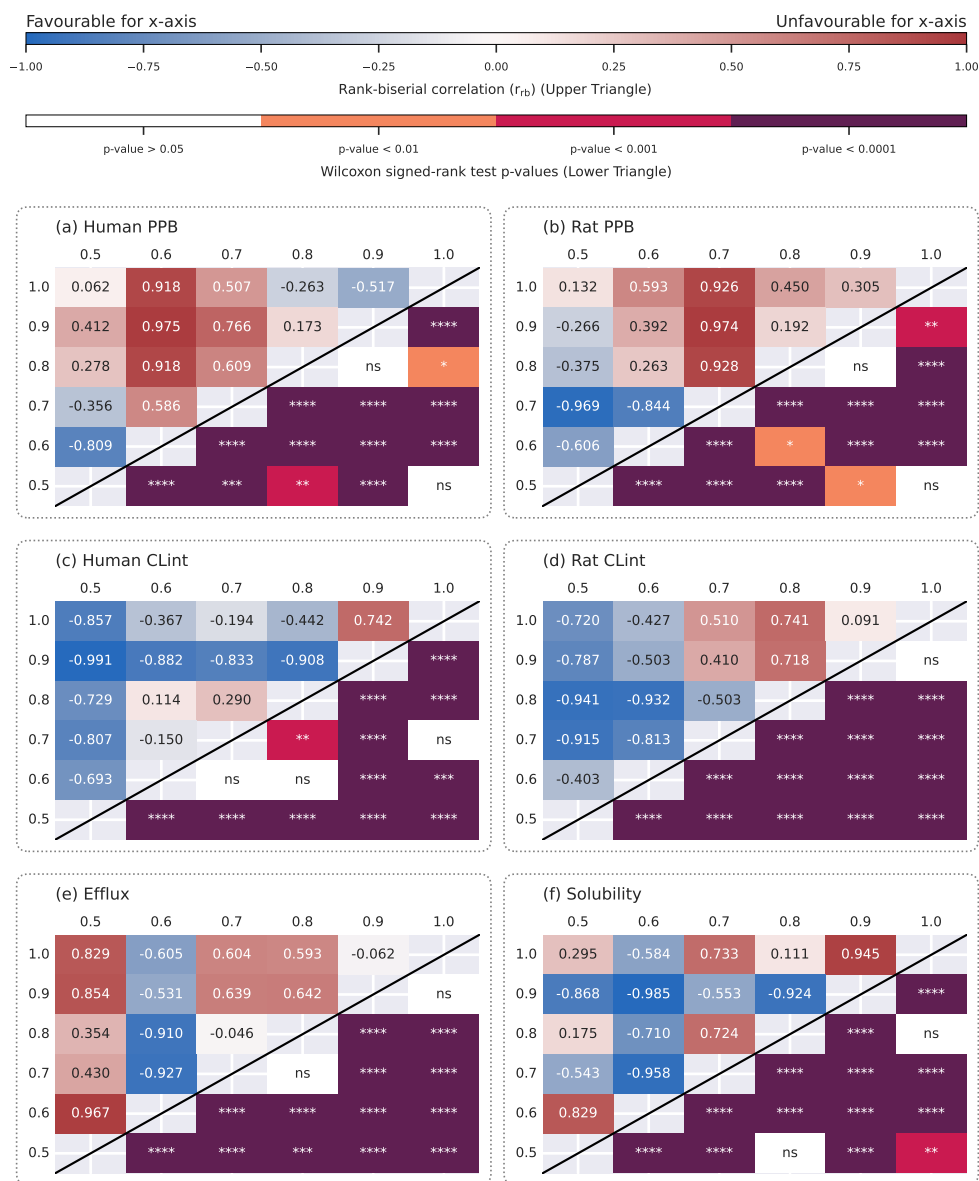


Figure 5: Rank-biserial coefficient ($r_{r,b}$) effect sizes (upper triangle) and Wilcoxon signed-rank test p -values (lower triangle) of the mean absolute percentage error (\downarrow MAPE(%)) of PT-GIN models pre-trained on Tanimoto filtered QMugs subsets. Tasks are (a) Human Plasma Protein Binding (PPB), (b) Rat PPB, (c) Human Intrinsic Clearance (CLint), (d) Rat CLint, (e) Efflux, (f) Solubility. Featurisation methods shown are GINs pre-trained (PT-GIN) to predict ECFP₄₂₀₄₈ on QMugs with a Tanimoto filter of 0.5, 0.6, 0.7, 0.8, 0.9, and 1.0. All filter subsets were equal in size. For $r_{r,b}$ effect sizes (upper triangle): blue indicates the method on the x -axis has a higher MAPE than the method on the y -axis; red indicates the opposite. For Wilcoxon signed-rank test p -values (lower triangle): white indicates no significant difference and darker indicates a smaller p -value ($n = 199$, $\alpha = 0.05$).

Supplementary Information 1.2.3 ChEMBL

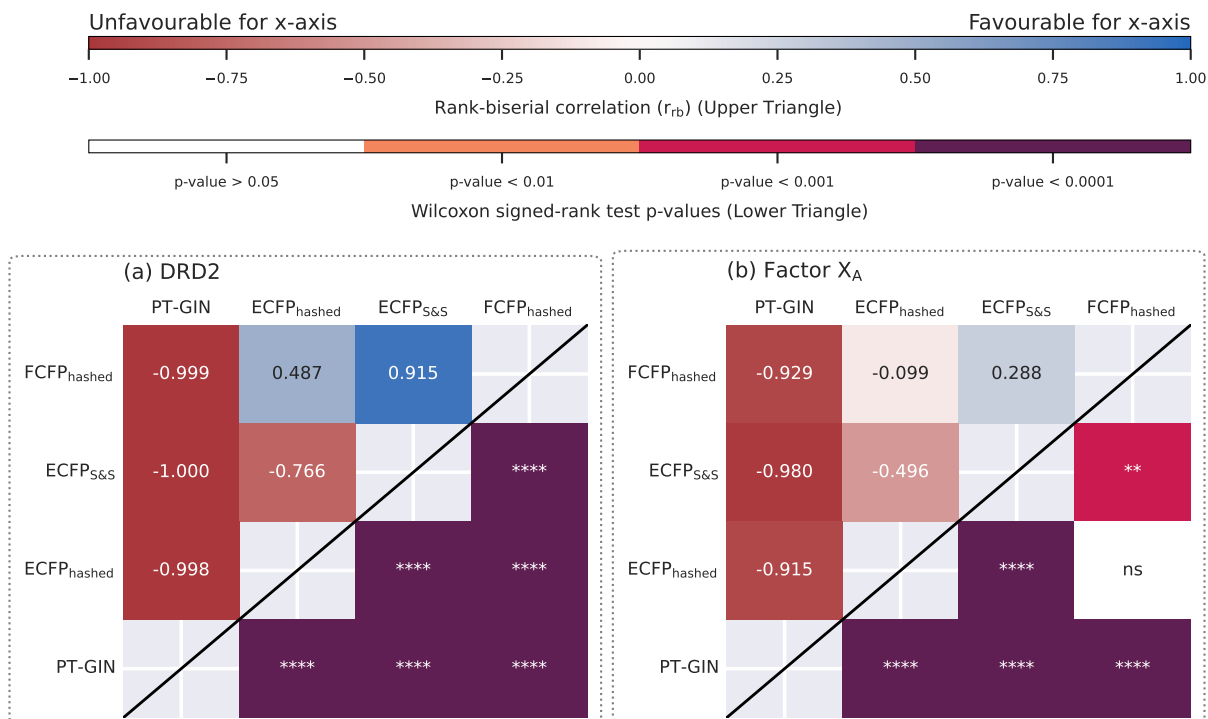


Figure 6: Rank-biserial coefficient (r_{rb}) effect sizes (upper triangle) and Wilcoxon signed-rank test p -values (lower triangle) of the coefficient of determination ($\uparrow R^2$) between methods on ChEMBL datasets. Tasks are (a) DRD2, (b) Factor X_A binding affinity prediction. Featurisation methods shown are ECFP-pretrained GINs (PT-GIN), hashed Extended-Connectivity Fingerprints (ECFP_{hashed}), hashed Functional-Connectivity Fingerprints (FCFP_{hashed}), and ECFPs folded via Sort & Slice (ECFP_{S&S}). For r_{rb} effect sizes (upper triangle): blue indicates the method on the x -axis has a higher R^2 than the method on the y -axis; red indicates the opposite. For Wilcoxon signed-rank test p -values (lower triangle): white indicates no significant difference and darker indicates a smaller p -value ($n = 199$, $\alpha = 0.05$).

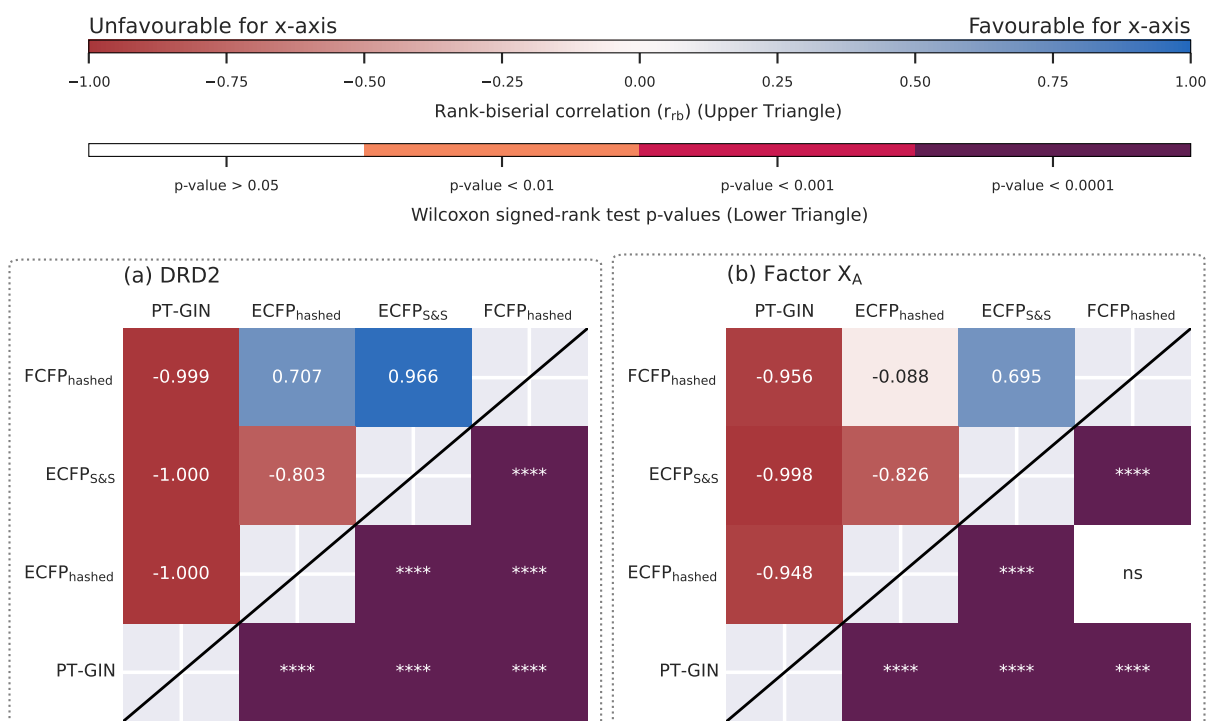


Figure 7: Rank-biserial coefficient (r_{rb}) effect sizes (upper triangle) and Wilcoxon signed-rank test p -values (lower triangle) of the Pearson correlation ($\uparrow \rho$) between methods on ChEMBL datasets. Tasks are (a) DRD2, (b) Factor X_A binding affinity prediction. Featurisation methods shown are ECFP-pretrained GINs (PT-GIN), hashed Extended-Connectivity Fingerprints (ECFP_{hashed}), hashed Functional-Connectivity Fingerprints (FCFP_{hashed}), and ECFPs folded via Sort & Slice (ECFP_{S&S}). For r_{rb} effect sizes (upper triangle): blue indicates the method on the x -axis has a higher ρ than the method on the y -axis; red indicates the opposite. For Wilcoxon signed-rank test p -values (lower triangle): white indicates no significant difference and darker indicates a smaller p -value ($n = 199$, $\alpha = 0.05$).

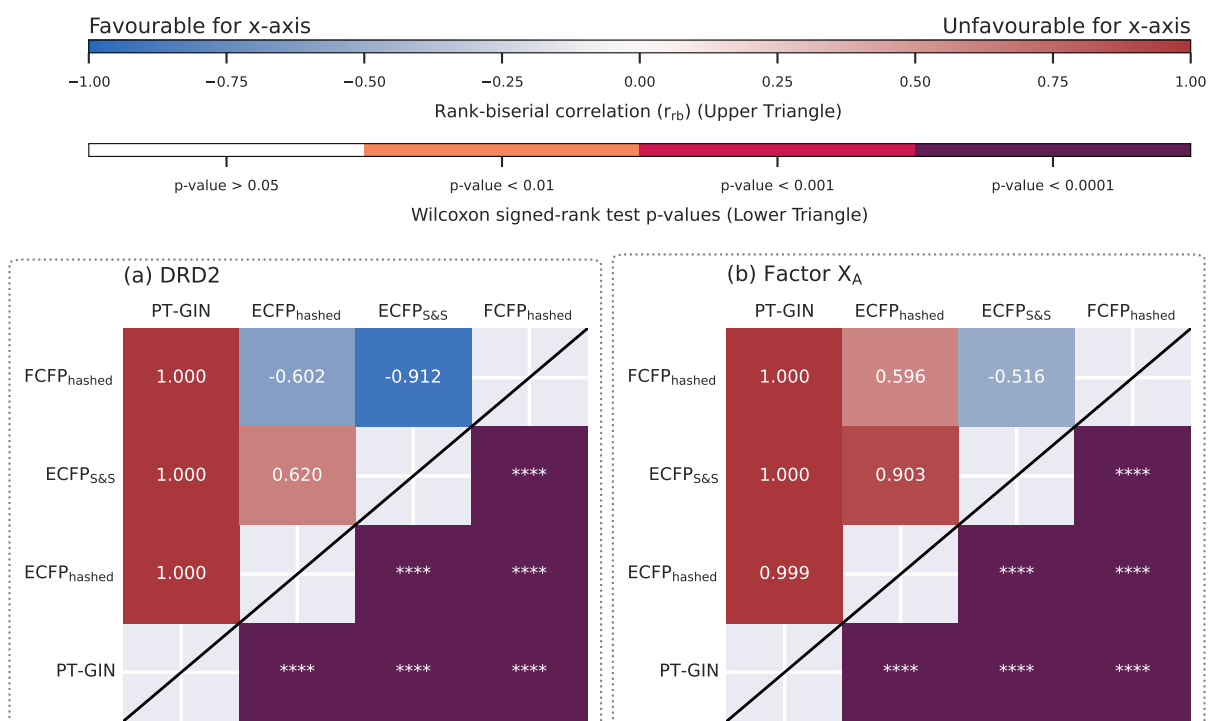


Figure 8: Rank-biserial coefficient (r_{rb}) effect sizes (upper triangle) and Wilcoxon signed-rank test p -values (lower triangle) of the mean absolute percentage error (\downarrow MAPE(%)) between methods on ChEMBL datasets. Tasks are (a) DRD2, (b) Factor X_A binding affinity prediction. Featurisation methods shown are ECFP-pretrained GINs (PT-GIN), hashed Extended-Connectivity Fingerprints (ECFP_{hashed}), hashed Functional-Connectivity Fingerprints (FCFP_{hashed}), and ECFPs folded via Sort & Slice (ECFP_{S&S}). For r_{rb} effect sizes (upper triangle): blue indicates the method on the x -axis has a higher MAPE than the method on the y -axis; red indicates the opposite. For Wilcoxon signed-rank test p -values (lower triangle): white indicates no significant difference and darker indicates a smaller p -value ($n = 199$, $\alpha = 0.05$).

Supplementary Information 1.2.4 MoleculeNet Regression

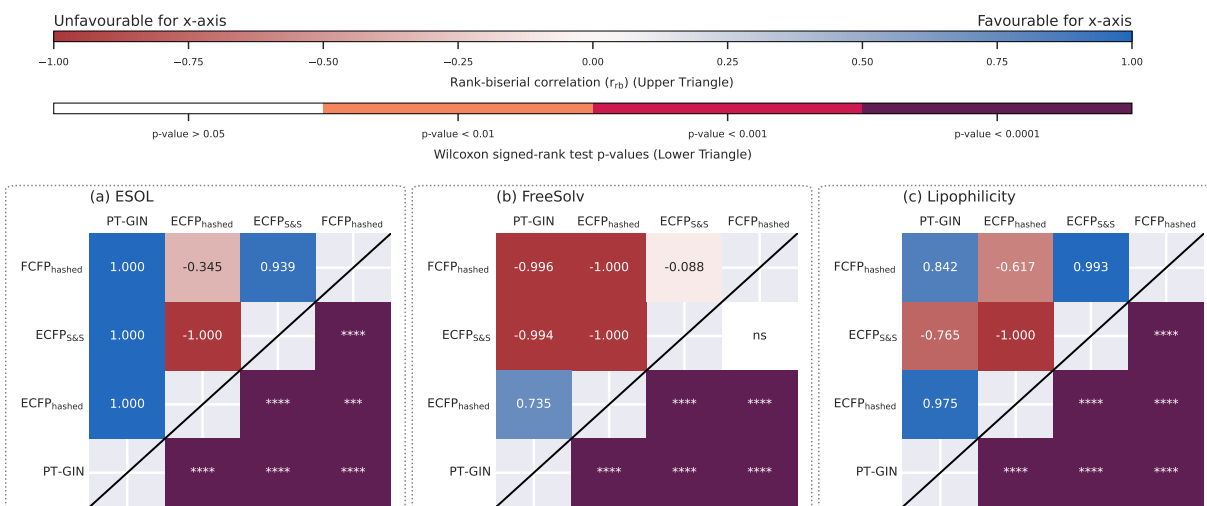


Figure 9: Rank-biserial coefficient ($r_{r,b}$) effect sizes (upper triangle) and Wilcoxon signed-rank test p -values (lower triangle) of the Pearson correlation ($\uparrow \rho$) between methods on MoleculeNet regression datasets. Datasets shown are (a) ESOL, (b) FreeSolv, and (c) Lipophilicity. Featurisation methods shown are ECFP-pretrained GINs (PT-GIN), hashed Extended-Connectivity Fingerprints (ECFP_{hashed}), hashed Functional-Connectivity Fingerprints (FCFP_{hashed}), and ECFPs folded via Sort & Slice (ECFP_{S&S}). For $r_{r,b}$ effect sizes (upper triangle): blue indicates the method on the x -axis has a higher ρ than the method on the y -axis; red indicates the opposite. For Wilcoxon signed-rank test p -values (lower triangle): white indicates no significant difference and darker indicates a smaller p -value ($n = 199$, $\alpha = 0.05$).

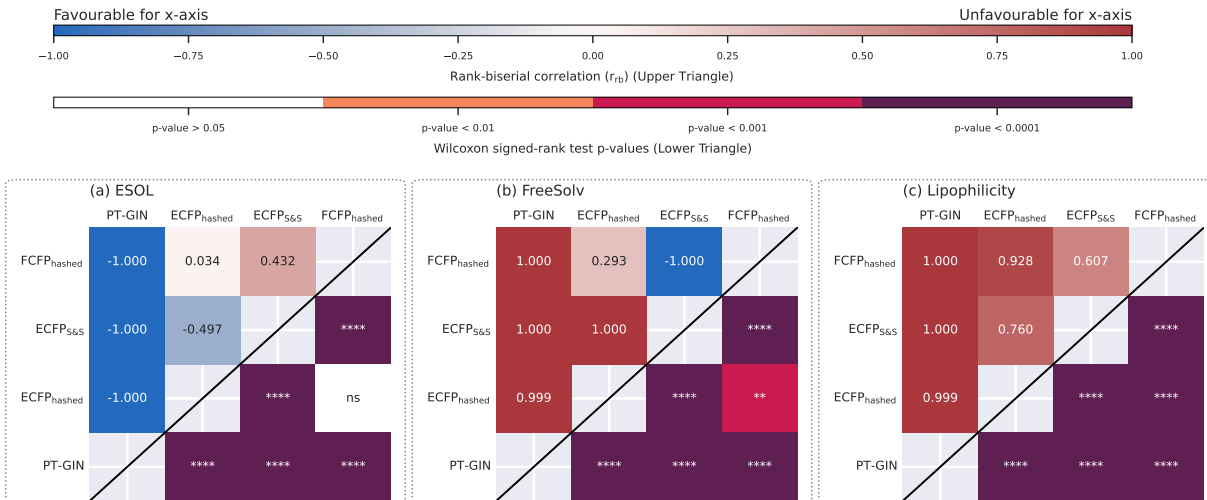


Figure 10: Rank-biserial coefficient ($r_{r,b}$) effect sizes (upper triangle) and Wilcoxon signed-rank test p -values (lower triangle) of the mean absolute percentage error ($\downarrow \text{MAPE}(\%)$) between methods on MoleculeNet regression datasets. Datasets shown are (a) ESOL, (b) FreeSolv, and (c) Lipophilicity. Featurisation methods shown are ECFP-pretrained GINs (PT-GIN), hashed Extended-Connectivity Fingerprints (ECFP_{hashed}), hashed Functional-Connectivity Fingerprints (FCFP_{hashed}), and ECFPs folded via Sort & Slice (ECFP_{S&S}). For $r_{r,b}$ effect sizes (upper triangle): blue indicates the method on the x -axis has a higher MAPE than the method on the y -axis; red indicates the opposite. For Wilcoxon signed-rank test p -values (lower triangle): white indicates no significant difference and darker indicates a smaller p -value ($n = 199$, $\alpha = 0.05$).

Supplementary Information 1.2.5 MUV

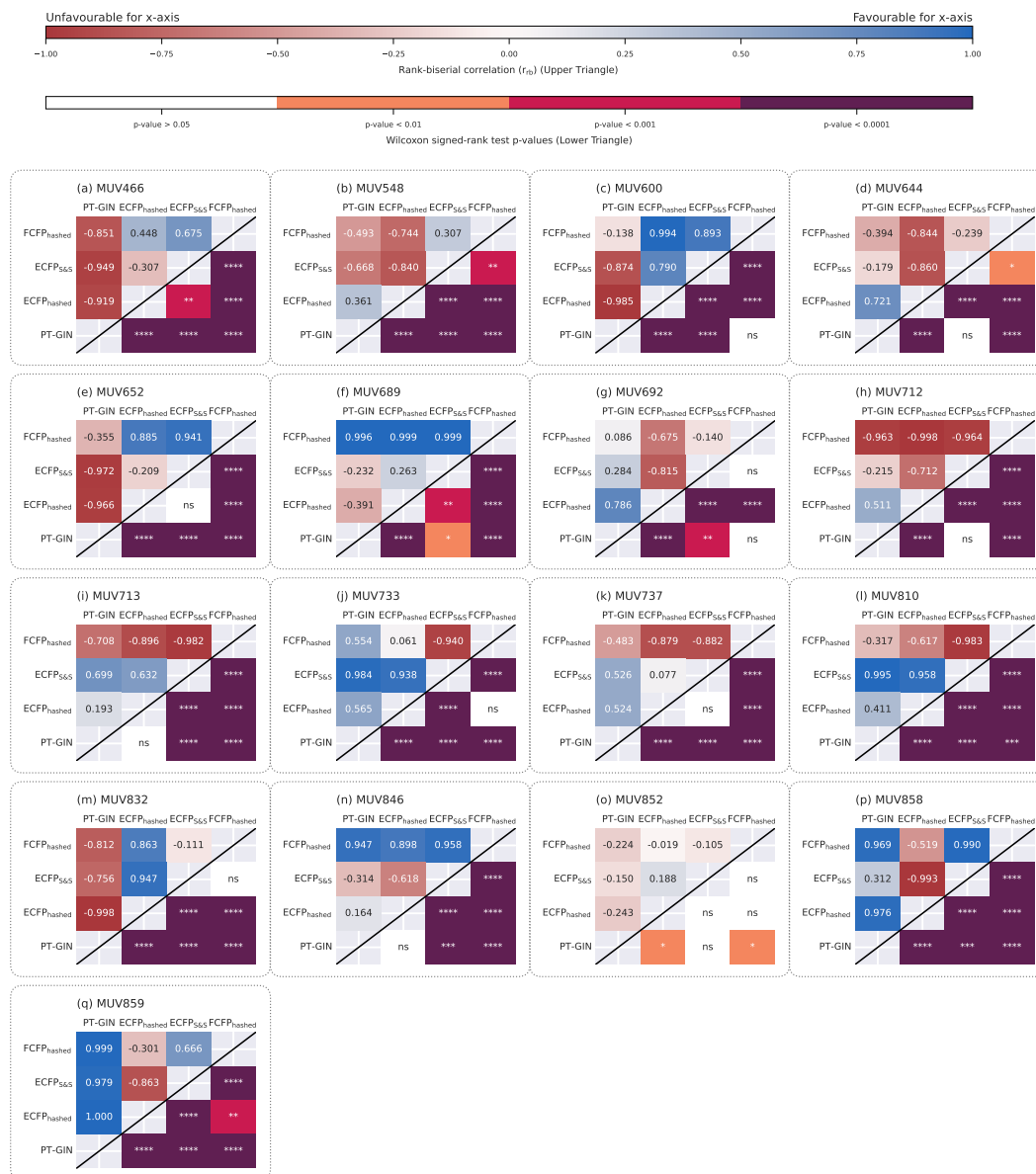


Figure 11: Rank-biserial coefficient (r_b) effect sizes (upper triangle) and Wilcoxon signed-rank test p -values (lower triangle) of the Area Under the Receiver Operating Characteristic (\uparrow AUROC) between methods on MUV virtual screening tasks. Tasks are (a) MUV466, (b) MUV548, (c) MUV600, (d) MUV644, (e) MUV652, (f) MUV689, (g) MUV692, (h) MUV712, (i) MUV713, (j) MUV733, (k) MUV737, (l) MUV810, (m) MUV832, (n) MUV846, (o) MUV852, (p) MUV858, (q) MUV859. Featurisation methods shown are ECFP-pretrained GINs (PT-GIN), hashed Extended-Connectivity Fingerprints (ECFP_{hashed}), hashed Functional-Connectivity Fingerprints (FCFP_{hashed}), and ECFPs folded via Sort & Slice (ECFP_{S&S}). For r_b effect sizes (upper triangle): blue indicates the method on the x -axis has a higher AUROC than the method on the y -axis; red indicates the opposite. For Wilcoxon signed-rank test p -values (lower triangle): white indicates no significant difference and darker indicates a smaller p -value ($n = 199$, $\alpha = 0.05$).

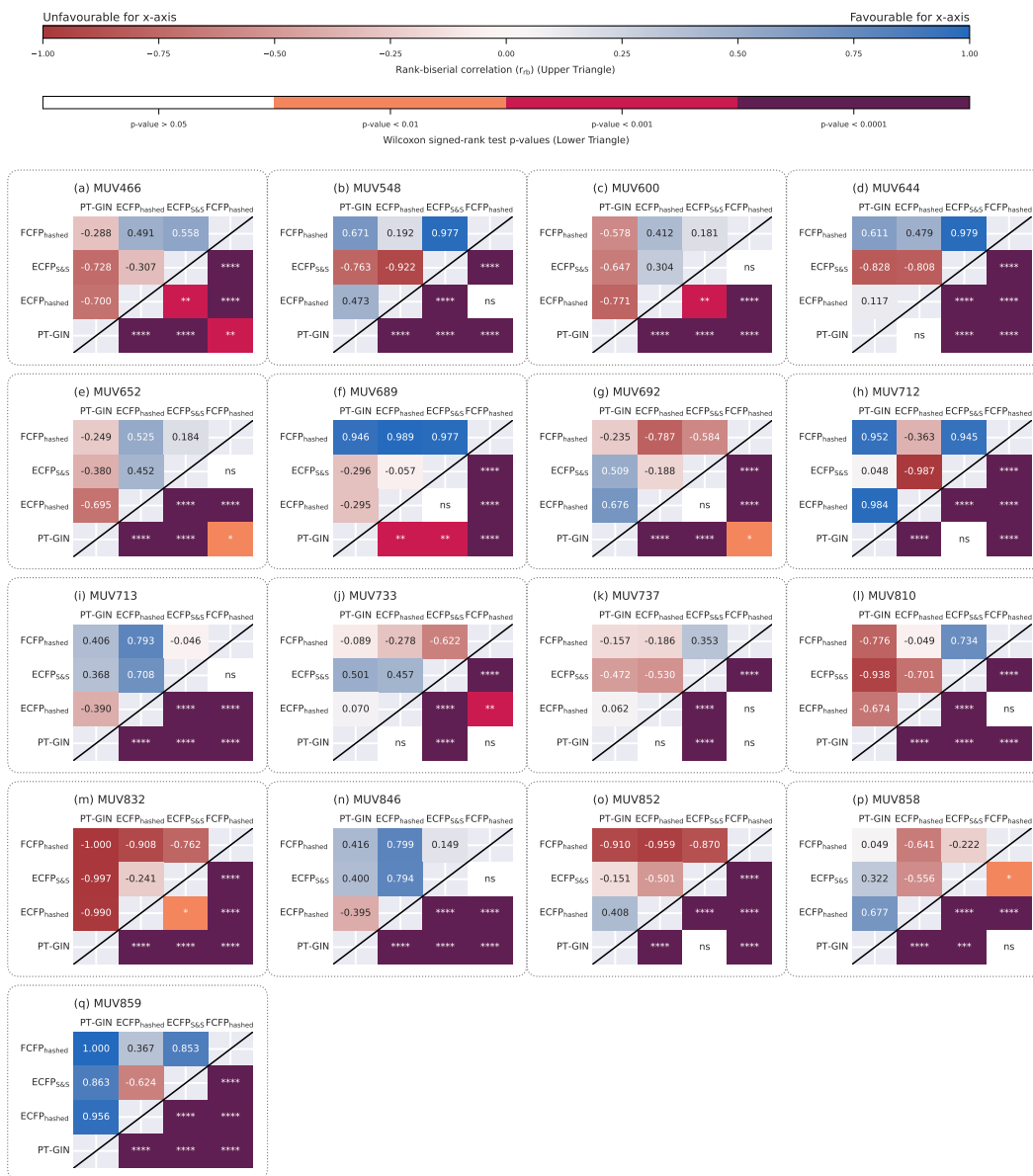


Figure 12: Rank-biserial coefficient (r_b) effect sizes (upper triangle) and Wilcoxon signed-rank test p -values (lower triangle) of the Area Under the Precision-Recall Curve (\uparrow AUCPR) between methods on MUV virtual screening tasks. Tasks are (a) MUV466, (b) MUV548, (c) MUV600, (d) MUV644, (e) MUV652, (f) MUV689, (g) MUV692, (h) MUV712, (i) MUV713, (j) MUV733, (k) MUV737, (l) MUV810, (m) MUV832, (n) MUV846, (o) MUV852, (p) MUV858, (q) MUV859. Featurisation methods shown are ECFP-pretrained GINs (PT-GIN), hashed Extended-Connectivity Fingerprints (ECFP_{hashed}), hashed Functional-Connectivity Fingerprints (FCFP_{hashed}), and ECFPs folded via Sort & Slice (ECFP_{S&S}). For r_b effect sizes (upper triangle): blue indicates the method on the x -axis has a higher AUCPR than the method on the y -axis; red indicates the opposite. For Wilcoxon signed-rank test p -values (lower triangle): white indicates no significant difference and darker indicates a smaller p -value ($n = 199$, $\alpha = 0.05$).

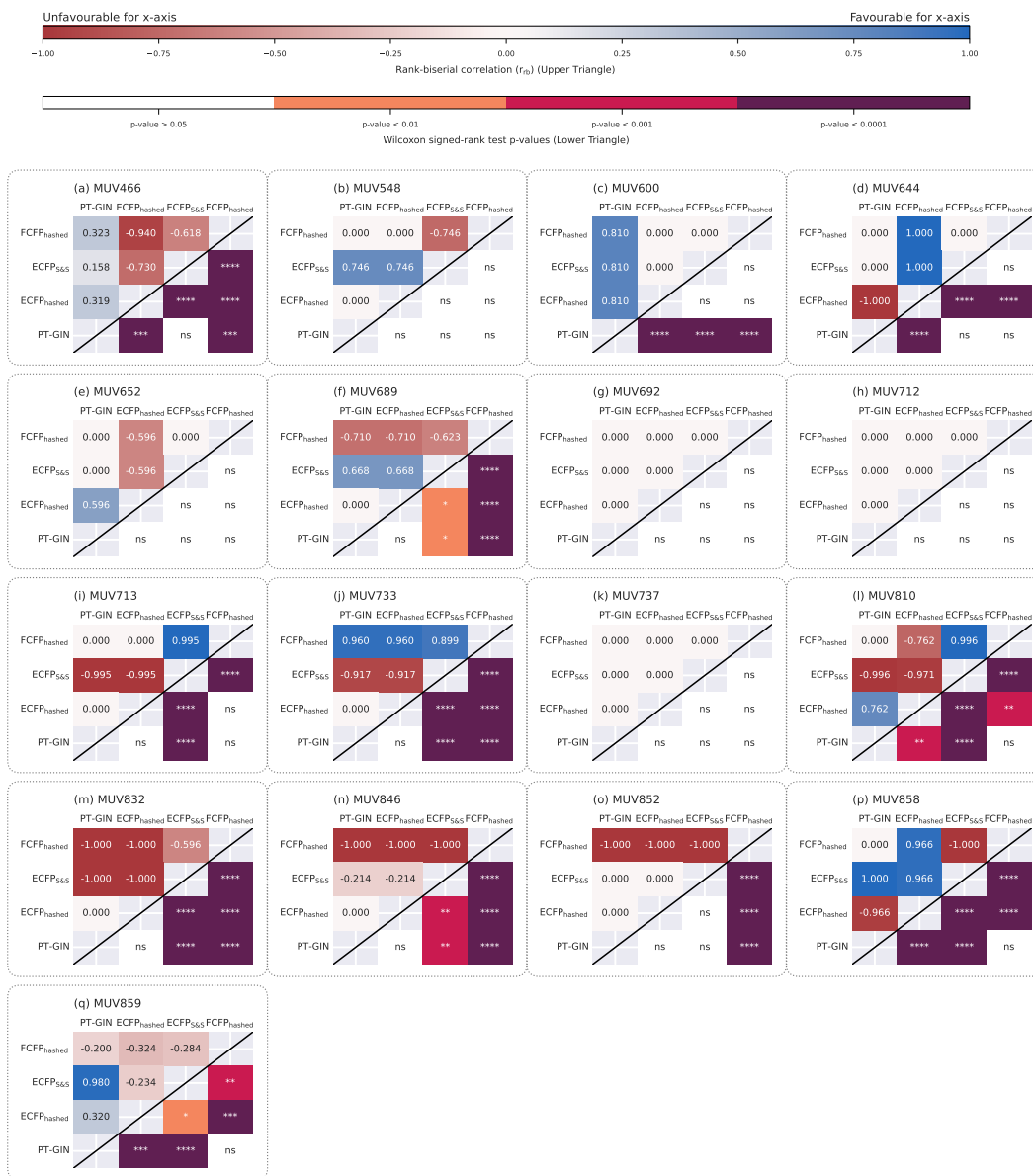


Figure 13: Rank-biserial coefficient (r_b) effect sizes (upper triangle) and Wilcoxon signed-rank test p -values (lower triangle) of the Matthews correlation coefficient (\uparrow MCC) between methods on MUV virtual screening tasks. Tasks are (a) MUV466, (b) MUV548, (c) MUV600, (d) MUV644, (e) MUV652, (f) MUV689, (g) MUV692, (h) MUV712, (i) MUV713, (j) MUV733, (k) MUV737, (l) MUV810, (m) MUV832, (n) MUV846, (o) MUV852, (p) MUV858, (q) MUV859. Featurisation methods shown are ECFP-pretrained GINs (PT-GIN), hashed Extended-Connectivity Fingerprints (ECFP_{hashed}), hashed Functional-Connectivity Fingerprints (FCFP_{hashed}), and ECFPs folded via Sort & Slice (ECFP_{S&S}). For r_b effect sizes (upper triangle): blue indicates the method on the x -axis has a higher MCC than the method on the y -axis; red indicates the opposite. For Wilcoxon signed-rank test p -values (lower triangle): white indicates no significant difference and darker indicates a smaller p -value ($n = 199$, $\alpha = 0.05$).

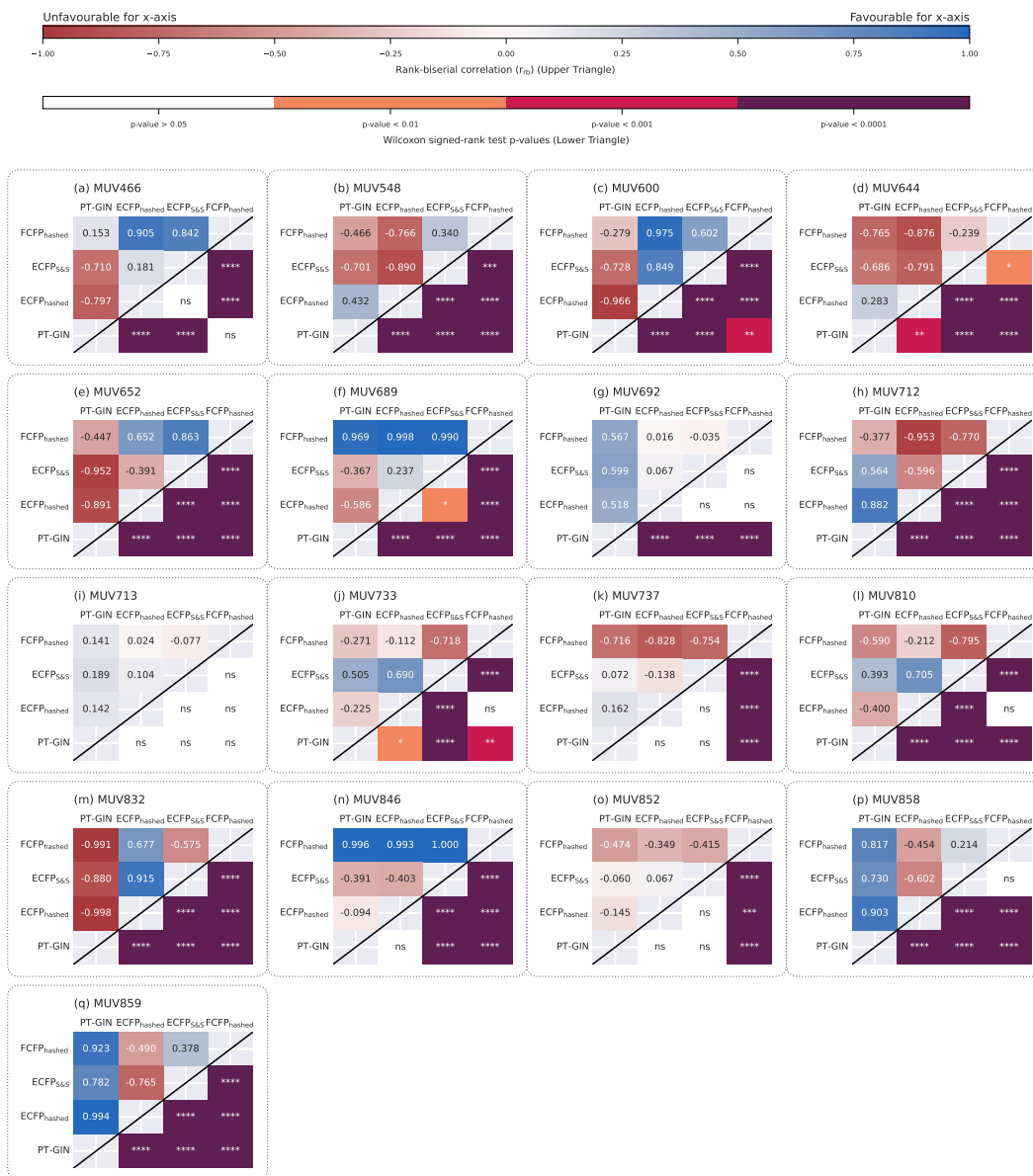


Figure 14: Rank-biserial coefficient (r_{rb}) effect sizes (upper triangle) and Wilcoxon signed-rank test p -values (lower triangle) of the Enrichment Factor at 10% ($\uparrow EF_{10\%}$) between methods on MUV virtual screening tasks. Tasks are (a) MUV466, (b) MUV548, (c) MUV600, (d) MUV644, (e) MUV652, (f) MUV689, (g) MUV692, (h) MUV712, (i) MUV713, (j) MUV733, (k) MUV737, (l) MUV810, (m) MUV832, (n) MUV846, (o) MUV852, (p) MUV858, (q) MUV859. Featurisation methods shown are ECFP-pretrained GINs (PT-GIN), hashed Extended-Connectivity Fingerprints (ECFP_{hashed}), hashed Functional-Connectivity Fingerprints (FCFP_{hashed}), and ECFPs folded via Sort & Slice (ECFP_{S&S}). For r_{rb} effect sizes (upper triangle): blue indicates the method on the x -axis has a higher $EF_{10\%}$ than the method on the y -axis; red indicates the opposite. For Wilcoxon signed-rank test p -values (lower triangle): white indicates no significant difference and darker indicates a smaller p -value ($n = 199$, $\alpha = 0.05$).

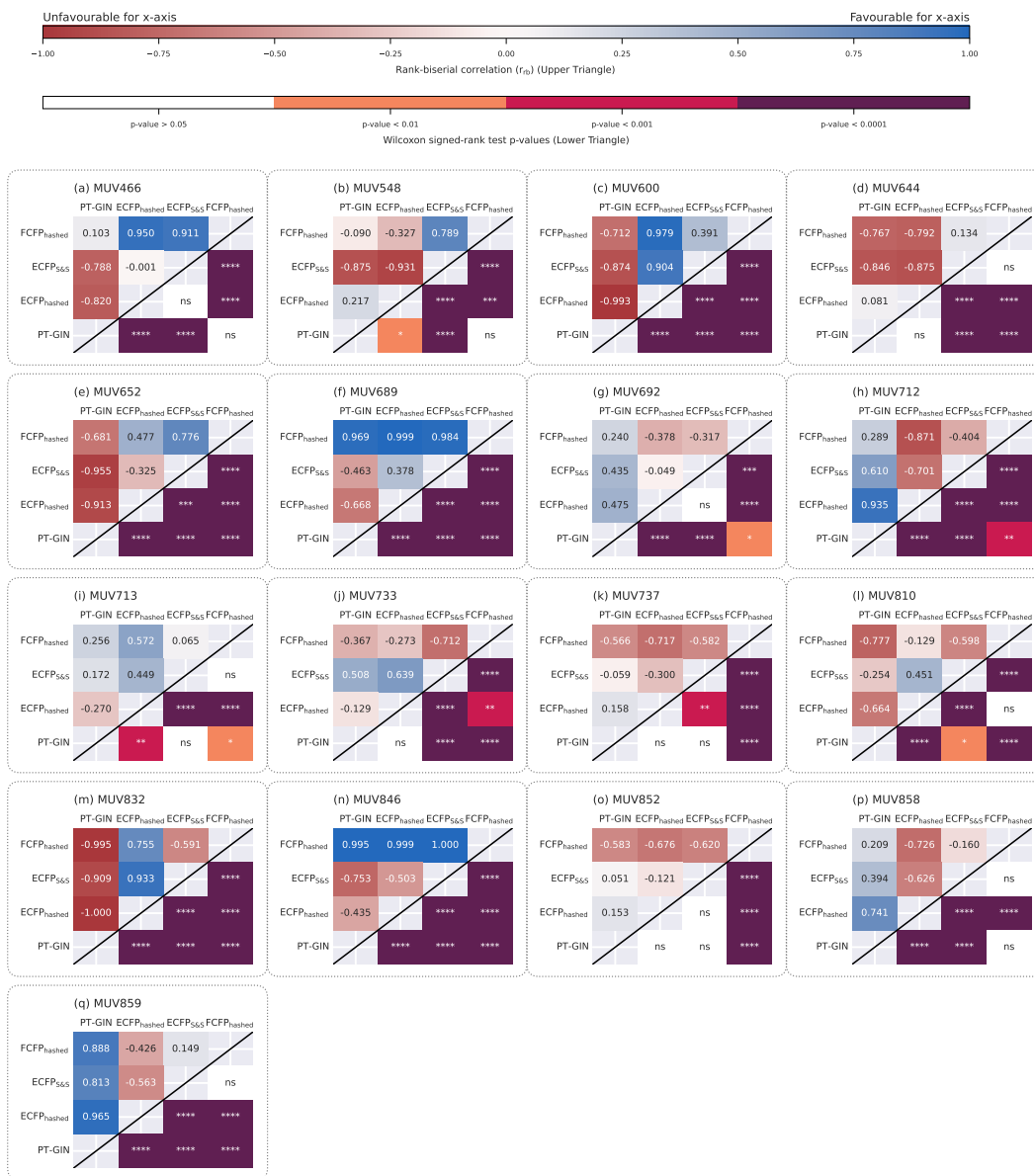


Figure 15: Rank-biserial coefficient (r_b) effect sizes (upper triangle) and Wilcoxon signed-rank test p -values (lower triangle) of the Enrichment Factor at 5% ($\uparrow EF_{5\%}$) between methods on MUV virtual screening tasks. Tasks are (a) MUV466, (b) MUV548, (c) MUV600, (d) MUV644, (e) MUV652, (f) MUV689, (g) MUV692, (h) MUV712, (i) MUV713, (j) MUV733, (k) MUV737, (l) MUV810, (m) MUV832, (n) MUV846, (o) MUV852, (p) MUV858, (q) MUV859. Featurisation methods shown are ECFP-pretrained GINs (PT-GIN), hashed Extended-Connectivity Fingerprints (ECFP_{hashed}), hashed Functional-Connectivity Fingerprints (FCFP_{hashed}), and ECFPs folded via Sort & Slice (ECFP_{S&S}). For r_b effect sizes (upper triangle): blue indicates the method on the x -axis has a higher $EF_{5\%}$ than the method on the y -axis; red indicates the opposite. For Wilcoxon signed-rank test p -values (lower triangle): white indicates no significant difference and darker indicates a smaller p -value ($n = 199$, $\alpha = 0.05$).

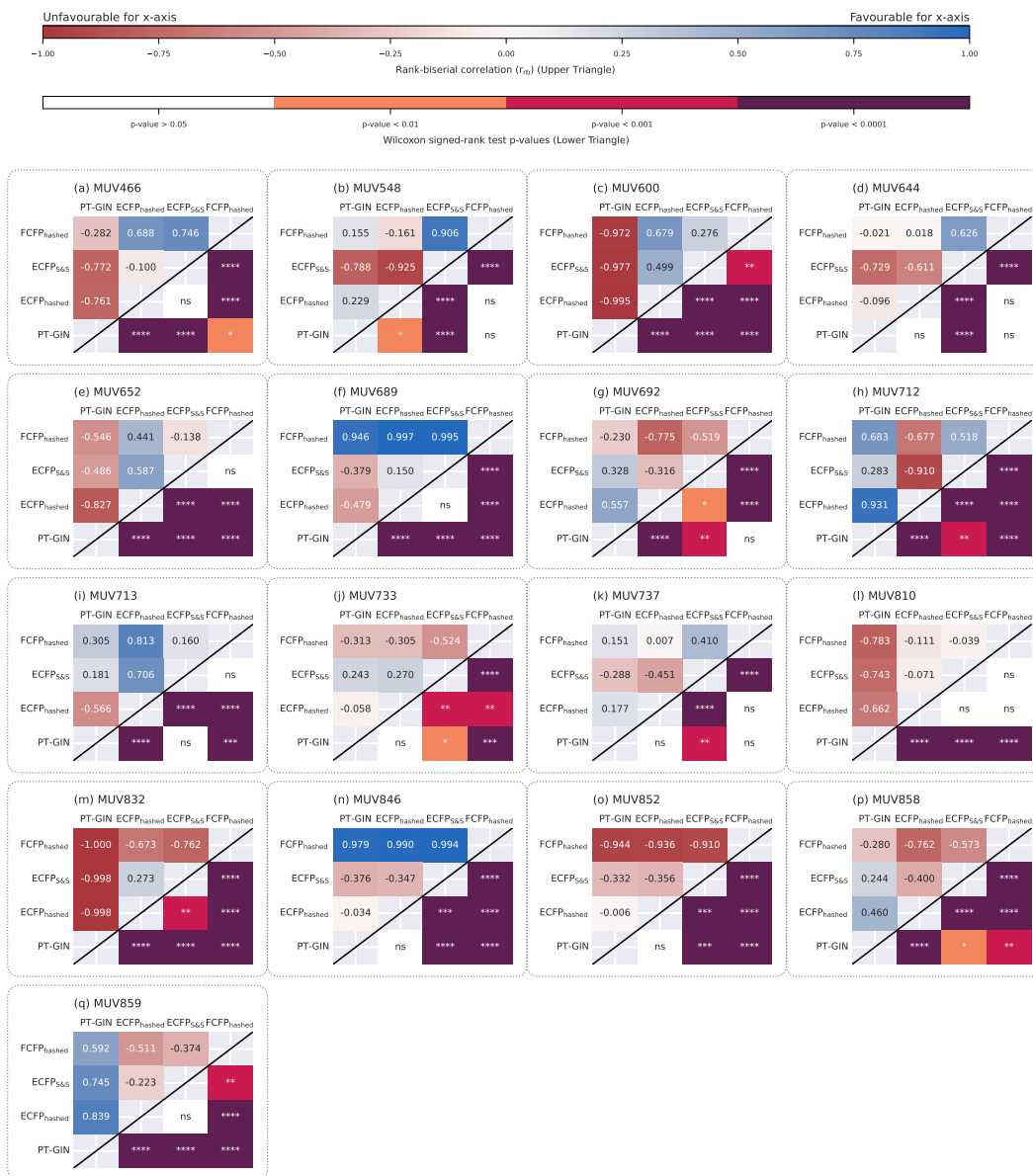


Figure 16: Rank-biserial coefficient (r_{rb}) effect sizes (upper triangle) and Wilcoxon signed-rank test p -values (lower triangle) of the Enrichment Factor at 1% ($\uparrow EF_{1\%}$) between methods on MUV virtual screening tasks. Tasks are (a) MUV466, (b) MUV548, (c) MUV600, (d) MUV644, (e) MUV652, (f) MUV689, (g) MUV692, (h) MUV712, (i) MUV713, (j) MUV733, (k) MUV737, (l) MUV810, (m) MUV832, (n) MUV846, (o) MUV852, (p) MUV858, (q) MUV859. Featurisation methods shown are ECFP-pretrained GINs (PT-GIN), hashed Extended-Connectivity Fingerprints (ECFP_{hashed}), hashed Functional-Connectivity Fingerprints (FCFP_{hashed}), and ECFPs folded via Sort & Slice (ECFP_{S&S}). For r_{rb} effect sizes (upper triangle): blue indicates the method on the x -axis has a higher $EF_{1\%}$ than the method on the y -axis; red indicates the opposite. For Wilcoxon signed-rank test p -values (lower triangle): white indicates no significant difference and darker indicates a smaller p -value ($n = 199$, $\alpha = 0.05$).

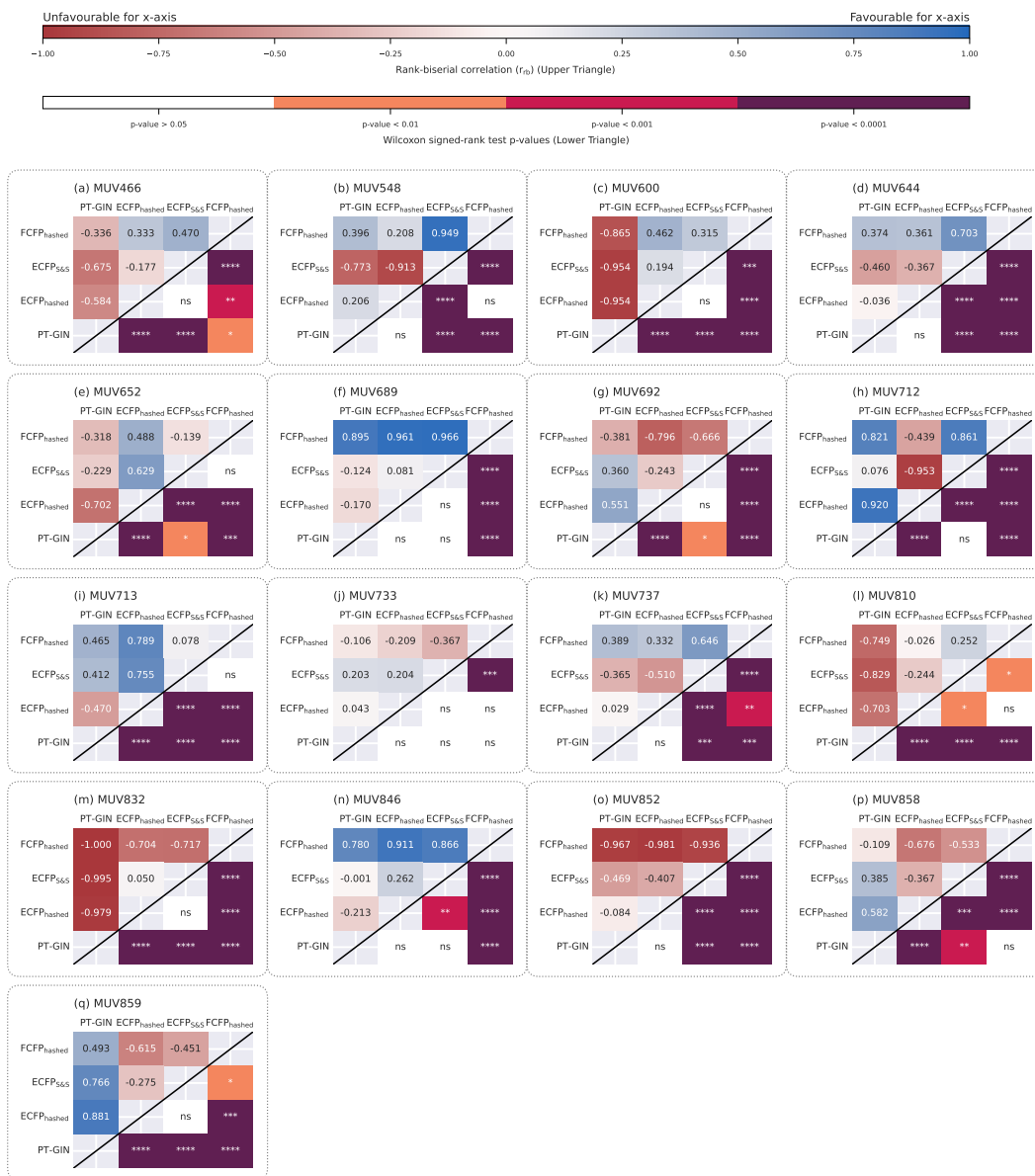


Figure 17: Rank-biserial coefficient (r_{rb}) effect sizes (upper triangle) and Wilcoxon signed-rank test p -values (lower triangle) of the Enrichment Factor at 0.5% ($\uparrow EF_{0.5\%}$) between methods on MUV virtual screening tasks. Tasks are (a) MUV466, (b) MUV548, (c) MUV600, (d) MUV644, (e) MUV652, (f) MUV689, (g) MUV692, (h) MUV712, (i) MUV713, (j) MUV733, (k) MUV737, (l) MUV810, (m) MUV832, (n) MUV846, (o) MUV852, (p) MUV858, (q) MUV859. Featurisation methods shown are ECFP-pretrained GINs (PT-GIN), hashed Extended-Connectivity Fingerprints (ECFP_{hashed}), hashed Functional-Connectivity Fingerprints (FCFP_{hashed}), and ECFPs folded via Sort & Slice (ECFP_{S&S}). For r_{rb} effect sizes (upper triangle): blue indicates the method on the x -axis has a higher $EF_{0.5\%}$ than the method on the y -axis; red indicates the opposite. For Wilcoxon signed-rank test p -values (lower triangle): white indicates no significant difference and darker indicates a smaller p -value ($n = 199$, $\alpha = 0.05$).

Supplementary Information 1.2.6 Tox21

Abbreviation	Label	PubChem Assay ID
NR AR	androgen receptor activation	743040
NR AR LBD	androgen receptor ligand binding domain activation	743053
NR AhR	aryl hydrocarbon receptor activation	743122
NR Aromatase	aromatase enzyme inhibition	743139
NR ER	estrogen receptor alpha activation	743079
NR ER LBD	estrogen receptor alpha ligand binding domain activation	743077
NR PPAR γ	peroxisome proliferator-activated receptor γ activation	743140
SR ARE	antioxidant responsive element signalling pathway activation	743219
SR ATAD5	ATPase family AAA domain containing 5 expression	720516
SR HSE	heat shock element signalling pathway activation	743228
SR MMP	mitochondrial membrane potential disruption	720637
SR p53	p53 signalling pathway activation	720552

Table 1: Tox21 toxicity screening tasks [1]. See <https://tripod.nih.gov/tox21/challenge/data.jsp>. NR = nuclear receptor signalling pathway, SR = stress response pathway. All twelve tasks correspond to quantitative high-throughput screening (qHTS) assay endpoints, where labels indicate whether a compound is active or inactive for a given biological pathway.

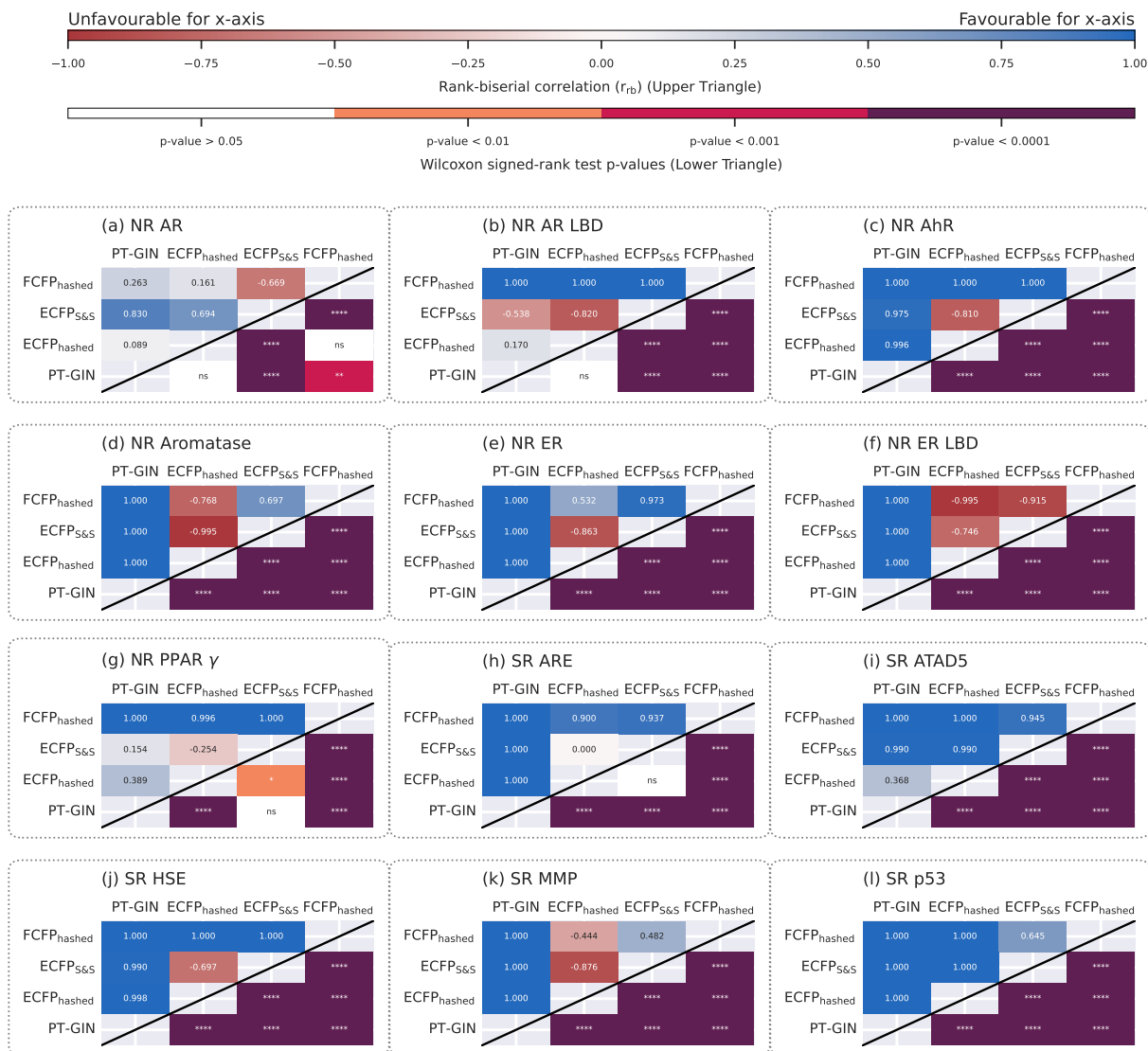


Figure 18: Rank-biserial coefficient (r_{rb}) effect sizes (upper triangle) and Wilcoxon signed-rank test p -values (lower triangle) of the Area Under the Receiver Operating Characteristic (\uparrow AUROC) between methods on Tox21 toxicity tasks. For task labels, see Table 1. Featurisation methods shown are ECFP-pretrained GINs (PT-GIN), hashed Extended-Connectivity Fingerprints (ECFP_{hashed}), hashed Functional-Connectivity Fingerprints (FCFP_{hashed}), and ECFPs folded via Sort & Slice (ECFP_{S&S}). For r_{rb} effect sizes (upper triangle): blue indicates the method on the x -axis has a higher AUROC than the method on the y -axis; red indicates the opposite. For Wilcoxon signed-rank test p -values (lower triangle): white indicates no significant difference and darker indicates a smaller p -value ($n = 199$, $\alpha = 0.05$).

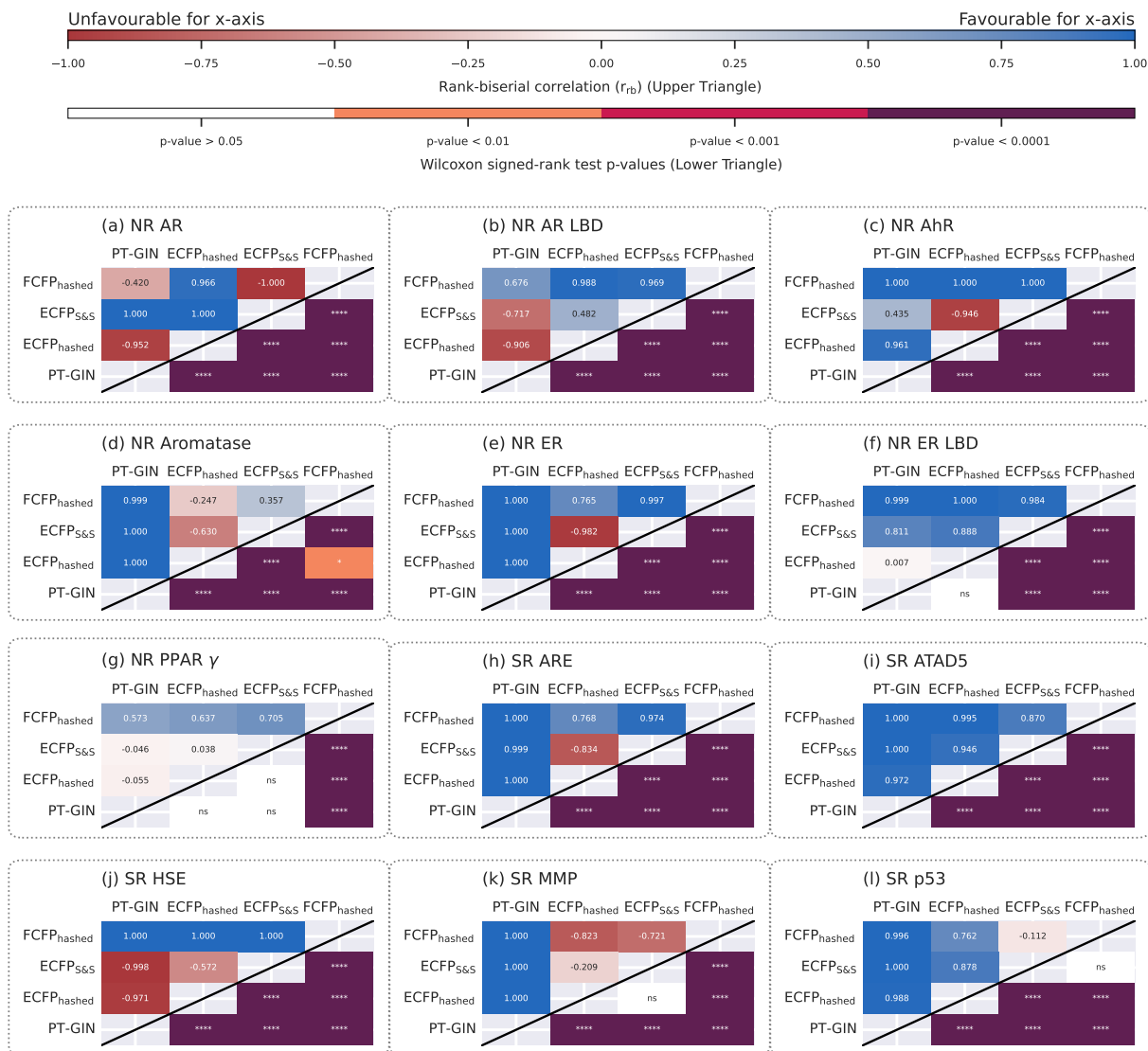


Figure 19: Rank-biserial coefficient (r_{rb}) effect sizes (upper triangle) and Wilcoxon signed-rank test p -values (lower triangle) of the Area Under the Precision-Recall Curve (\uparrow AUCPR) between methods on Tox21 toxicity tasks. For task labels, see Table 1. Featurisation methods shown are ECFP-pretrained GINs (PT-GIN), hashed Extended-Connectivity Fingerprints (ECFP_{hashed}), hashed Functional-Connectivity Fingerprints (FCFP_{hashed}), and ECFPs folded via Sort & Slice (ECFP_{S&S}). For r_{rb} effect sizes (upper triangle): blue indicates the method on the x -axis has a higher AUCPR than the method on the y -axis; red indicates the opposite. For Wilcoxon signed-rank test p -values (lower triangle): white indicates no significant difference and darker indicates a smaller p -value ($n = 199$, $\alpha = 0.05$).

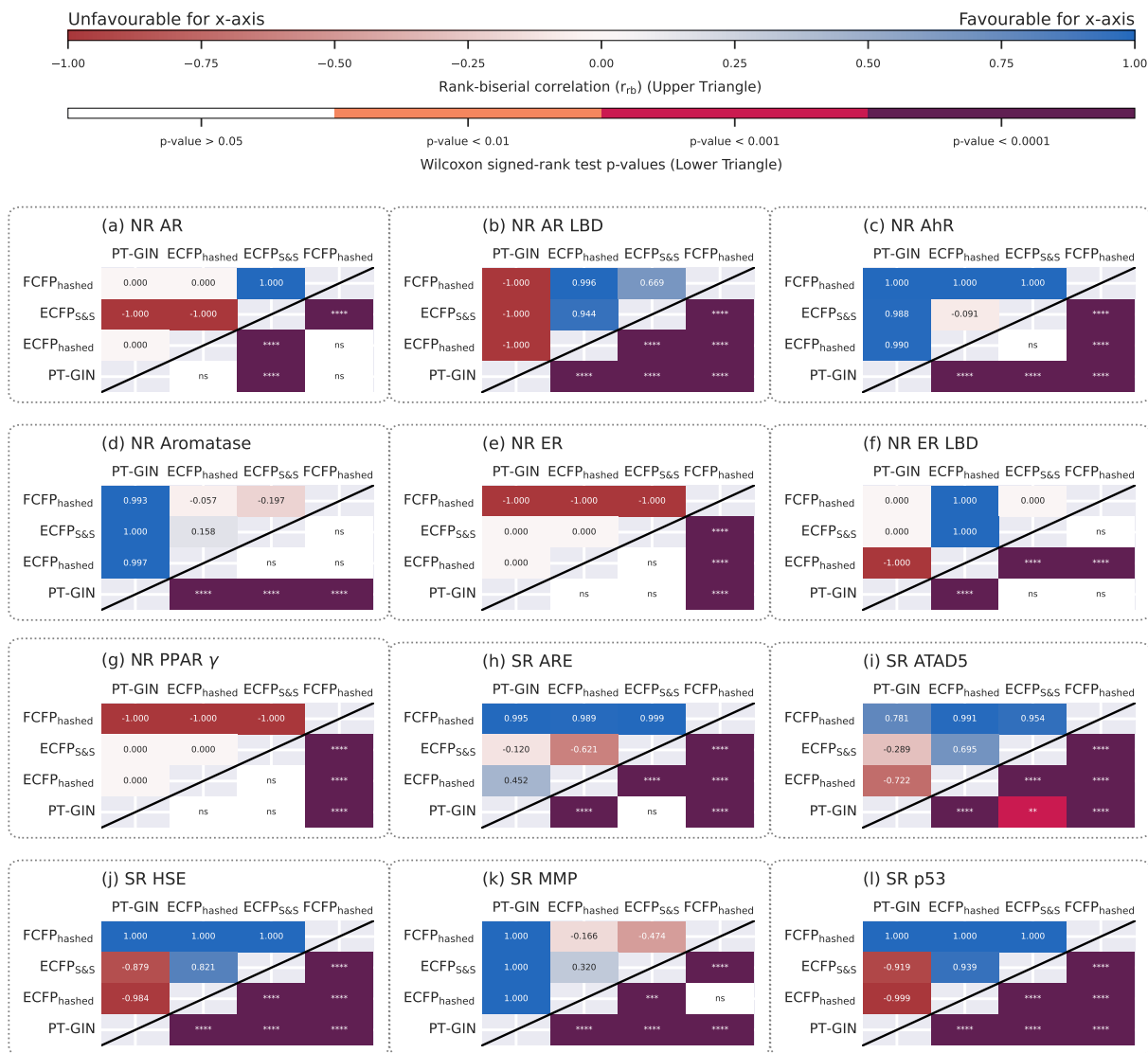


Figure 20: Rank-biserial coefficient (r_{rb}) effect sizes (upper triangle) and Wilcoxon signed-rank test p -values (lower triangle) of the Matthews correlation coefficient (\uparrow MCC) between methods on Tox21 toxicity screening tasks. For task labels, see Table 1. Featurisation methods shown are ECFP-pretrained GINs (PT-GIN), hashed Extended-Connectivity Fingerprints (ECFP_{hashed}), hashed Functional-Connectivity Fingerprints (FCFP_{hashed}), and ECFPs folded via Sort & Slice (ECFP_{S&S}). For r_{rb} effect sizes (upper triangle): blue indicates the method on the x -axis has a higher MCC than the method on the y -axis; red indicates the opposite. For Wilcoxon signed-rank test p -values (lower triangle): white indicates no significant difference and darker indicates a smaller p -value ($n = 199$, $\alpha = 0.05$).

Supplementary Information 1.3 Determining substructure importance via permutation

As both ECFPs folded via Sort & Slice (ECFP_{S&S}) [2] and PT-GIN leverage substructure representations—ECFP_{S&S} maps substructures to bits and PT-GIN maps substructures to tokens in molecular graphs—the relative importance of substructures can be compared. We investigated substructure importance for LightGBM models trained on ECFP_{S&S} and PT-GIN with the FreeSolv dataset [3], along with additional examples on other datasets. We implemented permutation importance [4] for ECFP_{S&S}, and we implemented embedding permutation on substructure tokens prior to message passing for PT-GIN (see Methods).

We found that pharmacophoric features commonly associated with high aqueous solubility (e.g., polar groups and hydrogen bond donors) are present in high ranking substructures for both approaches. Hydroxyls are the top-ranked substructure by importance when predicting aqueous free energy of solvation (ΔG_{solv}) for both ECFP_{S&S} and PT-GIN (Fig. 21). For ECFP_{S&S}, five other oxygen-containing substructures rank in the top ten, including esters, ketones, and cycloalkanol (Fig. 21a). Ketones and esters also rank highly for PT-GIN (Fig. 21b). For both featurisation approaches, models also consider nitrogenous substructures important, with three substructures containing a central nitrogen atom appearing for ECFP_{S&S}, and four for PT-GIN. PT-GIN additionally ranks a haloalkane (Fig. 21b). The overt presence of oxygen and nitrogen is reasonable; both elements are indicative of dipole moments and zwitterions, which enable a molecule to form electrostatic interactions with water, reducing ΔG_{solv} . One would expect molecules with functional groups containing the majority of the top-ranked substructures to have a lower ΔG_{solv} . Collectively, this suggests that both featurisation approaches effectively capture relevant features for predicting ΔG_{solv} .

The models differ noticeably in their reliance on individual substructures. Models trained on ECFP_{S&S} exhibits a stronger reliance on a specific substructure compared to those trained on PT-GIN. There is a clear skew in importance towards the top-ranked hydroxyl substructure using ECFP_{S&S} (Fig. 21a); R^2 reduces by over 0.6 on three instances with ECFP_{S&S}. For folds 0 and 4 with ECFP_{S&S}, every importance measurement except one exceeds a 0.4 decrease in R^2 . Hydroxyls are also the top-ranked substructure for PT-GIN, with R-OH being the only substructure where the majority of measurements have a $-\Delta R^2 > 0.1$, however the skew is not as extreme (Fig. 21b). Models, especially those trained on ECFP_{S&S}, are potentially overfitting to a single substructure as a proxy for predicting ΔG_{solv} . Comparing ΔG_{solv} values for molecules with and without R-OH reveals a distribution shift (Fig. 22). Any model trained on a representation that conveys hydroxyl presence is prone to overfitting to a single feature for a complex task. Predicting ΔG_{solv} only on molecules with R-OH substructures might be a more accurate measure of model robustness. The decrease in reliance on hydroxyl presence of PT-GIN compared to ECFP_{S&S} suggests that PT-GIN overfits less to a single substructure in this instance; this may indicate a loss of atom-level information from graph pooling.

Our novel graph tokenisation approach based on local circular substructures enabled analysis of substructure importance in PT-GINs, with direct comparison to ECFP_{S&S}, providing interpretable insight into model behavior and chemical understanding. Our case study on the FreeSolv benchmark revealed that ECFP_{S&S} may overfit to a single, dominant chemical feature (e.g., hydroxyls), a shortcut that PT-GINs were less prone to. This capability allows researchers to move beyond simple performance metrics and ask why a model is making its predictions on a dataset-wide level, enabling the diagnosis of model weaknesses and the identification of biases in benchmark datasets themselves.

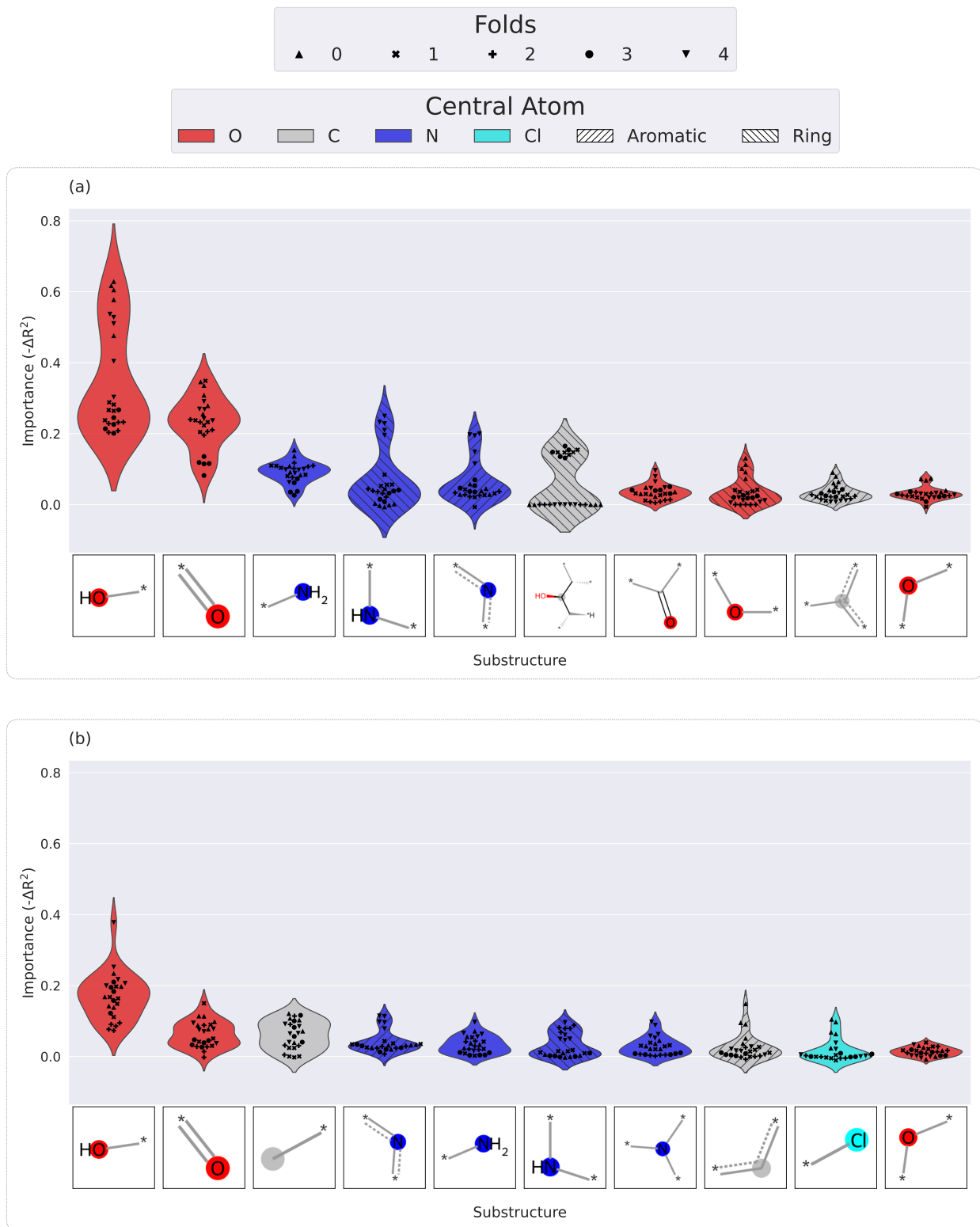


Figure 21: Substructure importances on the FreeSolv dataset. (a) Permutation feature importances for ECFP_{S&S}, mapped to substructures. (b) Token embedding importances for PT-GIN, mapped to substructures. For both (a) and (b), importances were measured as $-\Delta R^2$ on the test set upon permutation. Only the top ten ranked substructures by mean importance are shown. Violin plots are colored by central atom element type; hatches from the bottom left to the top right indicate the central atom is aromatic; hatches from the bottom right to the top left indicate the central atom is in a non-aromatic ring. Individual scores are shown as a swarm plot; marker shape indicates the test set fold.

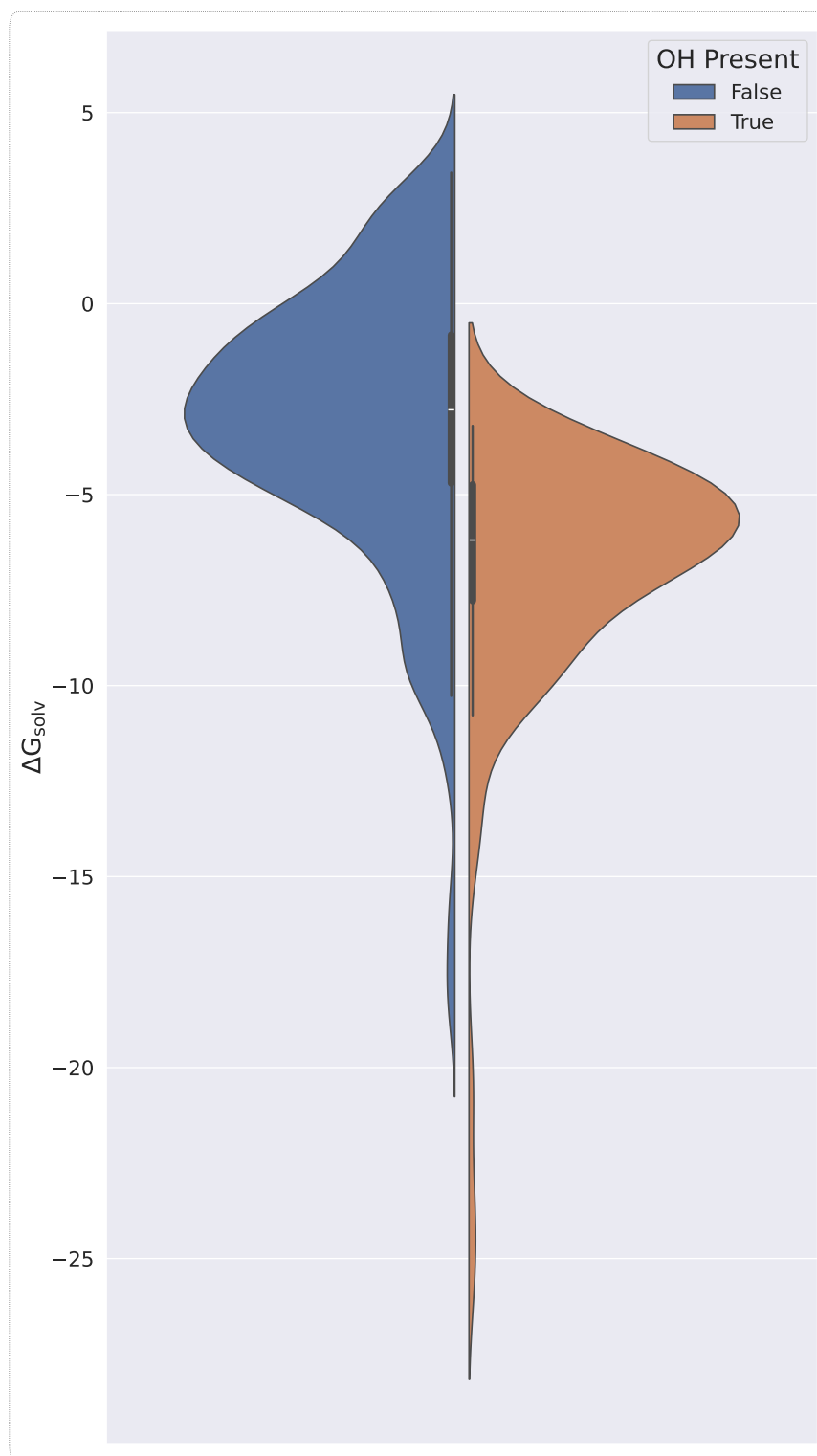


Figure 22: Distribution of ΔG_{solv} in the FreeSolv dataset for molecules with and without R-OH.

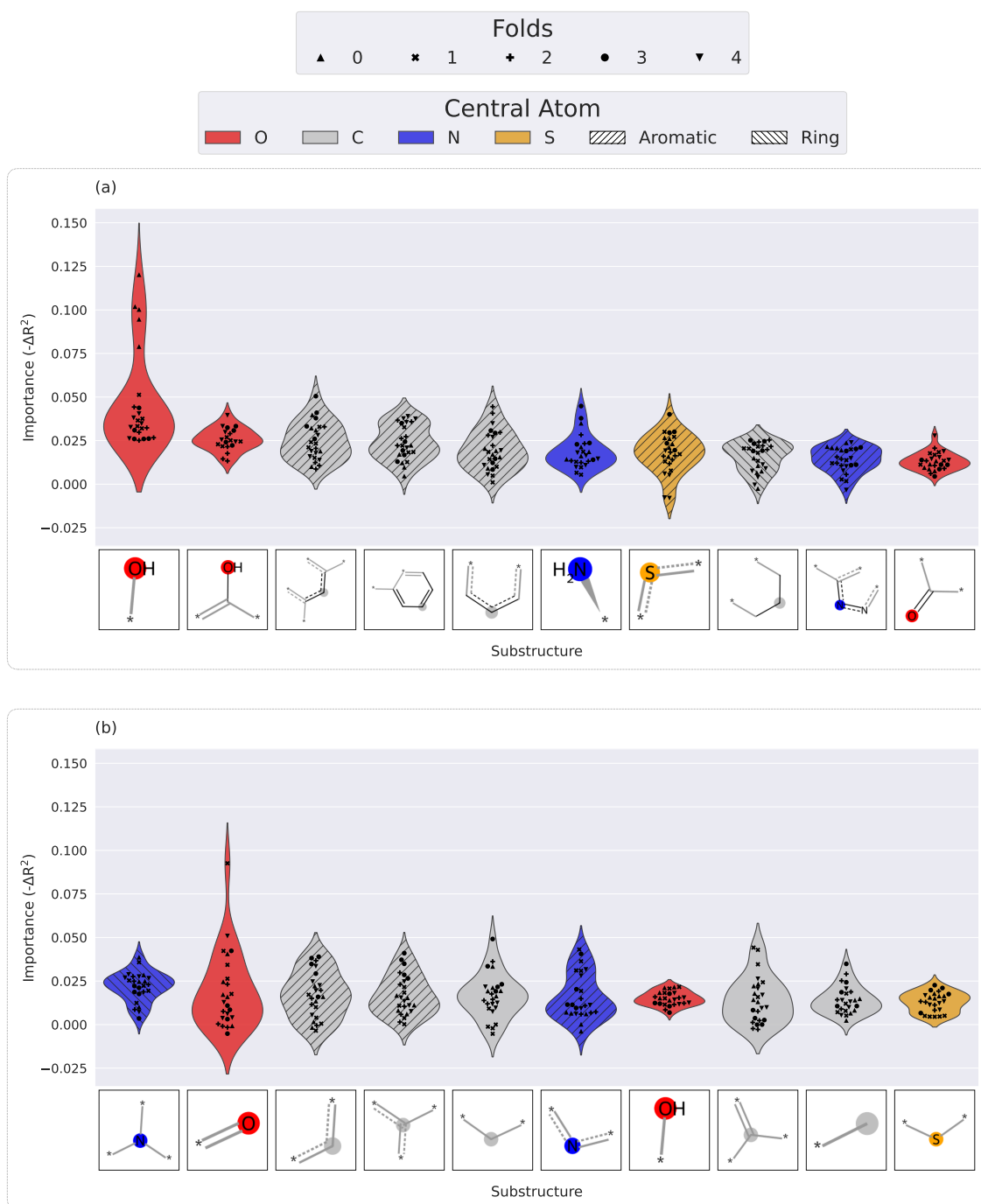


Figure 23: Substructure importances on the Human CLint dataset [5]. (a) Permutation feature importances for $ECFP_{S\&S}$, mapped to substructures. (b) Token embedding importances for PT-GIN, mapped to substructures. For both (a) and (b), importances were measured as $-\Delta R^2$ on the test set upon permutation. Only the top ten ranked substructures by mean importance are shown. Violin plots are colored by central atom element type; hatches from the bottom left to the top right indicate the central atom is aromatic; hatches from the bottom right to the top left indicate the central atom is in a non-aromatic ring. Individual scores are shown as a swarm plot; marker shape indicates the test set fold.

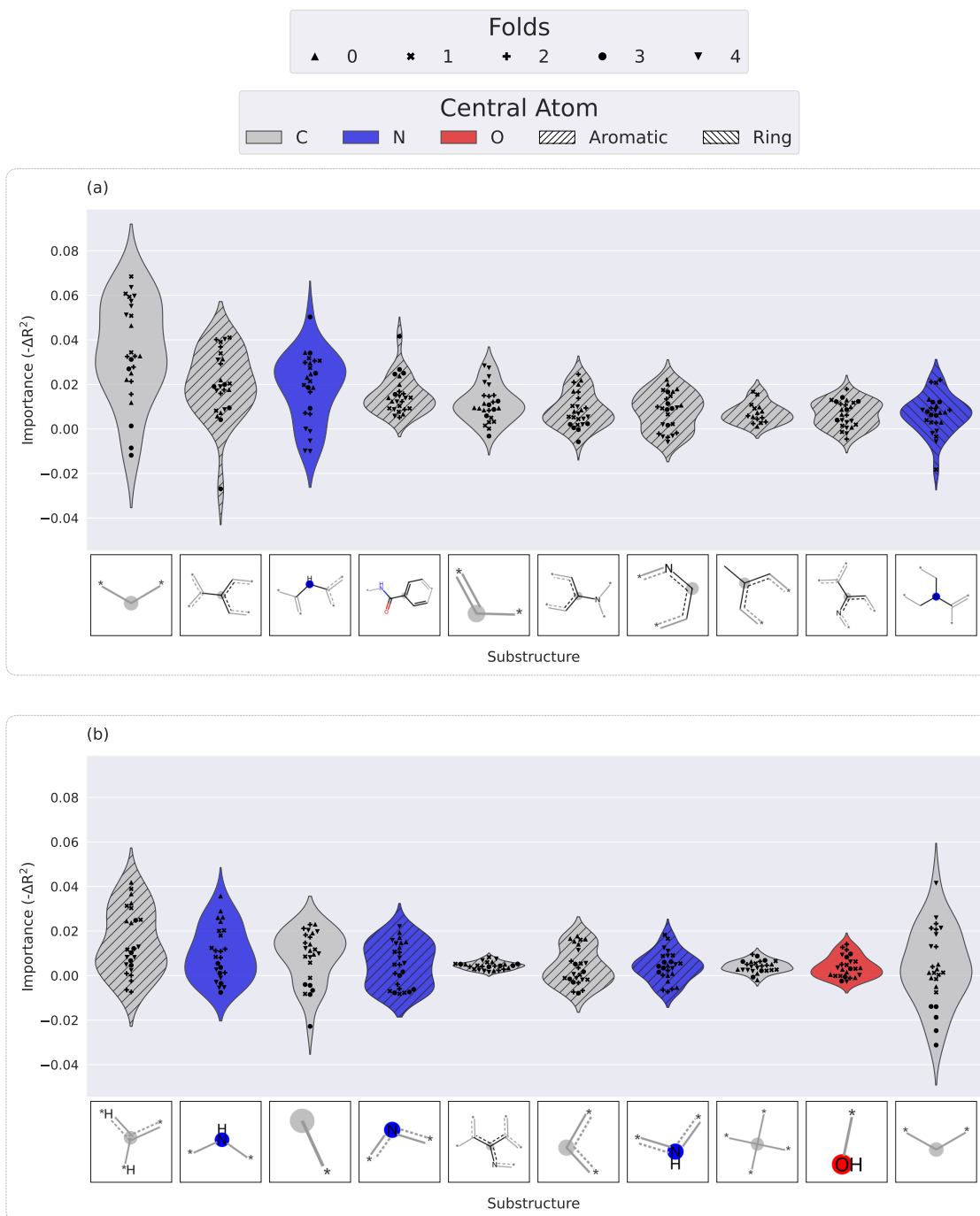


Figure 24: Substructure importances on the Biogen Solubility task [5]. (a) Permutation feature importances for $ECFP_{S\&S}$, mapped to substructures. (b) Token embedding importances for PT-GIN, mapped to substructures. For both (a) and (b), importances were measured as $-\Delta R^2$ on the test set upon permutation. Only the top ten ranked substructures by mean importance are shown. Violin plots are colored by central atom element type; hatches from the bottom left to the top right indicate the central atom is aromatic; hatches from the bottom right to the top left indicate the central atom is in a non-aromatic ring. Individual scores are shown as a swarm plot; marker shape indicates the test set fold.

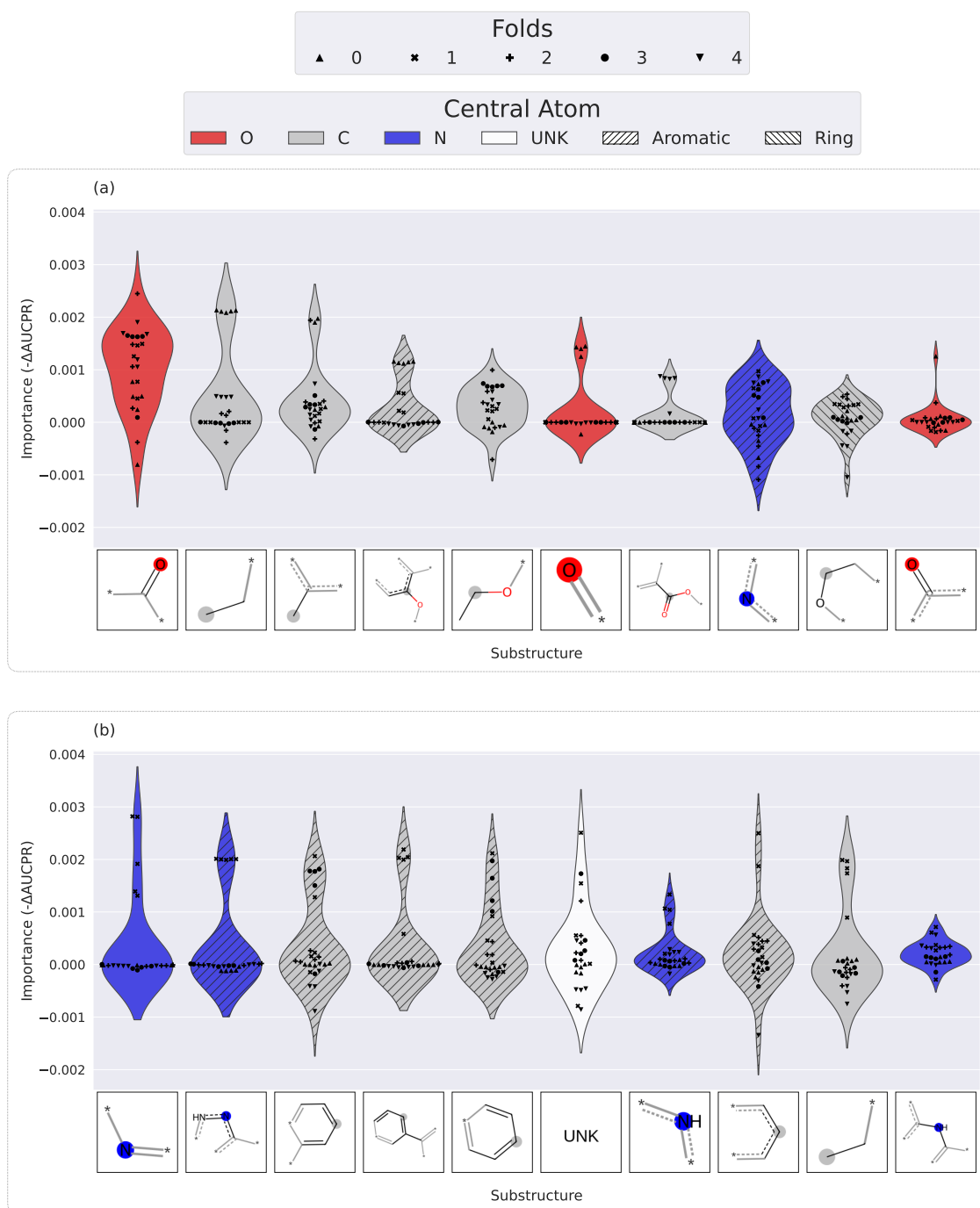


Figure 25: Substructure importances on the MUV858 task [6]. (a) Permutation feature importances for $ECFP_{S\&S}$, mapped to substructures. (b) Token embedding importances for PT-GIN, mapped to substructures. For both (a) and (b), importances were measured as $-\Delta AUCPR$ on the test set upon permutation. Only the top ten ranked substructures by mean importance are shown. Violin plots are colored by central atom element type; hatches from the bottom left to the top right indicate the central atom is aromatic; hatches from the bottom right to the top left indicate the central atom is in a non-aromatic ring. Individual scores are shown as a swarm plot; marker shape indicates the test set fold.

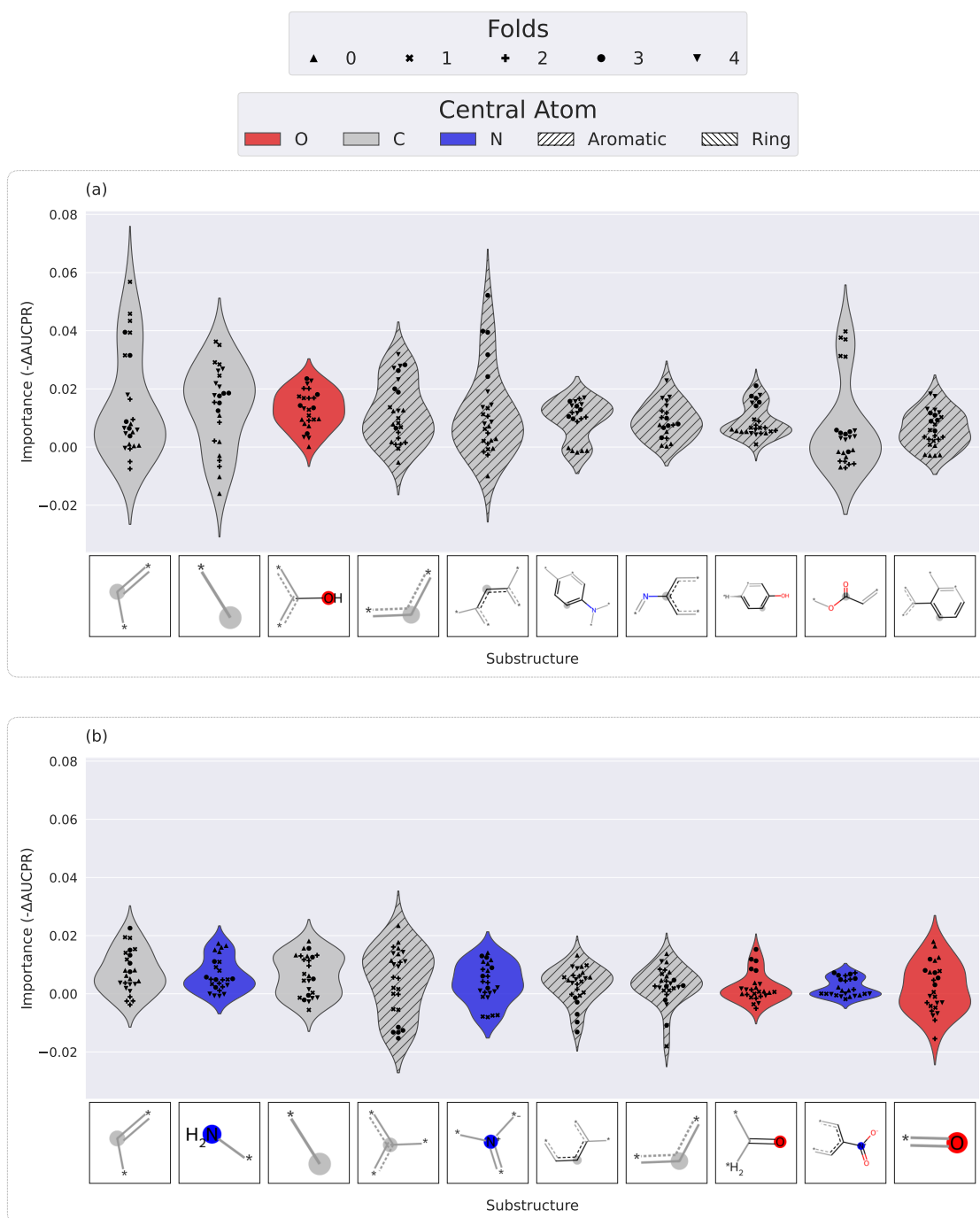


Figure 26: Substructure importances on the Tox21 SR ARE task [1]. (a) Permutation feature importances for ECFP_{S&S}, mapped to substructures. (b) Token embedding importances for PT-GIN, mapped to substructures. For both (a) and (b), importances were measured as $-\Delta\text{AUCPR}$ on the test set upon permutation. Only the top ten ranked substructures by mean importance are shown. Violin plots are colored by central atom element type; hatches from the bottom left to the top right indicate the central atom is aromatic; hatches from the bottom right to the top left indicate the central atom is in a non-aromatic ring. Individual scores are shown as a swarm plot; marker shape indicates the test set fold.

Supplementary Information 1.4 Example Metric Distribution Plots

Supplementary Information 1.4.1 Biogen

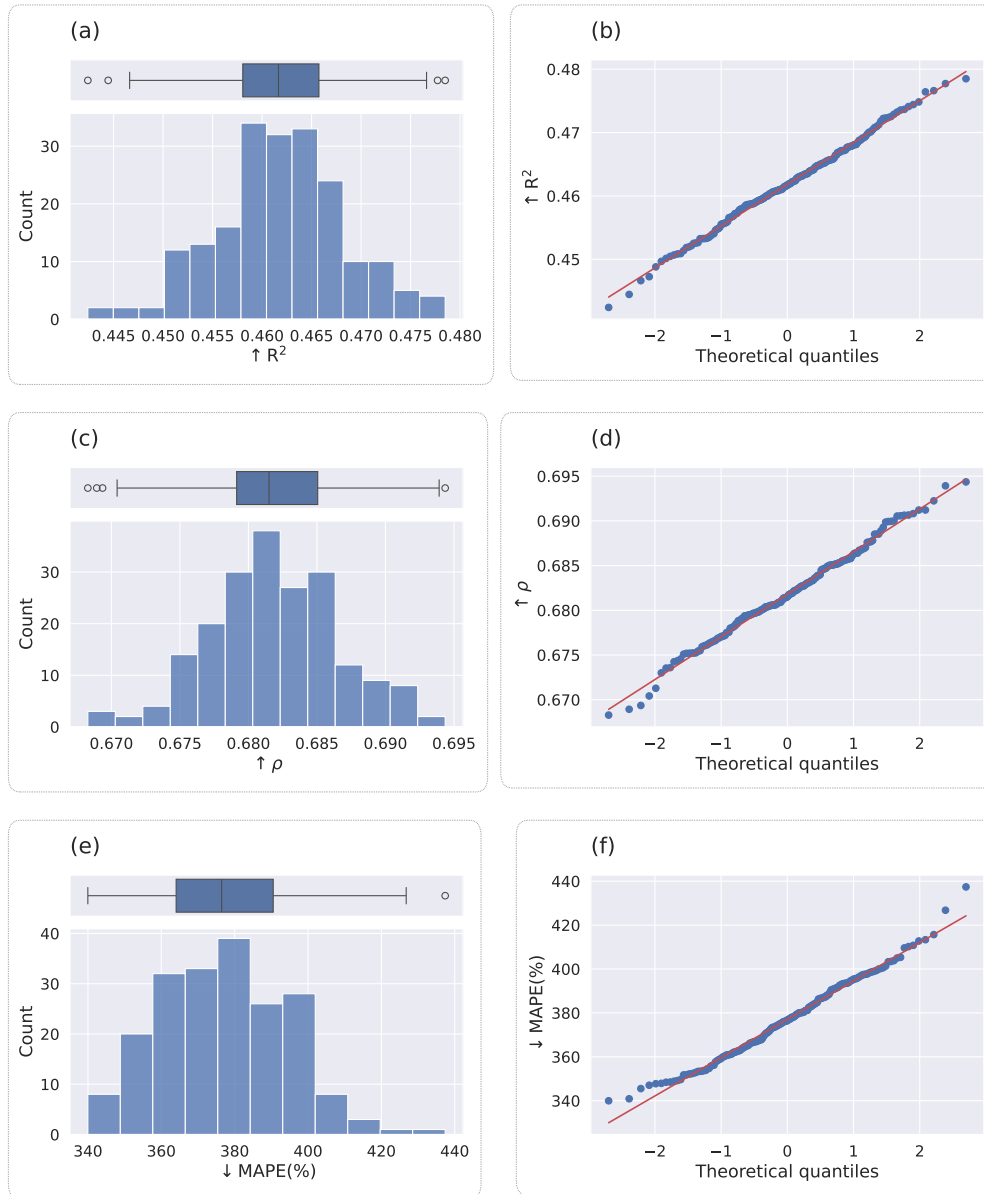


Figure 27: Metric distributions for PT-GIN on Efflux. Left column contains histograms and boxplots. Right column contains normal distribution Q-Q probability plots. Metrics shown are the (a, b) coefficient of determination (R^2), (c, d) Pearson correlation (ρ), and (e, f) mean absolute percentage error (MAPE (%)).

Supplementary Information 1.4.2 MUV

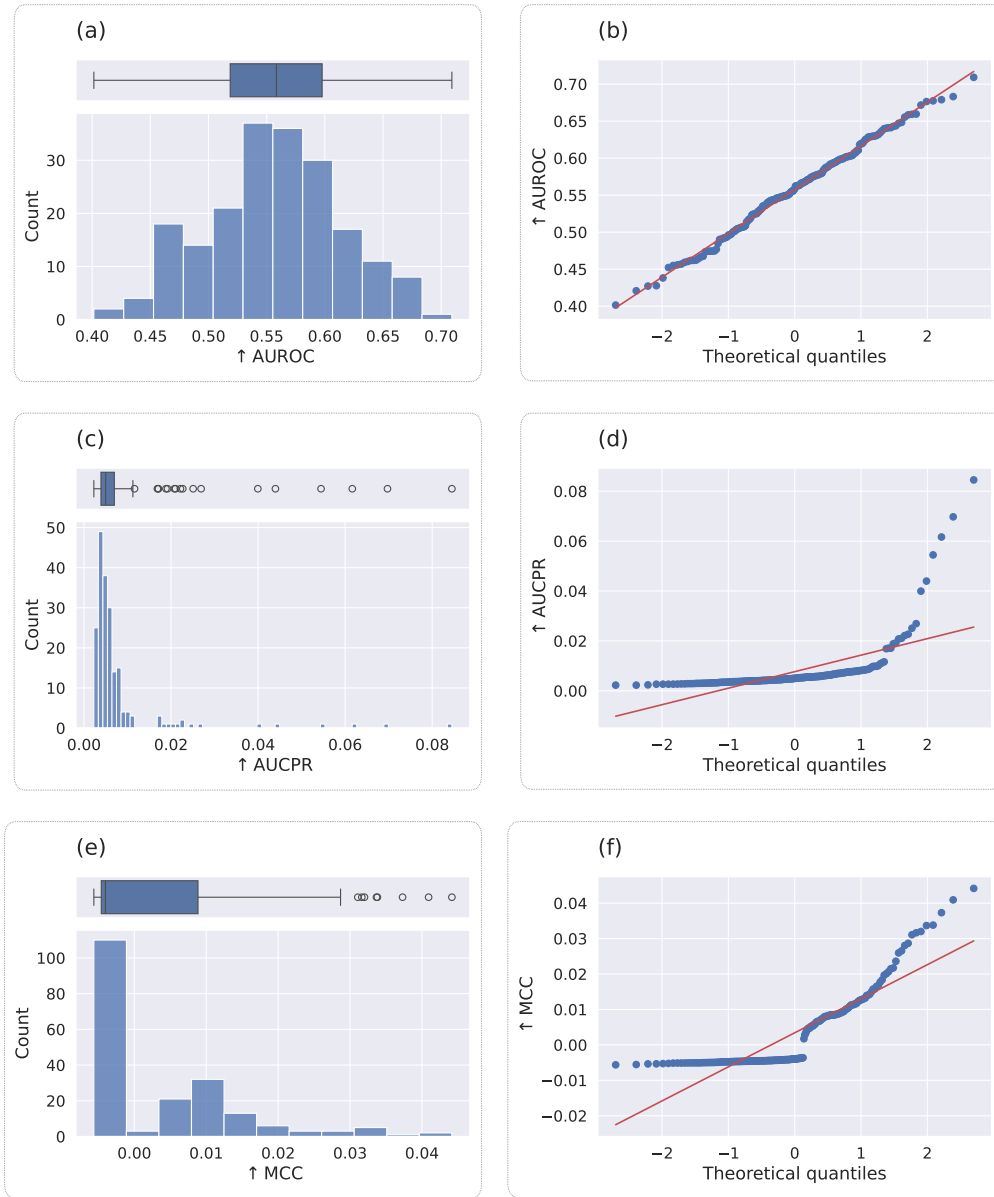


Figure 28: Metric distributions for PT-GIN on MUV466. Left column contains histograms and boxplots. Right column contains normal distribution Q-Q probability plots. Metrics shown are the (a, b) Area Under the Receiver Operating Characteristic (AUROC), (c, d) Area Under the Precision-Recall Curve (AUCPR), and (e, f) Matthews correlation coefficient (MCC).

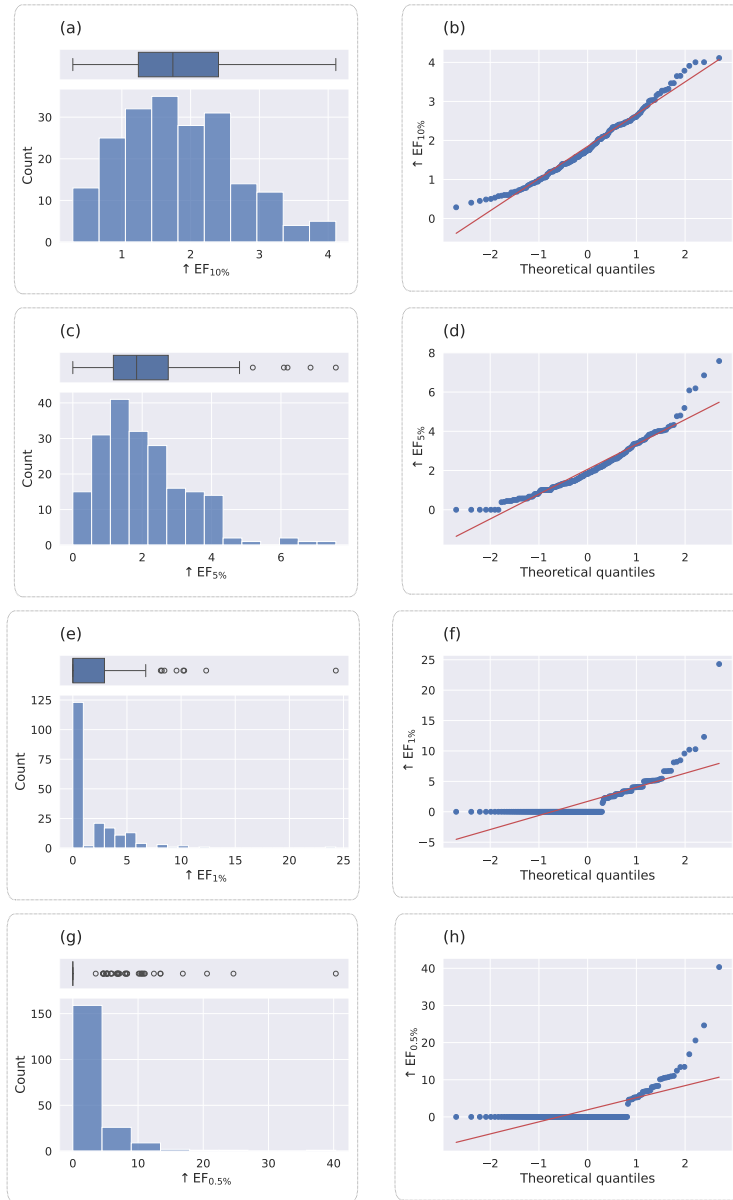


Figure 29: Enrichment Factor distributions for PT-GIN on MUV466. Left column contains histograms and boxplots. Right column contains normal distribution Q-Q probability plots. Metrics shown are Enrichment Factor at (a, b) 10%, (c, d) 5%, (e, f) 1%, and (g, h) 0.5%.

Supplementary Information 2 Algorithms

Algorithm 1 Generating a molecular substructure (i.e., circular subgraph) vocabulary using Sort & Slice

Input: A molecular dataset, \mathcal{M}

Input: A Morgan algorithm-based circular substructure enumeration function, `morgan_generator`

Input: The maximum radius for circular substructures, r_{max}

Input: The maximum substructure vocabulary size, k

```
1: D ← {}                                     ▷ Initialize empty dictionary
2: for molecule ∈  $\mathcal{M}$  do
3:   ▷ Loop over molecules and tally the number of molecules each substructure appears in
4:    $\mathcal{S} \leftarrow \text{morgan\_generator}(\text{molecule}, r_{max})$    ▷ Enumerate and hash circular substructures up to  $r_{max}$ 
5:   for (substructure, radius) ∈ set( $\mathcal{S}$ ) do   ▷ Loop over the set of substructure identifiers
6:     if substructure ∈ D then
7:       D[substructure] ← D[substructure] + 1   ▷ Add to count for substructure
8:     else
9:       D[substructure] ← 1                     ▷ Initialize substructure count
10:    end if
11:  end for
12: end for
13: Dsorted ← sort_by_value(D, descending)     ▷ Sort substructures by frequency
14: Dranked ← assign_ranks(Dsorted)          ▷ Assign integer ranks substructures based on sorted positions
15: vocab ← top_k(Dranked, k)                 ▷ Slice dictionary to retain top-ranked substructures
16: max_id ← max({vocab[k] : k ∈ keys(vocab)})
17: vocab["UNK"] ← max_id + 1
18: return vocab                                ▷ Return substructure vocabulary as a dictionary
```

Algorithm 2 Molecular substructure tokenization

Input: A molecule

Input: A dictionary output from Algorithm 1, `vocab`

Input: The same substructure enumeration function used for Algorithm 1, `morgan_generator`

Input: The same maximum radius used for Algorithm 1, r_{max}

```
1: graph = (V, E) where V := heavy_atoms ∈ molecule, E := bonds ∈ molecule
2: graph.tokens ←  $\mathbf{0}^{|V| \times (r_{max}+1)}$    ▷ Initialize token tensor; rows for each atom and columns for each radius
3:  $\mathcal{S} \leftarrow \text{morgan\_generator}(\text{molecule}, r_{max})$    ▷ Get circular substructures in the molecule
4: for (substructure, radius) ∈  $\mathcal{S}$  do     ▷ Loop over all circular substructures
5:   if substructure ∈ vocab then
6:     token ← vocab[substructure]         ▷ Represent token using substructure rank
7:   else
8:     token ← vocab["UNK"]                ▷ Get the unknown token
9:   end if
10:  central_atom ← get_central_atom(substructure)   ▷ Get the central atom index
11:  graph.tokens[central_atom, radius] ← token   ▷ Add substructure token to graph token tensor
12: end for
13: return graph
```

Algorithm 3 Permute the embeddings of a graph for a particular token

Input: A graph $= (V, E)$, **where** $n = |V|$

Input: The token to permute $\text{token} \in \{0, 1, \dots, v - 1\}$, **where** v is the token vocabulary size

Input: A random index permutation for node embeddings $\text{shuffled_indices} \in \{0, 1, \dots, l - 1\}^l$, **where** l is the node embedding dimension

Ensure: $l \geq n$ ▷ This assumption was always the case for our PT-GIN models

Ensure: Graph token tensor $\text{graph.tokens} \in \{0, 1, \dots, v - 1\}^{n \times m}$, **where** m is the number of tokens per node

Ensure: Graph embedding tensor $\text{graph.F}_v \in \mathbb{R}^{n \times m \times l}$

1: ▷ Find the locations of the token in the graph

2: $\text{token_locs} \leftarrow \{(i, j) \mid \text{graph.tokens}[i, j] = \text{token}, i \in [0, \dots, n - 1], j \in [0, \dots, m - 1]\}$

3: **if** $\text{token_locs} = \emptyset$ **then**

4: **return** graph

▷ If token is not present, return original graph

5: **end if**

6: $\text{permuted_graph} \leftarrow \text{copy}(\text{graph})$

7: $\text{node_embeddings} \leftarrow \text{permuted_graph.F}_v$

8: $\text{start} \leftarrow 0$

9: ▷ Calculate the chunk size for permutations to distribute over the different locations of the token

10: $\text{chunk_size} \leftarrow \left\lfloor \frac{l}{|\text{token_locs}|} \right\rfloor$

11: **for** $(i, j) \in \text{token_locs}$ **do**

12: ▷ Loop through instances of the token and distribute the permutations over the graph

13: $\text{end} \leftarrow \min(\text{start} + \text{chunk_size}, l)$

14: $\text{shuffled_subset} \leftarrow \text{shuffled_indices}[\text{start} : \text{end}]$

15: $\text{node_embeddings}[i, j, \text{start} : \text{end}] = \text{node_embeddings}[i, j, \text{shuffled_subset}]$

16: $\text{start} \leftarrow \text{end}$

17: **end for**

18: $\text{permuted_graph.F}_v \leftarrow \text{node_embeddings}$

19: **return** permuted_graph

Algorithm 4 GNN substructure importance on one train-test split using embedding permutation

Input: A pre-trained graph neural network GNN with substructure tokenization

Input: Training data and labels, $\mathcal{D}_{\text{train}}$ and Y_{train}

Input: Testing data and labels, $\mathcal{D}_{\text{test}}$ and Y_{test}

Input: A metric function

Input: The number of importance measurements to make, *iterations*

Ensure: Pre-trained GNN has a substructure token vocabulary, *vocab*

Ensure: Pre-trained GNN has learned node embeddings $\in \mathbb{R}^{(|\text{vocab}|) \times l}$, **where** *l* is the embedding dimension

Ensure: Pre-trained GNN has the substructure enumeration function used for tokenization, *morgan_generator*

Ensure: Pre-trained GNN has the maximum radius used for substructure tokenization, *max_radius*

```
1:  $X_{\text{train}} \leftarrow \text{GNN}(\mathcal{D}_{\text{train}})$  ▷ Compute frozen global embeddings of train data
2:  $X_{\text{test}} \leftarrow \text{GNN}(\mathcal{D}_{\text{test}})$  ▷ Compute frozen global embeddings of test data
3:  $\text{light\_gbm.fit}(X_{\text{train}}, Y_{\text{train}})$  ▷ Fit a LightGBM model on training data
4:  $\hat{Y}_{\text{test}} \leftarrow \text{light\_gbm}(X_{\text{test}})$ 
5:  $b_0 \leftarrow \text{metric}(\hat{Y}_{\text{test}}, Y_{\text{test}})$  ▷ Calculate base metric score
6:  $\text{output} \leftarrow \mathbf{0}^{|\text{vocab}| \times \text{iterations}}$  ▷ Initialize output array
```

```
7: for iter = 0, ..., iterations - 1 do ▷ Loop over iterations
8:   for index = 0, ...,  $|\text{vocab}| - 1$  do ▷ Loop over the vocabulary
9:     token  $\leftarrow$  index
10:     $\text{shuffled\_indices} \leftarrow \text{shuffle\_array\_order}([0, 1, \dots, |\text{vocab}| - 1])$ 
11:     $X_{\text{permuted}} \leftarrow [ ]$ 
12:    for molecule  $\in \mathcal{D}_{\text{test}}$  do
13:       $n \leftarrow |\{\text{heavy\_atoms} \in \text{molecule}\}|$ 
14:       $\text{graph} \leftarrow \text{tokenize}(\text{molecule}, \text{vocab}, \text{morgan\_generator}, \text{max\_radius})$  ▷ See Algorithm 2
15:       $\text{graph} \leftarrow \text{permute\_graph}(\text{graph}, \text{token}, \text{shuffled\_indices})$  ▷ See Algorithm 3
16:       $\text{graph} \leftarrow \text{GNN.message\_passing}(\text{graph})$ 
17:       $x \in \mathbb{R}^h \leftarrow \text{GNN.pooling}(\text{graph})$ , where h is the dimension of the global embedding
18:       $X_{\text{permuted}}.\text{append}(x)$ 
19:    end for
20:     $\hat{Y}_{\text{permuted}} \leftarrow \text{light\_gbm}(X_{\text{permuted}})$  ▷ Predict label using permuted global embeddings
21:     $b_{\text{permuted}} \leftarrow \text{metric}(\hat{Y}_{\text{permuted}}, Y_{\text{test}})$  ▷ Calculate permuted metric
22:     $\text{score} \leftarrow b_0 - b_{\text{permuted}}$  ▷ Calculate metric difference
23:     $\text{output}[\text{token}, \text{iter}] \leftarrow \text{score}$  ▷ Add score to output array
24:  end for
25: end for
26:  $\text{output} \leftarrow \text{mean}(\text{output}, \text{axis} = 1)$ 
27: return output
```

Supplementary Information 3 Package Versions

Package	Version
LightGBM	4.6.0
NumPy	2.2.3
Optuna	4.2.1
Pandas	2.2.3
PyTorch	2.5.1
PyTorch Geometric	2.6.1
RDKit	2024.09.03
Scikit-learn	1.6.0
Scikit-posthocs	0.11.4
SciPy	1.15.2
TorchEval	0.0.7

Table 2: Python package versions used in this work.

Supplementary Information 4 Datasets

Dataset	Source	Number of Molecules
Efflux ratio	Biogen [5]	2642
Human plasma protein binding	Biogen [5]	194
Human intrinsic hepatic clearance	Biogen [5]	3087
Rat plasma protein binding	Biogen [5]	168
Rat intrinsic hepatic clearance	Biogen [5]	3054
Solubility	Biogen [5]	2173
ESOL	MoleculeNet [7], ESOL [8]	1069
FreeSolv	MoleculeNet [7], FreeSolv [3]	640
Lipophilicity	MoleculeNet [7], ChEMBL [9]	4200
MUV466	MoleculeNet [7], Rohrer et al. [6]	14844
MUV548	MoleculeNet [7], Rohrer et al. [6]	14737
MUV600	MoleculeNet [7], Rohrer et al. [6]	14734
MUV652	MoleculeNet [7], Rohrer et al. [6]	14903
MUV689	MoleculeNet [7], Rohrer et al. [6]	14606
MUV692	MoleculeNet [7], Rohrer et al. [6]	14647
MUV712	MoleculeNet [7], Rohrer et al. [6]	14415
MUV713	MoleculeNet [7], Rohrer et al. [6]	14841
MUV733	MoleculeNet [7], Rohrer et al. [6]	14691
MUV737	MoleculeNet [7], Rohrer et al. [6]	14696
MUV810	MoleculeNet [7], Rohrer et al. [6]	14646
MUV832	MoleculeNet [7], Rohrer et al. [6]	14676
MUV846	MoleculeNet [7], Rohrer et al. [6]	14714
MUV852	MoleculeNet [7], Rohrer et al. [6]	14658
MUV858	MoleculeNet [7], Rohrer et al. [6]	14775
MUV859	MoleculeNet [7], Rohrer et al. [6]	14751
NR AR	MoleculeNet [7], Tox21 [1]	7257
NR AR LBD	MoleculeNet [7], Tox21 [1]	6750
NR AhR	MoleculeNet [7], Tox21 [1]	6541
NR Aromatase	MoleculeNet [7], Tox21 [1]	5814
NR ER	MoleculeNet [7], Tox21 [1]	6185
NR ER LBD	MoleculeNet [7], Tox21 [1]	6947
NR PPAR γ	MoleculeNet [7], Tox21 [1]	6442
SR ARE	MoleculeNet [7], Tox21 [1]	5824
SR ATAD5	MoleculeNet [7], Tox21 [1]	7064
SR HSE	MoleculeNet [7], Tox21 [1]	6459
SR MMP	MoleculeNet [7], Tox21 [1]	5804
SR p53	MoleculeNet [7], Tox21 [1]	6766
DRD2	ChEMBL [9], Dablander et al. [10]	6333
Factor X _A	ChEMBL [9], Dablander et al. [10]	3605

Table 3: Summary of the benchmark datasets used in this study. The number of molecules shown is the total number of SMILES that passed RDKit standardization.

Dataset	Number of Train-Test Splits with Positive Samples in the Test Set
MUV466	991
MUV548	990
MUV600	994
MUV644	989
MUV652	993
MUV689	992
MUV692	994
MUV712	991
MUV713	990
MUV733	992
MUV737	986
MUV810	994
MUV832	992
MUV846	989
MUV852	994
MUV858	992
MUV859	987

Table 4: Total number of test sets used for metric evaluation for MUV tasks. As MUV tasks are highly imbalanced, StratifiedGroupKFold splitting occasionally produces one fold with no positive classes. Folds without positive samples were excluded as test sets for metric evaluation; cross-validation averages were determined using the remaining available folds for each repeat.

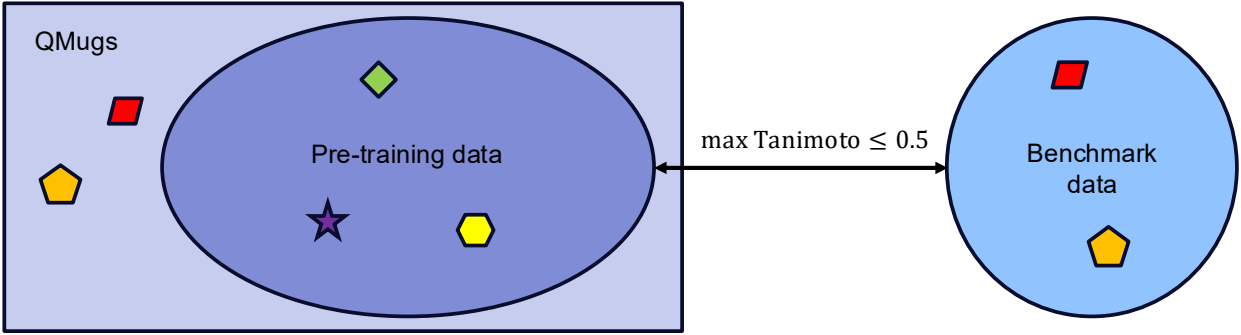


Figure 30: Tanimoto similarity filtering of pre-training dataset.

Supplementary Information 5 Hyperparameters

Hyperparameter	Search Type	Search Space
Activation	categorical	LeakyReLU, GELU, Hardswish
Batch Normalization	categorical	True, False
Dropout	float	0.0 - 0.5
Embedding dimensions	categorical	128, 256, 512
GIN MLP Layers	categorical	1, 2, 3
Graph Pooling	categorical	mean, sum, max
Hidden dimensions	categorical	128, 256, 512
Message Passing Layers	categorical	1, 2, 3
Prediction Head Layers	categorical	2, 3, 4
Weight Sharing	categorical	True, False

Table 5: GIN hyperparameters explored for pre-training.

Hyperparameter	Value
Activation	Hardswish
Batch Normalization	False
Batch Size	128
Bias initialization	Zeros
Dropout	0.125
Embedding Dimensions	512
Epochs	50
GIN MLP Layers	3
Graph pooling	Sum
Hidden Dimensions	512
Layer aggregation (readout)	last (pre-training); concat (benchmarking)
Learning Rate Half-Life (Epochs)	5
Learning Rate Start Factor	0.5
Message Passing Layers	3
Optimizer	Adam
Prediction Head Layers	2
Share Weights	True
Train eps	True
Warm-up Epochs	2
Weight initialization	Xavier Normal

Table 6: PT-GIN hyperparameters. For pre-training, layer aggregation was set to "last" to use the output of the final GIN layer as the global embedding. This was done to reduce the number of parameters in the prediction head and speed up pre-training. For benchmarking, layer aggregation was set to "concat" to concatenate the outputs of all GIN layers as the global embedding. This was done to maximize the information available in the global embedding for downstream tasks; the number of features was not a concern for benchmarking, as LightGBM models are capable of handling high-dimensional input relatively well.

Substructure Maximum Radius	Token Embedding Dimension	Initial Node Dimension	Hidden Layer Dimension	Number of Convolutions	Final Concatenated Embedding Dimension
0	512	512	512	3	2048
1	512	1024	512	3	2560
2	512	1536	512	3	3072

Table 7: PT-GIN embedding dimensions before and after convolutions.

Hyperparameter	Search Type	Search Space
num_leaves	int	10-100
learning_rate	float with log	0.001-0.3
n_estimators	int	10-120
subsample_for_bin	int	20000-200000
min_data_in_leaf	int with log	1-1000
bagging_fraction	float	0.25-1.0
feature_fraction	float	0.25-1.0
reg_alpha	float with log	0.01-10.0
reg_lambda	float with log	0.01-10.0

Table 8: LightGBM hyperparameters explored in benchmarking.

Hyperparameter	Search Type	Search Space
Activation	categorical	Hardswish
Dropout	float	0.0 - 0.5
Graph pooling	categorical	Max
Layer aggregation	categorical	concatenate
Learning Rate Half Life (Epochs)	int	5-50
Learning Rate Scaling Factor	float	0.1-1.0
Message Passing Layers	int	1-5
Prediction Head Layers	int	1-5
Train eps	categorical	True, False
Weight Sharing	categorical	True, False

Table 9: Hyperparameters explored for Scratch GIN models in benchmarking, regardless of dataset size. The initial learning rate was calculated as $lr = c \cdot d_{model}^{-0.5}$, where c is the learning rate scaling factor and d is the number of model parameters.

Hyperparameter	Search Type	Search Space
Batch Size	int	16
Embedding dimensions	categorical	2, 4, 8
GIN MLP Layers	int	1-3
Hidden dimensions	categorical	4, 8

Table 10: Hyperparameters explored for Scratch GIN models on datasets with fewer than 500 samples.

Hyperparameter	Search Type	Search Space
Batch Size	int	32
Embedding dimensions	categorical	4, 8, 16
GIN MLP Layers	int	1-5
Hidden dimensions	categorical	4, 8, 16

Table 11: Hyperparameters explored for Scratch GIN models on datasets with $500 \leq n < 1000$ samples.

Hyperparameter	Search Type	Search Space
Batch Size	int	128
Embedding dimensions	categorical	8, 16, 32
GIN MLP Layers	int	1-5
Hidden dimensions	categorical	8, 16, 32

Table 12: Hyperparameters explored for Scratch GIN models on datasets with $1000 \leq n < 5000$ samples.

Hyperparameter	Search Type	Search Space
Batch Size	int	64
Embedding dimensions	categorical	16, 32, 64
GIN MLP Layers	categorical	1-5
Hidden dimensions	categorical	16, 32, 64

Table 13: Hyperparameters explored for Scratch GIN models on datasets with $n \geq 5000$ samples.

References

- [1] Richard, A. M. *et al.* The Tox21 10K Compound Library: Collaborative Chemistry Advancing Toxicology. *Chemical Research in Toxicology* **34**, 189–216 (2021). URL <https://doi.org/10.1021/acs.chemrestox.0c00264>.
- [2] Dablander, M., Hanser, T., Lambiotte, R. & Morris, G. M. Sort & Slice: A simple and superior alternative to hash-based folding for extended-connectivity fingerprints. *Journal of Cheminformatics* **16**, 135 (2024). URL <https://doi.org/10.1186/s13321-024-00932-y>.
- [3] Mobley, D. L. & Guthrie, J. P. FreeSolv: A database of experimental and calculated hydration free energies, with input files. *Journal of Computer-Aided Molecular Design* **28**, 711–720 (2014). URL <https://doi.org/10.1007/s10822-014-9747-x>.
- [4] Breiman, L. Random Forests. *Machine Learning* **45**, 5–32 (2001). URL <https://doi.org/10.1023/A:1010933404324>.
- [5] Fang, C. *et al.* Prospective Validation of Machine Learning Algorithms for Absorption, Distribution, Metabolism, and Excretion Prediction: An Industrial Perspective. *Journal of Chemical Information and Modeling* **63**, 3263–3274 (2023). URL <https://doi.org/10.1021/acs.jcim.3c00160>.
- [6] Rohrer, S. G. & Baumann, K. Maximum unbiased validation (MUV) data sets for virtual screening based on PubChem bioactivity data. *Journal of Chemical Information and Modeling* **49**, 169–184 (2009). URL <https://doi.org/10.1021/ci8002649>.
- [7] Wu, Z. *et al.* MoleculeNet: A benchmark for molecular machine learning. *Chemical Science* **9**, 513–530 (2018). URL <https://doi.org/10.1039/C7SC02664A>.
- [8] Delaney, J. S. ESOL: Estimating Aqueous Solubility Directly from Molecular Structure. *Journal of Chemical Information and Computer Sciences* **44**, 1000–1005 (2004). URL <https://doi.org/10.1021/ci034243x>.
- [9] Zdrazil, B. *et al.* The ChEMBL Database in 2023: A drug discovery platform spanning multiple bioactivity data types and time periods. *Nucleic Acids Research* **52**, D1180–D1192 (2024). URL <https://doi.org/10.1093/nar/gkad1004>.
- [10] Dablander, M., Hanser, T., Lambiotte, R. & Morris, G. M. Exploring QSAR models for activity-cliff prediction. *Journal of Cheminformatics* **15**, 47 (2023). URL <https://doi.org/10.1186/s13321-023-00708-w>.